THESIS FOR THE DEGREE OF DOCTOR OF PHILOSOPHY

Vibrational energy harvesting for sensors in vehicles

JOHAN BJURSTRÖM

Department of Microtechnology and Nanoscience

CHALMERS UNIVERSITY OF TECHNOLOGY

Gothenburg, Sweden 2024

Vibrational energy harvesting for sensors in vehicles

JOHAN BJURSTRÖM

ISBN 978-91-8103-147-8

Doktorsavhandlingar vid Chalmers tekniska högskola
Ny serie nr 5605
ISSN 0346-718X

Chalmers University of Technology
Microtechnology and Nanoscience - MC2
SE-412 96 Göteborg, Sweden
Telephone + 46 (0)31-772 1000

Chalmers digitaltryck
Gothenburg, Sweden 2024

Vibrational energy harvesting for sensors in vehicles

JOHAN BJURSTRÖM

Department of Microtechnology and Nanoscience

Chalmers University of Technology

Abstract

The miniaturization of semiconductor technology and reduction in power requirements have enabled wireless self-sufficient devices, powered by ambient energy. To date the primary application lies in generating and transmitting sensory data. The number of sensors and their applications in automotive vehicles have grown drastically in the last decade. Wireless self-powered sensors can facilitate current sensor systems by removing the need for cabling and may enable additional applications. These systems have the potential to provide new avenues of optimization in safety and performance.

This thesis delves into the topic of vibrations as ambient energy source, primarily for sensors in automotive vehicles. The transduction of small amounts of vibrational, i.e. kinetic, energy to electrical power, also known as vibrational energy harvesting, is an extensive field of research with a plethora of inventions. A short review is given for energy harvesters, in an automotive context, utilizing transduction through either the piezoelectric effect or magnetic induction. Three practical examples of kinetic energy harvesting in vehicles are described in more detail. The first is a piezoelectric beam for powering a strain sensor on the engines rotating flexplate. It makes combined use of centrifugal force, gravitational pull and random vibrations to enhance performance and reduce required system size. The simulated power output is 370 μW at a rotation frequency of 10.5 Hz, with a bandwidth of 2.44 Hz. The second example is an energy harvesting unit placed on a belt buckle to power a hall sensor measuring if the belt buckle is securely buckled in. It implements magnetic induction by the novel concept of a spring balance air gap of a magnetic circuit, to efficiently harvest minute vibrations and allow for tuning of the resonance frequency through adjusting the equilibrium air gap distance. Simulations show a resonance frequency tuning of 420 Hz/mm (on average) and the potential to achieve 52 μW under normal road conditions driving at 70 km/h. A potential improvement of this concept, by implementing a magnetostrictive component, is evaluated in a separate work. The same concept, of a spring balanced air gap in a magnetic circuit, is here implemented in a cantilever design. In this way the magnetostrictive component can easily me incorporated into the spring component, i.e. the cantilever, and can thus affect both proof mass displacement and magnetic flux. The system using magnetostriction shows a factor of 2 larger output power, compared to an equivalent system without magnetostriction, while maintaining a resonance frequency tuning of 140 Hz /mm. The third practical example is of a device for harvesting the mechanical energy from the occupant's act of buckling and unbuckling the seat belt. The linear motion of the belt buckle insertion and extraction is in this case used to drive movement of magnets and induce voltage in a coil. The linear motion of the buckle is converted to rotation of a magnet array to increase power generation. Simulations show the device can potentially generate 4 mJ for a single buckle insertion.

Theoretical modeling of vibrational energy harvesting systems is also addressed. Fundamental descriptions of the lumped and distributed models are given. Based on the lumped models of a piezoelectric energy harvester (PEH) and an electromagnetic energy harvester (EMEH), a unified model is described and analyzed. New insights are gained regarding the pros and cons of the two types of energy harvester run at either resonance or anti-resonance. A numerical solution is given for the exact boundary of a dimensionless quality factor and a dimensionless intrinsic resistance, at which the system begins to exhibit anti-resonance. Regarding the maximum achievable power, the typical PEH is favored when running the system in anti-resonance and the typical EMEH is favored at resonance. The described modeling considers all parameters of the lumped model and thus provides a useful tool for developing vibrational energy harvester prototypes.

Keywords: vibration energy harvesting, unified modeling, piezoelectric, electromagnetic induction, anti-resonance, prescribed displacement, automotive safety, low frequency, small amplitude excitation, nonlinear dynamics, magnetostriction, galfenol, frequency tuning.

List of publications

Paper I

J. Bjurström, F. Ohlsson, A. Vikerfors, C. Rusu and C. Johansson

“Tunable spring balanced magnetic energy harvester for low frequencies and small displacements”

Energy Conversion and Management 259 (2022) 115568

Paper II

J. Bjurström, F. Ohlsson, C. Rusu and C. Johansson

“Unified modeling and analysis of vibration energy harvesters under inertial loads and prescribed displacements”

Applied Sciences 2022, 12, 9815

Paper III

J. Bjurström, E. Köhler, H. Staaf, T. Björnfot, D. Kolev, C. Rusu, S. Nord, M. Andersson, E. Godtman Kling,

“Energy harvesting feasibility for safety belt buckle”

2024 IEEE Wireless Power Technology Conference and Expo (WPTCE), 8-11 May 2024, Kyoto, Japan

Paper IV

J. Bjurström, C. Rusu and C. Johansson,

“Combining Magnetostriction with Variable Reluctance for Energy Harvesting at Low Frequency Vibrations”,

Applied Sciences 2024, 14(19), 9070. Special issue ‘Advanced Energy Harvesting Technology’

Acknowledgements

The list is long, of those deserving of acknowledgment, and gratitude, for bringing me to this point. From the very beginning the people in our lives affect its direction and are inevitably a part of how we wind up where we are now. I cannot mention you all here but know that I am grateful.

This thesis work I owe to my supervisor Cristina Rusu, who invited me into this field of research. Thank you for making my PhD experience as positive as possible, with the best possible outcome, and thank you for your warm-hearted mentorship and wise guidance.

I am thankful for Per Lundgren and Peter Enoksson and their support and valuable advice.

I am also very thankful for Christer Johansson and Fredrik Ohlsson and their enthusiasm in sharing their wealth of knowledge and discussing ideas.

I am grateful for The Swedish Foundation for Strategic Research (project FID16-0055), Chalmers and RISE for providing the means for me to perform my research. Also, I am thankful to Yogen Patel (Autoliv) for this interesting and very challenging research topic opportunity, to Stefan Nord and Mikael Andersson (Autoliv) for excellent construction of the harvester buckle and tests in your lab, and not least Erik Godtman Kling (ReVibe Energy AB) for inspiring electromagnetic discussions and harvester buckle construction.

The greatest debt of gratitude of course goes to my family, for they have shared in my troubles with none of the gain.

To my father for his useful input in scientific discussions and instilling me with the essence of the scientific process.

To my mother for her empathy and for always listening.

To my sister for being the best of role models and always waiting with open arms.

To my son for making me laugh in the darkest of times.

To my wife for being an inspiration in life and driving me to grow. For her wisdom and emotional support throughout it all. For her love and the joy it gives me.

Mölndal, December 2024

Johan Bjurström

Contents

CHAPTER 1

Vibrational energy harvesting – an overview

1.1 Introduction

Energy harvesters (EHs) refer to the small-scale technology for converting ambient energy to a useful form. In modern society the most useful form is typically electrical energy. A common source of ambient energy is movement, i.e., kinetic energy, for example from moving or vibrating parts in devices or vehicles. A vibrational energy harvester (VEH) is a small device for scavenging ambient kinetic energy and converting it to electrical energy. State-of-the-art VEH range in size from centimeters to nanometers and generate electrical power in the range of nano watts to watts, depending on their purpose and environment.

The very first instance of kinetic energy harvesting dates to the early 1800s [1,2] and the invention of the electrical generator by Michael Faraday (Figure 1 left), utilizing magnetic induction. At this time Faradays invention was a simple and safe way of generating small amounts of electricity for use in scientific research but evolved to grow in scale and become the main means with which we generate electricity throughout society. Additional methods for generating electricity from movement were demonstrated in the late 1800s and early 1900s but were impractical to scale in size to produce commercially useful amounts of electrical power. Until the 21st century there was no commercial incentive in small-scale energy harvesting devices. However, this fact began to change by the introduction of semiconductor technology and in extension processor units.

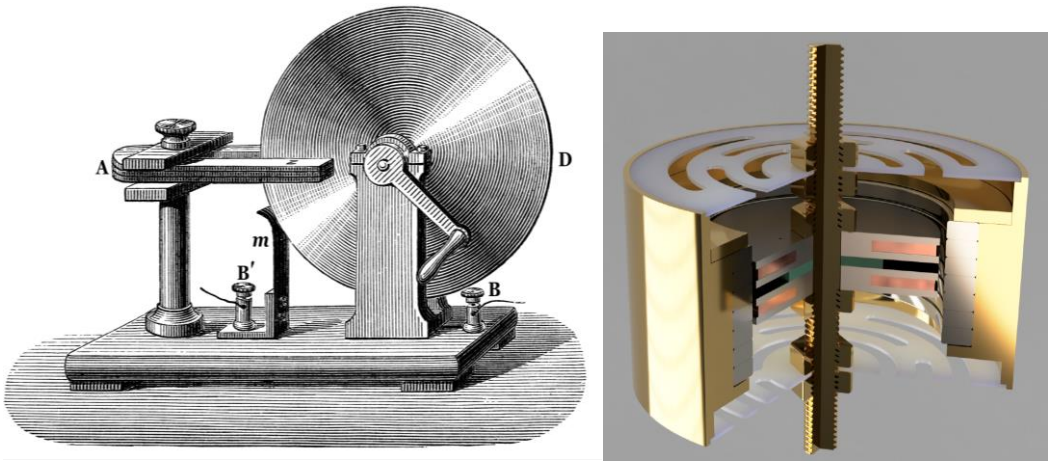

Figure 1. Left: A depiction of Faradays original electric generator [3]. Right: 3D rendering by Digregorio et al. [4] / CC BY. The rendering shows a state-of-the-art electromagnetic vibrational energy harvester utilizing the motion of a stack of ring magnets attached to a pair of planar springs.

The advancements in semiconductor technology have resulted in commercially available ultra-low power microprocessors (running on as little as 18 µW/MHz [5]) and low power transceivers [6–9]. Sondej et al. demonstrates a complete ultra-low power wireless sensor system [10], using a proprietary communication protocol, with a power consumption of 21 µW per kb/s of wirelessly throughput data. Research on vibrational energy harvesting has been active since the beginning of the 21st century [11]. Looking at the plethora of solutions which have been developed over the past two decades, a significant portion of them can provide well and above the power needs of low power electronics (see, e.g., review articles on vibrational energy harvesting [12–14]). Although the application requirements still limit many of the viable solutions, vibrational energy harvesting for powering commercial small-scale applications is now a reality and with continued progress in research the number of viable applications will grow.

1.2 Vibrational energy harvesting in vehicles

The most evident benefit of energy harvesting is self-sustained electronics for cases where access is difficult or impossible and in cases where many units result in high maintenance costs or cumbersome power cabling. An important area where self-sustained electronics can be beneficial is in automotive applications [15–19], primarily considering sensors for safety, performance optimization and predictive maintenance. An automotive vehicle has several energy sources which may be exploited by energy harvesting in general, such as heat, RF-signals and sunlight. Within a vehicle, these are however limited in region or availability [20]. Kinetic energy, in the form of vibrations, is available throughout the vehicle.

The current trend in the development of automotive vehicles is an increased use of sensors and computational power (see Figure 2 for examples of sensors in cars). Some examples are adaptive power train control for increased efficiency [21,22], tire pressure sensing, tire grip indicators, and safety systems such as “Lane assist”, “early obstruction detection” and “Air bag control”. All these systems rely on sensory input, leading to an increasing number of sensors. Increasingly autonomous vehicles also create an increased reliance on sensory input, both external to the vehicle and internal. Internal sensory input can improve vehicle safety as it provides information on passenger and driver characteristics [23], which can include e.g., driver alertness, occupant detection and occupant properties (e.g., height, belt buckle state or vital signs [24]). Proper vehicle behavior and structural integrity are also key factors in vehicle safety and can be determined using internal vehicle sensor data.

External sensor data is primarily produced by telemetry sensors (such as infra-red or optical cameras), which typically require a large energy source, not achievable through energy harvesting. These sensors are however not required in large numbers and have the benefit being able to produce large amounts of information (through image analysis) and can be used both externally and internally. *In situ* measurement data, produced by *in situ* sensors, is still required for many cases of internal sensing (such as in tire pressure or grip sensing, power train control, vehicle behavior and structural integrity). Such *in situ* sensors can typically be passive and placed in numerous, hard to reach, places. The *in situ* data may also be more efficient in regard to the produced meta-data (e.g., occupant detection is likely simpler to determine through pressure sensing rather than image analysis) Integration of a large number

of sensors is challenging to realize if batteries must be utilized (due to replacement need, inaccessible deployment, large quantities and environmental impact). Alternatively, wired power distribution is needed, increasing weight/cost and complicating the installation due to limited space. The most promising solution is therefore self-powered wireless sensor systems. In this way, it reduces the weight and saves cost by reducing the amount of cables in the car without reducing the robustness of the system, allowing to increase the number of sensors in the car, reduce risks and increase safety.

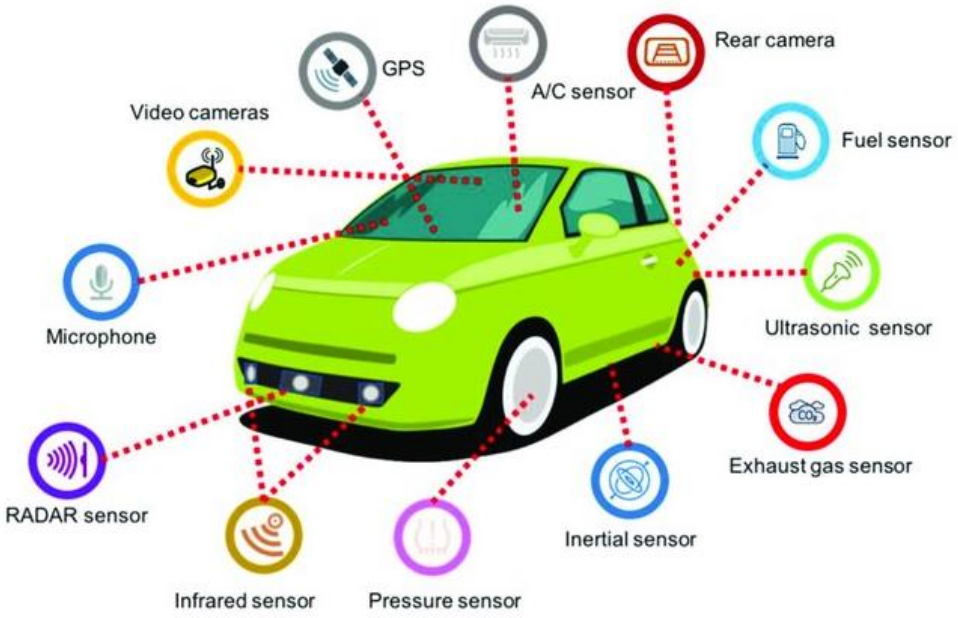

Figure 2. Modern automotive vehicle sensor applications. Image form "Sensor Technologies for Intelligent Transportation Systems", Guerrero-Ibáñez et.al. [25] / CC BY.

Much of the research for VEHs in vehicles is focused on areas where there is a large amount of available energy. These areas are primarily the vehicle suspension [26], wheel rotation [27] and on-engine vibrations [19,28,29].

VEH drawing power from the vehicles suspension system are typically based on an electromechanical transduction element placed in parallel with the vehicles shock absorbers. A review of the various designs implemented in this regard is given by Abdelkareem et al. (2008 [26]), Caban et al. (2023 [30]) and Reddy et al. (2024 [31]). Ali et al. (2023 [32]) provide a thorough review of the research field during the past two decades. Zhao et al. (2019 [33]) describe a system where the parallel electrical damping is achieved by a piezoceramic cylinder connected via a lever with variable pivot point. This design allows the force transmitted to the piezoceramic to be adjusted. The average measured power was 19 W driving at 60 km/h. Zhao et al. (2019 [34]) and Alhumaid et al. (2022 [35]) implement motion conversion from axial to rotation together with varying magnetic force exerted on piezoelectric elements. Zhao et al. test their system under real road condition, measuring an average power of 25 W driving at 60 km/h. The VEH by Alhumaid et al. generates only 0.95 mW but is only tested in lab conditions with a small vibration frequency and amplitude. An axisymmetric cylindric EMEH for suspension damping is implemented by Zhou et al. (2022 [36]). It uses a stack of two magnets moving within a stack of coils. Iron components are added to guide the magnetic flux

and increase the magnetic field gradients within the coils. The EMEH generates 240 mW at 3.3 Hz with a displacement amplitude of 2 mm.

VEHs in tires can scavenge energy from one or a combination of sources, such as tire deformation, the alternating relative direction of gravitational pull and road vibrations. A strain based PEH, embedded on the inner surface of the tire, is described by Esmaeeli et al. (2019 [37]) and they state their VEH generates 24 μJ per revolution, which at 40 km/h leads to an average power output of 0.12 mW. Seo et al. (2019 [38]) implements an EMEH with nonlinear magnetic springs, placed vertically aligned on the inner surface of the tire, scavenging energy from impacts and vibration. The lab-based measurements showed a power output of 5.8 mW at 60 km/h. An EMEH converting the wheel rotational energy through a plucking mechanism, developed by Miao et al. (2022 [39]), generates an average power of 13 mW at approx. 20km/h.

The power output from PEH externally placed on some surface of the engine has a significant dependance of the engine rpm [19,28,29]. Gao et al. (2017 [28]) implement a rod with seismic mass to induce strain in a stack of piezo discs, which generates 30 μW under lab conditions (at 60Hz and 1g acceleration) and 0.4 μW on the engine (after engine has achieved a stable state). To increase the bandwidth, Koo et al. (2021 [29]) use a double cantilever PEH, which delivers 0.248 mW under lab-conditions with 1.2 g excitation corresponding to running an engine at 3200 rpm. The corresponding field measurement shows only 0.038 mW. The PEH by Pepe et al. (2022 [19]) consists of a single cantilever beam but utilizes a maximum power point tracking (MPPT) scheme to enhance power output. An average power output of 2.8 mW is achieved in simulations, using vibration data as measured on the engine.

An EMEH using a non-linear mechanical spring for bandwidth widening and MPPT for power optimization is described by Paul et al. (2021 [40]). The VEH performance is evaluated on the rear part of the vehicle, in the context of a complete system powering a temperature sensor and a humidity sensor. Under harmonic excitation in a lab, the EMEH produced an average power of 552 μW under 0.5 g acceleration.

Table 1 lists the above mentioned VEH together with some characteristic parameters. As the size and applications vary to a large degree, we list the output power “as is” (not normalized by size). VEH coupled to the suspension system naturally produce large output power as they can make use of the large vehicle mass. VEH in tire applications are typically small (due to restrictions meant to maintain tire performance). Their power performance is moderate and again there is a coupling, to some degree, to the vehicle mass. The VEH making use only of their own inertia, used on engine, chassis and passenger compartment, also produce the overall lowest power. In this class of VEH, the EMEH described in paper I shows good performance as it has competitive power output together with a large bandwidth. The EMEH of paper I is also the only VEH in table 1 with the possibility of resonance frequency tuning, i.e. the potential of real time control of the resonance frequency over a significant frequency range. Such tuning capability is an attractive property in automotive applications, where the vibrations spectrum will depend on vehicle speed.

Table 1. Summary of VEH developed for use on vehicles.

Type	Avg Output power – lab	Size [cm³]	BW [Hz]	Tip Mass	Lab conditions Acc. @ Freq.	Output power – field	Reference
PEH	30 µW	60[1]	8	100 g	1 g @ 60 Hz	0.4 µW	[28] - engine
PEH	0.248 mW	1.1	6[2]	1 g	1.2 g @ -	0.357 mW	[29] - engine
PEH	1.6 mW	3[1]	4.5	16 g	1 g @ 127 Hz	2.8 mW[3]	[19] - engine
PEH	-	150[1]	-	-	-	19 W[4]	[33] - suspension
PEH	-	6700[1]	-	-	-	25 W[4]	[34] - suspension
PEH	0.95 mW	2100[1]	>5	-	0.23 g @ 2.5 Hz	-	[35] - suspension
EMEH	240 mW	630[1]	-	4.2 kg	0.09 g @ 3.3 Hz	210 mW[3]	[36] - suspension
PEH	0.12 mW	0.32	-	-	40 km/h (5 Hz)	-	[37] - tire
EMEH	5.8 mW	4.1	-	-	60 km/h	-	[38] - tire
EMEH	13 mW	3	-	-	20 km/h (3 Hz)	-	[39] - tire
EMEH	0.55 mW	4	9	2.7 g	0.5 g @ 79 Hz	-	[40] – chassis
EMEH	1.1 mW	19	14	180 g	0.13 g @ 47 Hz	52 µW[3]	paper I - buckle

[1]Rough estimate of size, [2]Assumed, based on author statement. [3] Simulated, based on field data.
[4] Simulated, based on field data, 60 km/h, road class B.

1.3 Vibrational energy harvester system

A complete VEH systems consists of additional parts other than the transduction mechanism (see Figure 3 right). The standard components are rectification, filtering, regulation and storage.

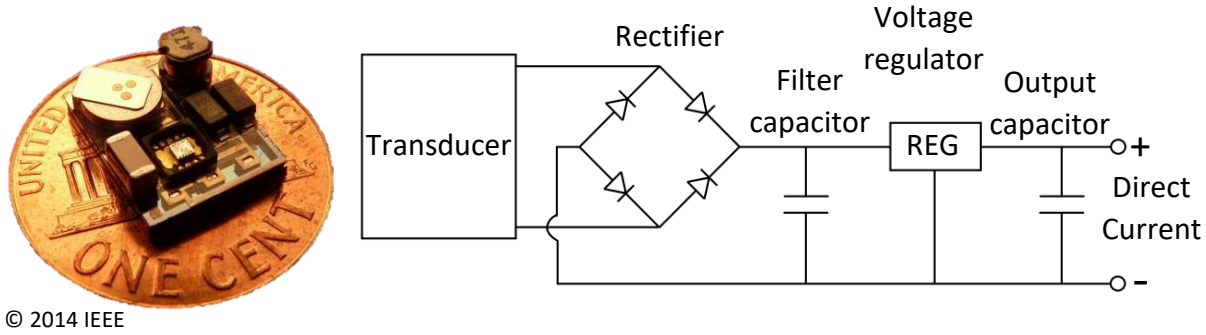

Figure 3. Left: A complete VEH system [41]. Right: Typical components required by a VEH other than transduction.

As the VEH converts mechanical oscillations the resulting current and voltage are typically of alternating polarity. As integrated circuits (ICs), such as a processor, require a direct current (DC) power supply the VEH output must be rectified, i.e., the polarity must be constant. A constant polarity does not imply constant voltage, only that it is of the same sign over time. This can be achieved by either excluding parts of the generated voltage or converting the sign. There are a number of methods to rectify a signal, either mechanically [42] or electrically e.g. by use of diodes. A common approach is a full wave rectifier bridge as seen in Figure 3, which converts the voltage to be of the same sign.

The rectified VEH output voltage is then filtered by a capacitor to remove some of the signal variation. The voltage level is here still proportional to the amplitude of the voltage generated by the VEH transduction mechanism, which in turn depends on the ambient energy source. The unreliable voltage level together with the remaining oscillations prohibit the use of most electronics.

The filtered signal must therefore be regulated, which results in a constant DC voltage as long as the average ambient power is large enough relative to the power consumption of the load. There are numerous commercial ICs which perform voltage regulation, ranging from simple Zener diodes to highly energy efficient pulse width modulation units.

Most sources of ambient energy will vary significantly in strength and can likely be below a usable threshold in recurring periods. To maintain continuous operation, the system will require stored energy which can be used during the periods of low source energy. A capacitor at the output of the VEH regulator can fulfill this task and additionally handle any power spikes which may appear in the load circuit. Important characteristics of the charge storage unit are self-discharge rate, capacitance per gram and the number of charge/discharge cycles before failure. There are a few types of storage units which may be used, each with certain pros and cons. One promising technology is the supercapacitor, an electrochemical capacitor with high capacitance. Its most beneficial characteristics is that it allows for a very large number of charge/discharge cycles [43].

It is also likely that the average ambient power is overall too low to power the desired electronics continuously. The alternatives are then to either run the application intermittently (when enough energy has been harvested) or implement a secondary battery. The VEH can then extend the lifetime of the battery by recharging when possible. The number of recharge cycles is however still limited in current state-of-the-art batteries, although advances have been made in this regard [44].

It may be necessary to include a voltage amplifier (charge pump) prior to the rectifier as many rectifiers inherently lead to a reduction in voltage. To maximize power generation, it is also necessary to regulate the load impedance [19].

1.3.1 Transduction mechanisms

There are several mechanisms which can be used to convert kinetic energy to electricity. Depending on the intended application each mechanism can be more or less suitable. Temperature sensitivity, tensile strength, complexity, and scalability are some properties which can differ between transducers and can determine which to choose for a certain application.

Mechano-electric materials exhibit useful changes in electrical properties when put under mechanical stress. Piezoelectric and electrostrictive materials are mechano-electric and give rise to charges under applied stress, which can be used to directly convert mechanical or kinetic energy to electric energy (Figure 4 left). Another example is a magnetostrictive material, that changes in magnetization when under mechanical stress, which together with a magnetic field bias (Figure 4 middle), can be used to induce magnetic field variations in a coil and thus induced voltage [45,46].

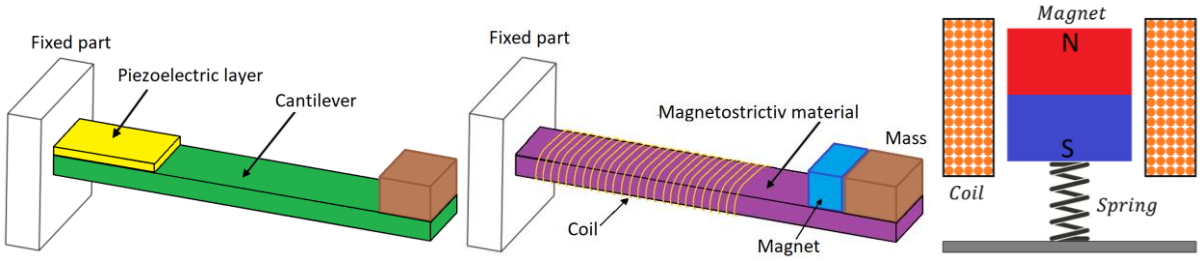

Figure 4. Left: piezoelectric cantilever with piezoelectric layer (yellow), flexible beam (green) and proof mass (brown). Middle: Magnetostrictive cantilever with coil wound magnetostrictive material, tip mass and permanent magnet. Right: Basic electromagnetic energy harvester with cylindrical magnet oscillating along coil axis [47].

Electromagnetic induction relies on Faraday's law, which relates the change in magnetic flux with time in a closed loop to electromotive force (EMF), which in turn can drive an electrical current in a coil connected to a load. This can be achieved by, e.g., the relative displacement between coil and magnet (Figure 4 right).

Triboelectricity refers to the charge generated due to charge transfer between two different dielectric material surfaces in contact. After being brought out of contact, the induced charge difference can be used to generate a current between electrodes. The motion between surfaces can be either vertical (Figure 5 left) or horizontal. A review of triboelectric energy harvesters is given by Wang (2013 [48]) and more recently by Munirathinam et al. (2023 [49]).

Electrostatic energy harvesters (Figure 5 right) make use of an initial charge within two surfaces separated by a dielectric (such as air). The initial surface charges can either be induced by an external charge source or by incorporating a charge-doped material in-between the surfaces [50]. If an external charge source is used, the charge must be injected when the distance between the surfaces is minimal, i.e. the capacitance between the surfaces is at a maximum. After charge injection, one approach is then to electrically isolate the surfaces to maintain the charge (open circuit condition). Mechanically increasing the distance between the surfaces leads to a reduction in capacitance and thus an increase in potential between the surfaces. This potential is then used to drive a current and produce electrical power.

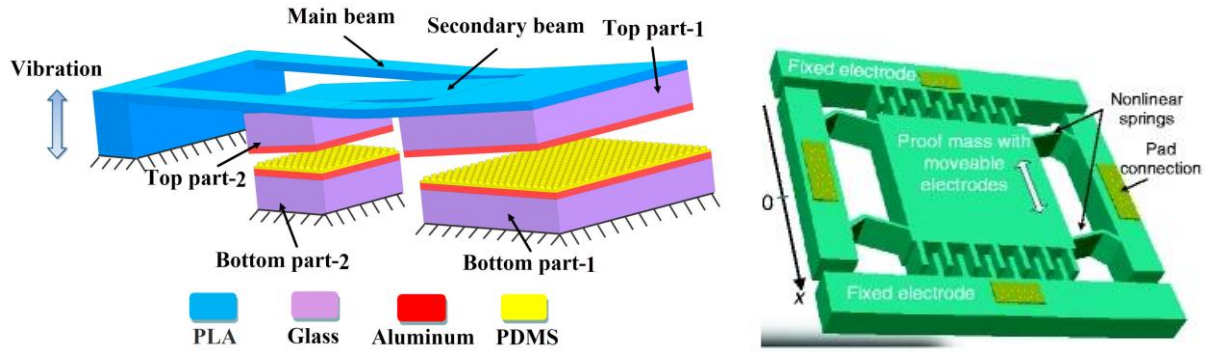

Figure 5. Left: Triboelectric cantilever with vertical motion between triboelectric layers [51]. Right: Electrostatic energy harvester [52].

In this thesis we will be focusing on piezoelectric and electromagnetic (inductive) vibrational energy harvesting.

1.4 Optimization of power output

Most research in vibrational energy harvesting focuses on maximizing the power output. What this entails varies depending on the application.

Any VEH with an elastic component (equivalent to a spring) will generate peak power at one or two specific frequencies (resonance frequencies). Power optimization can in this regard be achieved by matching the VEH resonance frequency with the largest frequency component of the ambient vibration. Active or passive tuning schemes can also be implemented to continuously optimize the resonance frequency. The frequency spectrum of ambient vibrations will inevitably have some spread, thus achieving a wide resonance peak (i.e. large bandwidth) is also beneficial. Implementing non-linear behavior is a method which can be used to adjust the frequency range up or down as well as increase bandwidth. Examples of mechanism to induce non-linearity are bistability [53], stoppers [54], spring non-linearity [55,56] or non-linear damping [57].

There is also an optimal value of the electrical impedance of the load which is connected to the VEH. Deviation from this optimal value will either lead to a low total extracted power or most power being dissipated within the VEH. For a PEH, which can be modeled as current source in parallel with an intrinsic resistance, a load impedance which is too large will lead to most generated power being dissipated within the VEH, instead of the load. For an EMEH, which can be modeled as voltage source in series with an intrinsic resistance, this is the case when the load impedance is too small.

Simply maximizing the power generation performance assumes there is enough ambient energy to supply this power. For cases where the ambient energy is very small it may be that most power is generated by maximizing conversion efficiency.

1.4.1 Resonance and anti-resonance

Resonance is the effect of an amplified response in an oscillating structure. Any non-rigid structure, subject to a periodic force can exhibit resonance. Exciting the structure with a frequency equal or close to (depending on mechanical damping) its natural frequency will lead to resonance (conceptually illustrated in Figure 6). A simple explanation of the natural frequency is that it is the frequency at which the structure would vibrate if hit (or plucked in the case of a guitar string). In reality it is a bit more complicated as the structure will have a number of “harmonics” at which the excitation frequency also leads to resonance. There is also the possibility of the structure having multiple degrees of freedom. A beam may for example both bend and twist. If, in this case, the bending and twisting are dependent of each other we have a system of two coupled oscillators. There can be any number of coupled oscillators in a vibrating structure and for each coupled oscillator, the structure will exhibit an additional resonance peak. We could complicate this further by again considering the higher order harmonics for each oscillator.

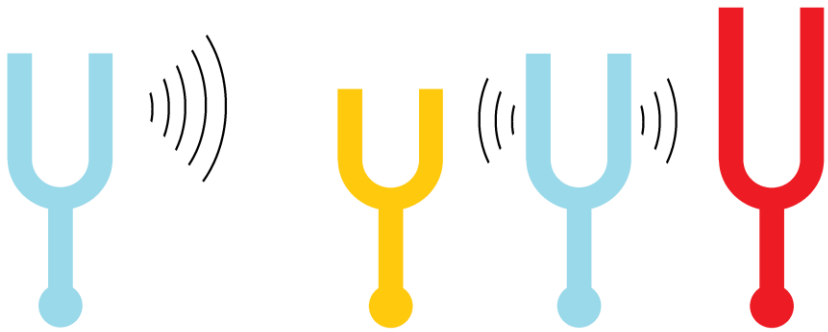

Figure 6. Basic principle of resonance between tuning forks. The soundwaves produced by hitting the blue tuning fork will only induce resonant vibrations in the receiving tuning fork having the same natural frequency.

When analytically modelling a VEH it is often simplified as a single degree of freedom (SDOF) mechanical oscillator coupled to an electrical domain. The electrical domain is typically also idealized and contains only one reactive component (a capacitance in the case of a PEH and inductance in the case of an EMEH). As an electrical oscillator requires both an inductance and capacitance, the idealized VEH in the electrical domain is not an oscillator. Based on this modelling a VEH will only have one resonance frequency (with high order harmonics still possible).

As described in paper II of this thesis, a SDOF VEH can be designed to have two power peaks as a function of excitation frequency. The second peak is a result of the systems anti-resonant frequency. While the resonant frequency corresponds to the systems state of minimum impedance (i.e., an oscillation amplitude maximum), the anti-resonant state corresponds the state of maximum impedance (oscillation amplitude minimum). The anti-resonant state occurs when the VEH exhibits a maximum in damping, which occurs when the transfer of energy, from the mechanical domain to the electrical domain, is at a maximum. This is equivalent to a maximum in electrical damping. An example of measured resonance and anti-resonance in a PEH is given by Colin et al. (2013 [58]). A further explanation of resonance and antiresonance, and their relations, can be found in the IEEE Standard on Piezoelectricity [59] or in the textbook by Priya and Inman [60]. Although the explanations are centered around PEH they hold for any VEH. Some expressions must be modified to account for differences in equivalent circuit representations between various VEH, e.g. replacing the parallel capacitance and parallel dielectric resistance in a PEH with a series inductance and series coil wire resistance in a EMEH.

1.4.2 Stochastic resonance

The forms of resonance described in the previous section are based on harmonic base excitation. In reality the base excitation of a VEH will often be noisy to a large degree, but with possible harmonic components. This type of vibrational environment can be ideal for a VEH implementing stochastic resonance.

Stochastic resonance can only be utilized in a bistable or multistable VEH, i.e. a VEH with at least two states of minimum potential energy. The benefit of such a system in a noisy environment is that a sufficient noise level can induce oscillations between the two potential

minima, when the harmonic component is too small. The theory of stochastic resonance is explained in detail by Rajasekar et al. (2016 [61]). A practical example using a snap-through buckling beam for bi-stability is given by Ando et al. (2020 [62]). Chapter 2.2 gives an in-depth example of a bi-stable rotational VEH utilizing stochastic resonance.

1.4.3 Impedance matching

From electrical circuit theory it can been derived that there is an optimal resistance of the load connected to the energy harvester (see paper II), at which most power is dissipated by the load. For a non-optimal load, a significant portion of the energy generated by the VEH will be dissipated as heat by the intrinsic impedance of the VEH. The expression for intrinsic impedance differs between different types of VEH. For an EMEH the impedance is a result of an inductance in series with the coil wire resistance. For a PEH it is a capacitance in parallel with a resistance resulting from two parallel plates (the electrodes) and a dielectric (the piezoelectric material) in between.

Only taking into account circuit theory, the optimal load resistance would equal the VEH equivalent circuit impedance. It can however be derived that for a VEH one must also include a term proportional to the electrical damping of the system. For the simplified case of a purely resistive load, the frequency response of the VEH and at the load are equal. Adding a reactive load will affect maximum power output and the frequency at which the power is at an optimum [63]. This thesis focuses on the performance of the energy transduction mechanisms of the VEH and does not go into any depth regarding power management, in which case a reactive load should be considered.

Both impedance and electrical damping are frequency dependent. For a practical case, where the excitation frequency is likely noisy and shifting it is typically beneficial to have a dynamic and adaptive load. Maximum power point tracking (MPPT) is based on this idea and is well established in literature [64] and can be found as a feature in commercial power management units. MPPT can be described as a technique to adjust the impedance of the load such that it continuously matches the impedance of the VEH as the excitation frequency varies. There are numerous ways to achieve this (as described in [64]). As an example, adjusting the duty-cycle of a pulse width modulated power converter (operating in discontinuous mode), can be used to emulate a controllable resistance.

1.5 Scope

The scope of this thesis is to explore the use of piezoelectric and electromagnetic vibrational energy harvesters as power source for sensors in vehicles. The thesis will also describe the basic principles and characteristics of these systems. The thesis will not evaluate the complete VEH system in detail and will thus not delve into the research regarding rectification, impedance matching, power management or energy storage.

Chapter 1 of this thesis introduces vibrational energy harvesting in general and its applications in the automotive industry. An overview of a complete VEH system is given and the key characteristics are explained.

Chapter 2 describes the fundamental principles of the piezoelectric effect and gives a review of its implementation for sensors in vehicles. The design, implementation, and results for a PEH utilizing stochastic resonance to power a strain sensor on an engine flex plate, is also described.

Chapter 3 describes the fundamental principles of magnetic induction and magnetostriction and gives a review of their respective implementations. The design, implementation, and results for two distinct EMEH powering a sensor on a belt buckle are described here. A potential performance improvement by synergistically implementing magnetostriction is also explored.

Chapter 4 presents analytical modeling methods based on lumped and distributed models and gives an in-depth analysis of the results of such modelling for piezoelectric and electromagnetic energy harvesters.

Chapter 5 gives a discussion, conclusion and description of future work to be done, based on the results and experiences gained from the current thesis work.

CHAPTER 2

Piezoelectric energy harvesters

2.1 Introduction to piezoelectricity

Piezoelectricity, the phenomenon where certain dielectrics become polarized under tension or compression and vice versa, was first demonstrated by the brothers Jacques and Pierre Curie in 1880 [65]. Their discovery was a result of their research into pyroelectricity, where they examined the polarization effect in semi-symmetrical crystals due to heat. They found that a polarization could also be achieved by applying pressure along certain axis of the crystal. The first practical serious application of this physical phenomenon was in Sonar devices during the first world war [66]. The Sonar was invented to detect submarines, utilizing a piezoelectric element to both generate and measure acoustic under water waves. Since then, piezoelectric elements have found many uses as sensors, actuators and energy harvesters. Perhaps one of the most important uses is as a clock generator for processors, without which they would not function.

To possess the property of piezoelectricity the material must have a non-centrosymmetric arrangement of its atomic or molecular structure [67]. Centro-symmetry refers to structures which are identical on opposite sides of an axis, for any given point. Figure 7 shows a simple model for an intuitive explanation the piezoelectric effect in crystals, proposed by Meissner A. in 1927 [68]. The model is based on quartz, which has a unit cell structure that is non-centrosymmetric. Under stress-free conditions the unit cell is neutral but becomes polarized when subject to tension or compression. The natural crystal structure in quartz is such that the polarization of unit cells is aligned through the material, thus leading to a net polarization in the bulk of the material.

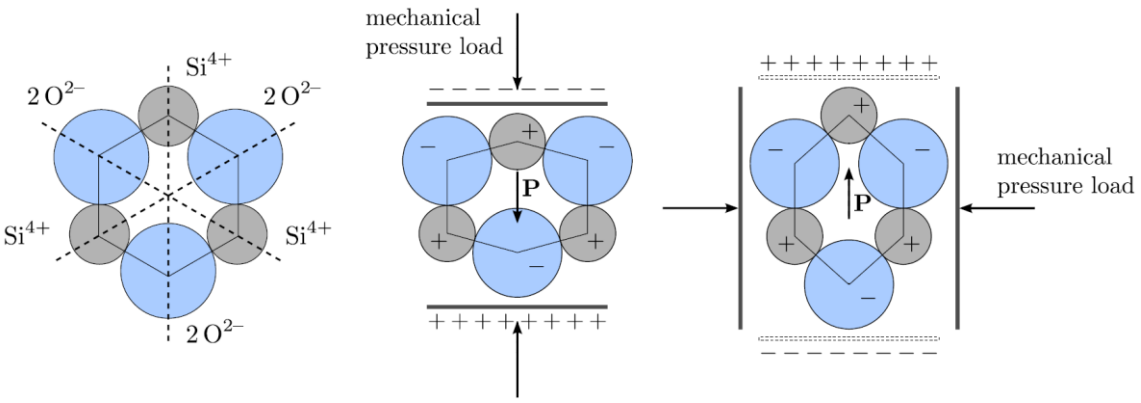

Figure 7. Crystal unit cell model for quarts and the effect of applying pressure [69].

Piezoelectricity can also be induced in some ceramics. These ceramics have crystal unit cells which become non-centrosymmetric and form dipoles under a certain, material dependent, temperature [70], also called the Curie temperature. An equivalent definition of the Curie temperature is the temperature at which the material undergoes a phase change between being ferroelectric and paraelectric. Examples of such ceramics are perovskite, lead titanate (PTO) and lead zirconate titanate (PZT), all of which have the same structure (see Figure 8). Within the ceramic material there will be regions where the electric dipoles are approximately aligned. Such a region is called a Weiss domain. The orientation of Weiss domains in an untreated ceramic may be weakly aligned. By applying a strong electric field over the ceramic, while keeping it heated to facilitate domain movement (although below the Curie temperature [71]), all the Weiss domains can be aligned (a process also called poling). After cooling, the alignment is to a high degree maintained. The ceramic will now behave similarly to quartz, as modeled in Figure 7. Compared to quartz however, the piezoelectric ceramics mentioned above can achieve a much stronger piezoelectric effect.

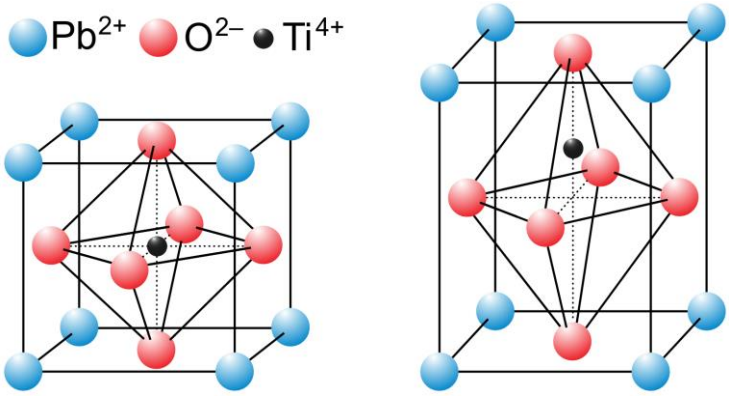

Figure 8. Left: PTO above the curie temperature with centrosymmetric unit cell. Right: PTO below Curie temperature with non-centrosymmetric unit cell [70]. Image source [72].

Piezoelectricity is not restricted to occurring in crystalline materials [67,73]. The phenomenon has been observed naturally in some polymers such as DNA and various proteins and can also be induced in synthesized polymers, such as PVDF and PVDF-TrFE [74]. To make use of the generated charge, electrode material must be deposited on both sides of the piezoelectric material. The electrodes will naturally reduce the strain produced in the piezoelectric material and act as a performance reducing capacitance. Both the electrode material composition [75,76] and spatial configuration [77] can be optimized.

The piezoelectric effect goes both ways; applying stress in the material generates an electric displacement and applying an electrical field generates strain within the material (compression or tension). Stress to charge is called the direct piezoelectric effect. Electric field to strain is called the inverse/converse piezoelectric effect.

An important characteristic of the piezoelectric effect is that it is linear [66] (unlike the similar electrostatic effect which is cubic). A constant defining this linear proportionality is the piezoelectric constant, d, coupling the electric charge density displacement D to stress T and strain S to electric field E. Considering the 3 dimensions of space and rotation in each dimension, d becomes a 3rd rank tensor, D and E are 3×1 vectors and T and S are 3×3 matrices.

d is transposed for the inverse piezoelectric effect. These linear relationships are given by Equation (1) and Equation (2).

$$D_i = d_{ijk} T_{jk} \quad (1)$$

$$S_{ij} = d_{kij} E_k \quad (2)$$

To derive the actual charge displacement or strain we must include the effects from the elastic and electric nature of the material. For the inverse effect we include a term according to Hooke's law (Equation (4)) and the natural relationship between charge density displacement and electric field within any dielectric (Equation (3)). Here ε is the dielectric permittivity, a 3×3 matrix, and s is the elastic compliance, a 4th rank tensor.

$$D_i = \varepsilon_{ij} E_j \quad (3)$$

$$S_{ij} = s_{ijkl} T_{kl} \quad (4)$$

The constitutive strain-charge equations (Equations (5) and (6)) describing the piezoelectric material is given by the combinations of Equation (1) and (2) and Equation (3) and (4). The tensor ranks can be reduced by using Voight notation in which the rotational elements are combined, e.g., $T_{11} \rightarrow T_1$, $T_{22} \rightarrow T_2$, $T_{23}\ and\ T_{32} \rightarrow T_4$, $T_{13}\ and\ T_{31} \rightarrow T_5$ and $T_{12}\ and\ T_{21} \rightarrow T_6$. T and S can now be expressed by 1×6 vectors, d as a 3×6 matrix and s as a 6×6 matrix. To clarify, using Voight notation, indices 1 to 3 correspond to the 3 dimensions of space, while indices 4-6 correspond to rotation.

$$D_i = d_{ij} T_j + \varepsilon_{ik} E_k \quad (5)$$

$$S_j = s_{jl} T_l + d_{ji} E_i \quad (6)$$

It is important to note that the values of ε_{ik} and s_{jl} are those derived under the absence of piezoelectric effects. ε is derived under zero or constant stress, equivalent to unclamped or mechanically free conditions and s is derived under zero or constant electric field, equivalent to open circuit conditions [78].

2.2 Piezoelectric energy harvester research

In the early days of piezoelectric research, the viable applications where limited due to the few available piezoelectric materials with notable electromechanical coupling (typically quartz or Rochelle salt). With the discovery of barium nitrate and later PZT a significant improvement in coupling factor was achieved. These were ceramic materials with which the composition could be tailored to suit the need of the application.

The "thin film cantilever beam" is today the most commonly applied type of piezoelectric energy harvester. It consists of a substrate (often silicon) with a thin film of piezoelectric material deposited on top (typically PZT). Some reasons for the cantilevers popularity in this sense could be the relative simplicity in design and the possibility to accurately predict the

system characteristics with a combination of Euler-Bernoulli beam theory (see chapter 4) and the constitutive strain-charge equations.

The basic cantilever configuration has some drawbacks. The resonance frequency typically increases with decreasing size, as the beam length gets shorter. Compensating by reducing thickness leads to a reduction of the generated charge. The bandwidth is also relatively small in comparison to the width of an *in situ* vibration spectrum. Thus, research focuses to overcome these drawbacks by various methods. The following paragraphs will give examples of macro-sized VEH implementing different methods to optimize the frequency response.

A fairly straight forward approach to increasing the bandwidth is implemented by Kim et al. (2020 [79]). The electrodes of four single layer thin film PZT cantilever beams, each with a shift in natural frequency, are connected in parallel in the electrical domain. The frequency response of each is essentially superimposed, leading to a large increase in the frequencies where a useful power output can be achieved. Using an array configuration where all the PZT layers are facing the same direction (e.g. “up”) leads to four separate bands of viable power. By alternating PZT layers with face “up” and face “down”, the power in-between the resonance peaks can be increased to viable levels, at the cost of peak power. As an example, one of the array configurations achieved two full width at half maximum (FWHM) bands of 8 Hz with a maximum average power of 6.3 mW at 1.5 g excitation (in the range 110 Hz-130 Hz). A related approach is to use multiple beams coupled in the mechanical domain as well as the electrical domain, as described by Bouhedma et al. (2020 [80]). This system also implements magnetic coupling for active frequency tuning. A power output of 0.5 mW at 0.5 g is achieved with a combined bandwidth of approx. 7 Hz.

The review of magnetically coupled PEH, by Jiang et al. (2021 [81]) gives several examples of different magnetic coupling schemes leading to monostable, bistable and multi-stable systems. Each of these can be used to tune the frequency response. The bistable and multi-stable configurations have the benefit of larger mass-displacement due to inter-well oscillations. Sun et al. (2022 [82]) describe a PEH which achieves quad stability by the force interaction between a ring magnet and square magnet. The prototype of this PEH shows a measured power output of 19 μW at 1.5 g.

Non-linear characteristics in a VEH can also be achieved by mechanical springs with non-linear stiffness, typically achieved by a certain geometry of the spring. The PEH by Pertin et al. (2022 [56]) implements a tapered mechanical spring. An output power of 0.26 mW at 0.9 g is achieved, with a bandwidth of approx. 20 Hz. An orthonormal planar spring is used in the PEH by Dhote et al. (2019 [83]), which achieves a bandwidth of 35 Hz at 0.8 g excitation amplitude. The bandwidth is in this case defined as the band in which 4V open circuit is maintained. Chen et al. (2022 [84]) describe a PEH with a relatively large bandwidth of 13 Hz, considering the center frequency of approximately 40 Hz. This PEH uses perforated segments of a clamped-clamped beam to achieve non-linear stiffness. An average output power of 0.184 mW is achieved.

In the review articles by Wakshume et al. (2024 [85]) and Tabak et al. (2024 [86]) piezoelectric microfiber composites are noted as a viable solution to overcome the brittleness and non-

conformity of bulk ceramics, while maintaining a large piezoelectric effect. Wakshume et al. also describes auxetic structures, which increase in size in the dimension orthogonal to an applied tension, as a key enabler for increasing performance of piezoelectric VEH.

Wang et al. (2024 [87]) describe a system of vertically stacked, coupled, cantilever beams with piezoelectric patches. The end of the stack is connected to a magnetic proof mass. The proof mass movement is restricted to one dimension. A separate set of static magnets lead to a tri-stable system. This VEH achieves a power output of 1.49 mW within the frequency range of 2–9.5 Hz at an excitation of 0.4 g.

Table 2 gives a sample of piezoelectric VEH together with some characteristic parameters. Various beam structures and configurations are included. The set of power densities show a large variance, which may in part be due to large differences in the amount of active material. For example, the VEH by Kim et al. [79], has about 6 times the amount of piezoelectric material as the VEH by Bouhedma et al. [80] and the about 18 times the amount of active material as in the VEH by Dhote et al. One must however also consider that a portion of the active material will have a very small contribution to the transduction of energy. The low profile of piezoelectric VEH also lead to large differences in size, as some include a block-shaped proof mass and some do not. Taking these considerations into account, as well as the differences in tip mass weight and excitation acceleration, would likely reduce the variance in performance. The VEH with multiple beams naturally achieve larger bandwidth, but typically have either large footprints [79] or slender structures with small regions of active material [83]. The VEH in table 2 using structured springs [56][84] achieve large bandwidth in a more size efficient way. The VEH described by Forsberg et al. shows that a simple cantilever beam with tip mass can have a power density comparable with more complex systems, if subject to both rotation and vibration.

Table 2. Summary of reviewed piezoelectric energy harvesters.

Harvester type	**Power density [μW/cm³]**	**Size [cm³]**	**BW [Hz]**	**Tip mass [g]**	**Conditions acc. @ freq.**	**Ref.**
Auxetic structure	5.5	33	13	10.4	0.3 g @ 51 Hz	[84]
Auxetic structure	5.5	33	13	10.4	0.3 g @ 51 Hz	[84]
Stacked beams	26.5	56.3	5	-	0.4 g @ 9.5Hz	[87]
Tapered spring	37.1	7	20	3.8	0.9 g @ 175 Hz	[56]
Stochastic resonance	63.8	5.8	2.4	5	1 g @ 10.5Hz	[88]
Multi-beam	69.4	7.2	7	15.2	0.5 g @ 63 Hz and 76 Hz	[80]
Multi-beam	414.5[2]	15.2[1]	16	-	1.5 g @ 112 Hz, 117 Hz, 123 Hz, 128 Hz	[79]

[1] Beam size with 1 mm added to account for electrodes and tip displacement [2] Averaged over four resonance peaks, [3] Frequency band in which 4V open circuit is maintained. Likely optimistic value compared to FWHM.

2.3 Piezoelectric energy harvester for engine sensor

In any vehicle there are several rotating components. Rotations with an axis perpendicular to earths gravitational field allow for a simple mechanism to induce an oscillating force. For a small VEH with small proof mass the force amplitude is however quite small. The vibrations from road roughness and engine dynamics together with the small periodic gravitational force are a good combination for implementing a stochastic resonance VEH. The work described here [88] explores the possibility of using a simple cantilever beam on the engine flexplate to power a strain sensor (see Figure 9).

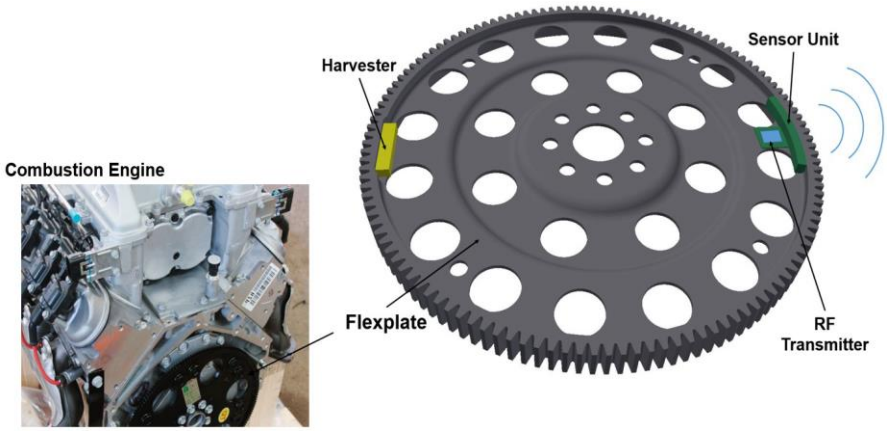

Figure 9. Placement of stochastic resonance VEH and strain sensor on flexplate within engine.

In rotating systems there are multiple sources of excitation that can be harvested, such as alternating gravity direction, centrifugal force and the rotational movement itself, all well defined by the rotation speed. There are various designs of rotational VEH in the literature. Wang et al. (2012 [89]) utilize magnetostatic coupling between the static and rotating parts [90]. Li et al. (2011 [90]) describe a VEH mounted entirely on the rotating part of a system, using a magnetostrictive or piezoelectric transducer and the alternating gravity of the rotation as a source of excitation [91]. Gu et al. (2010 [91]) develop a passively tuned PEH using the centrifugal force to tune the resonance frequency [92] obtaining a tenfold increase in bandwidth when compared to a cantilever with constant axial force.

Another source of energy in these rotating systems is vibration that is exploited in a periodically modulated bistable system. This approach allows for higher energy output than monostable systems under the same excitation, e.g. by using a piezoelectric cantilever with a magnet tip mass combined with another magnet [92], or by increasing the bandwidth significantly compared to non-self-tuning concepts, when using the centrifugal force to achieve bistability [93,94].

The rotational PEH described in this chapter is a lightweight harvester mounted entirely on the rotating part, with dimensions of 40×8×6 mm^3. The concept is based on a piezoelectric beam with a proof mass that is inwards oriented to create a bistable system using centrifugal force as schematically shown in Figure 10. This design allows the harvester to be much smaller than previous designs [92,94] as it does not need any magnets to create the bistable system nor the coils for power generation.

The simulations of the rotational PEH were performed in both COMSOL and MATLAB using the values of a commercial 2-layer PEH with resonance at 98 Hz. The mentioned PEH was used in the experiments.

From the equation of motion simulated in MATLAB it can be seen that this system has a bistable behaviour (figure 11 left and right) where the velocity of the cantilever's end point is plotted against its displacement for the cases without and with white noise signal as vibration, respectively.

The simulations for power as a function of rotation frequency are presented in figure 12, where the values are averages of multiple runs as the occurrence of resonance is dependent on white noise and thus is random. The peak output is 370 µW and the bandwidth is 2.44 Hz (equivalent to a bandwidth of 146.4 rpm).

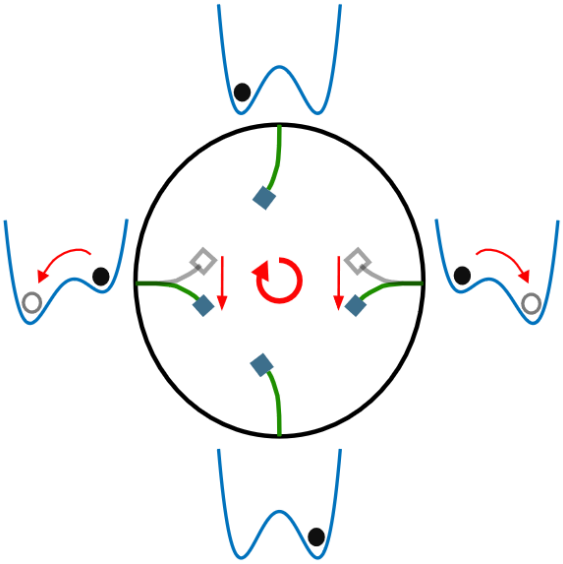

Figure 10. Schematic of piezoelectric cantilever positioning on the rotating part and visualization of the change in potentials during one rotation of a centrifugal force induced bistable system [88].

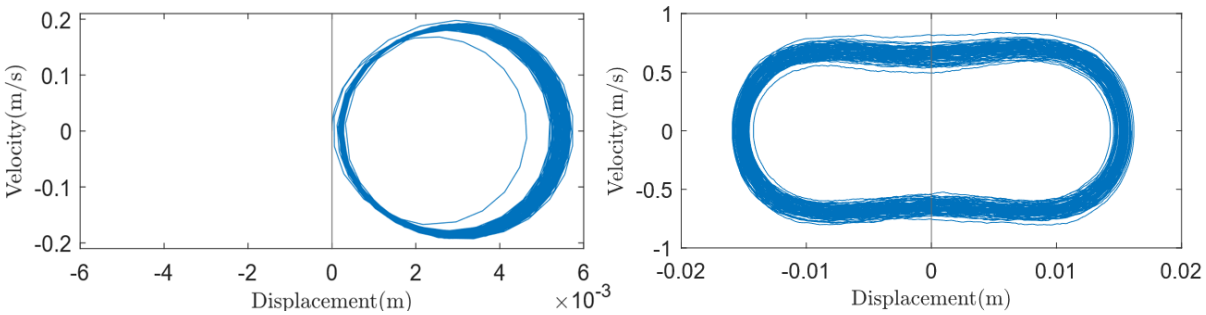

Figure 11. Left: Inter-well movement only due to vibrations; Right: Movement between stable positions under periodic forcing and vibrations [88]

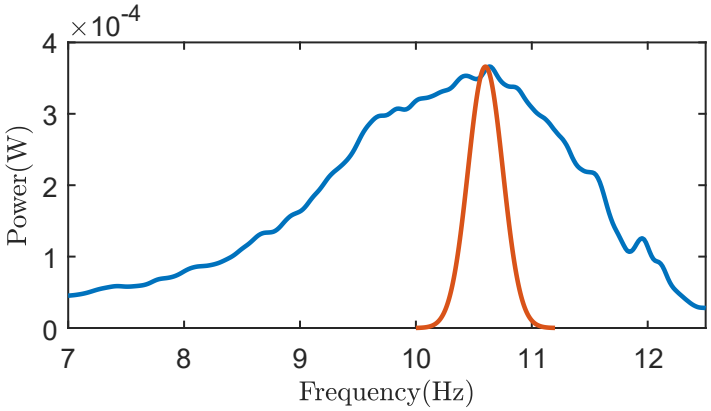

Figure 12. Increase in bandwidth (blue line) of the bistable EH as compared with a standard harvester (red line) having the same Q-factor as obtained from the measured damping ratio (normalized to match the power obtained in the simulations) [88].

To validate simulation results, lab measurements were carried out on a simple prototype. A miniature electrodynamic shaker (Modal Shop 2007E), driven by a SmartAmp power amplifier (Agilent 2100E21-100) was used to generate a sinusoidal excitation for the harvester. The response of the harvester was recorded using both an oscilloscope (PicoTechnology 2000 series) to measure the output voltage and a laser distance sensor (Panasonic HL-G1) to measure the displacement of the harvester (Figure 13 left).

Measurements were performed to compare the real bending of the cantilever beam to the theoretical calculations used in the simulations when a static force equivalent to the centrifugal force is applied to the harvester. Two measurements setups were implemented. The first was a simple setup, with the cantilever beam being pushed against an EKS Electronic Scale. The tip displacement and force could in this way be accurately measured (using the laser distance sensor) under static conditions. However, as the tip is in this case not strictly free, the results can contain significant error. For the second setup the harvester was placed in a rotating system with the proof mass facing inwards as seen in Figure 13 right. A DC motor (Micro Motors, RH158 12V) was used to drive the rotation, and the movement was recorded by a digital camera (Nikon D5300). In this case the beam tip is free. Although this setup replicates the centrifugal force of the real application, it was error prone in regard the measuring the tip displacement.

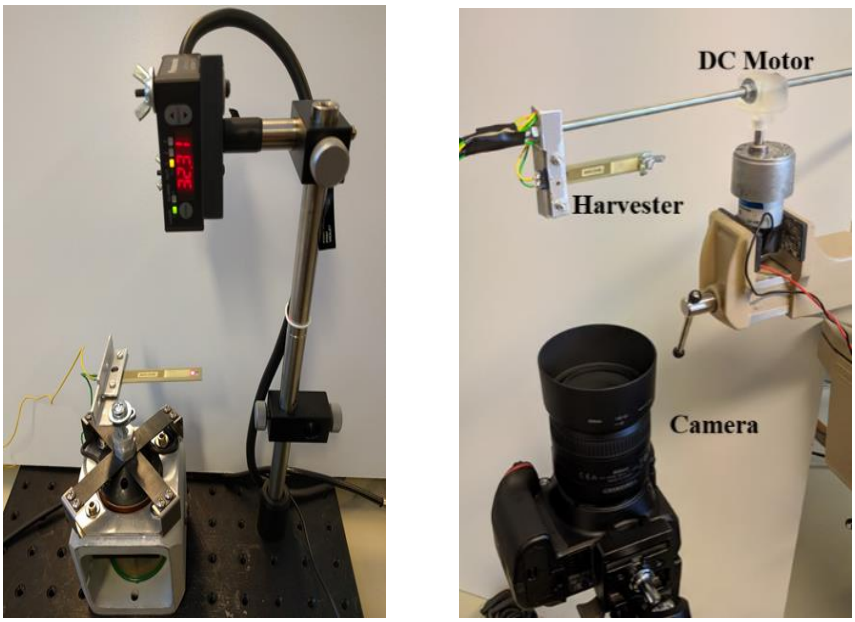

Figure 13. Left: Experimental setup for EH characterization. Right: horizontal rotation testing (The camera is pointing up) [88].

The resistance sweeps that were performed at resonance both in COMSOL and experimentally are shown in Figure 14, with the peak power at approximately 70 kΩ in both cases. The good agreement between these datasets indicates that the electrical characteristics of the COMSOL model are close to those of the experimental setup.

The theoretical values for the equilibrium positions as a function of rotation frequency are shown in Figure 15 with continuous lines. The experimental data shown in Figure 15 represents an empirical upper limit buckling frequency (red circle), the calculated lower limit of the buckling frequency (green circle), and the displacement at specific rotation speeds (blue circles). The experimentally determined buckling frequency, using the scale setup, will likely result in an overestimation as the movement of the beam tip is to some degree hindered by friction against the scale. The experimental displacement of the beam has increasing error margins with the rotation speed due to a too simple measurement setup. With this in consideration, the bistability simulations show good agreement with experiment.

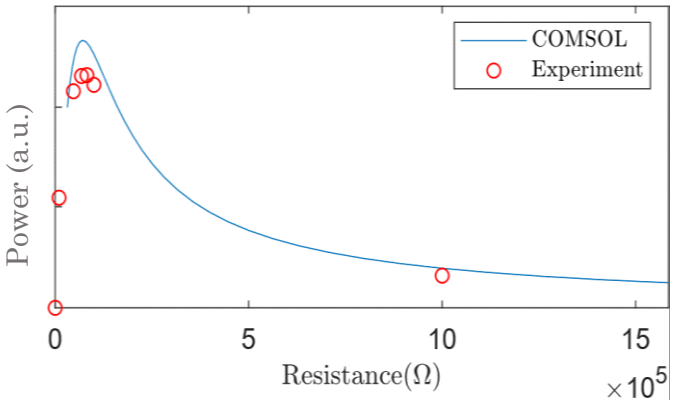

Figure 14. The resistance sweeps in COMSOL and experimental results showing the power at resonance dependent on resistance of a harvester without proof mass [88].

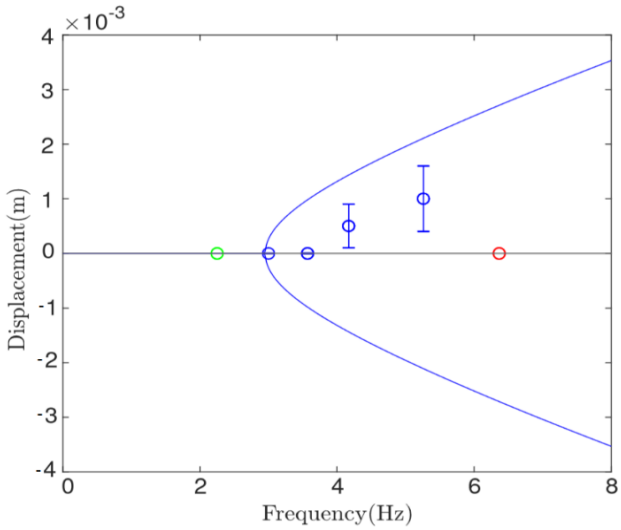

Figure 15. Theoretical (line) and experimental bending results for the displacement of piezo proof mass vs frequency. Red circle is the measured equivalent buckling frequency using the scale setup. Green circle is the calculated lower limit buckling frequency. Blue dots are the measured displacement in the rotating setup [88].

With the presence of a double potential as generated by the buckling of the harvester the difference in movement when comparing movement inside one potential well and movement between the potentials wells is significant. When comparing the results in figure 11 left and right, the top velocity is not only increased but also kept during a longer time as the distance is significantly increased as well. As the instantaneous power is dependent on the velocity squared there is no doubt that the occurrence of a bistable system, under periodic modulation, can increase the mechanical power available in a system.

The work described here provides a proof-of-concept for a miniaturized rotational energy harvester mounted on a flexplate. The results show that the vibrationally excited bistable EH, under periodic modulation, significantly increases power output compared to a monostable system. Likewise, an increase in bandwidth is gained from the passive tuning by centrifugal force. The EH described in this work is significantly reduced in size compared to similar state-of-the-art technologies, by utilizing an inwards oriented beam under alternating gravity to achieve bistability and a piezoelectric element for energy harvesting.

CHAPTER 3

Electromagnetic energy harvesters

3.1 Introduction to electromagnetic induction

All electromagnetic energy harvesters use the principle of Faraday's law to convert kinetic energy to electrical power. That a magnetic field can generate current was hinted at by the experiments of François Arago in 1824. His experiment, showing "Arago rotation" showed a magnetized needle which rotated when a copper disc was rotated in close proximity (with the disk in parallel with the needle). The properties of electromagnetics were not well understood at the time and thus the reason for the Arago rotation was under much debate [2]. The experiments performed by Faraday in 1831 essentially provided all the laws governing electromagnetic induction [1] shedding new light on old problems. Faraday describes his experiments in "V. Experimental researches in electricity" [95], in which he writes:

> "Upon obtaining electricity from magnets by the means already described …, I hoped to make the experiment of M. Arago a new source of electricity; and did not despair, by reference to terrestrial magneto-electric induction, of being able to construct a new electrical machine"

The mathematician Clerk Maxwell derived a mathematical formulation [96] for electromagnetic induction based on Coulombs law for electrostatics and results from experiments by Faraday, as well as Lenz. This expression is known as Faraday's Law and is given by Equation (7), which states that the line integral, along a closed loop, of the electric field is equal to the time derivative of the flux in area bounded by the line. Here ϕ is the magnetic flux, E is the electric field and B is the magnetic flux density. Equation (7) is also called the induced electromotive force (EMF, with the units of Volts). Equation (8) is the differential form of Faradays law [96].

$$\oint \vec{E} \cdot \overrightarrow{ds} = -\frac{d\phi}{dt} \qquad (7)$$

$$\nabla \times E = -\frac{dB}{dt} \qquad (8)$$

To determine the current generated from moving a magnet close to a coil, the magnetic field from the magnet, in the region of the coil, must first be determined. The magnetic field from a cylindrical magnet is equivalent to the field produced by a tightly wound ideal solenoid. The field can be determined using Biot-Savarts law [97], which is an expression for the magnet

field as a result of a constant current. An alternative is to treat the magnet as a volume of infinitesimal magnetic dipoles, from which the effect of each is integrated over the volume [98]. Equation (9) gives the expression for the magnetic field density along the symmetry axis of a cylindrical magnetic. B_r is the magnetic remanence of the magnet, L_m and D_m are the length and diameter of the magnet and x is the distance from the centre of the magnet.

$$B(x) = \frac{B_r}{2}\left(\frac{x + L_m/2}{\sqrt{(x + L_m/2)^2 + (D_m/2)^2}} - \frac{x - L_m/2}{\sqrt{(x - L_m/2)^2 + (D_m/2)^2}}\right) \quad (9)$$

Equation (9) together with Equation (7) or (8) can be used to approximate the voltage induced in a coil from a magnet moving along the axis of the coil. This requires the simplification that the z-component of the magnetic field has an insignificant variation within the radius of the coil. By integrating the time differential of the magnetic field density over the length of the coil, and multiplying with area, *A*, and winding density, *n*, the generated voltage is given by Equation (10).

$$V_{IND} = nA \int \frac{dB_Z}{dt} dx \quad (10)$$

Similarly to electrical current, the magnetic flux will take the path of least resistance. In electromagnetic theory the term reluctance is used instead of resistance and is a function of the magnetic permeability, length and cross-sectional area. Materials with high permeability can be used to guide magnetic flux, constituting a magnetic circuit. The driving "force" in the magnetic circuit is called the magnetomotive force [99] and can be seen as an analogy to EMF. Magnetic circuits are for example implemented in various motors, actuators [100] and transformers.

3.2 Research in electromagnetic energy harvesting

As mentioned in the introduction of this thesis, the principles of energy harvesting by magnetic induction date back to the late 1800s. During the initial decades of development of electrical generators, size was not a large issue, nor was the frequency response as the input was typically clearly defined. The research field of vibrational energy harvesting puts the electrical generator in a new context with new challenges. Research in the field of vibrational electromagnetic energy harvesters face the same challenges as those in the field of vibrational energy harvesting in general, such as achieving a large bandwidth, high power output, low resonance frequency and small size. It is also often stated that the typical EMEH is relatively bulky but benefits from a large electromechanical coupling factor.

An important factor determining the potential power output of an EMEH is the magnetic field gradient. Some research is therefore focused on maximizing this aspect. Li et al. (2021 [101]) achieve a large gradient by a planar array of $M \times M$ magnets, with a 180° polarity shift between each row of magnets. The magnet array oscillating above a planar array of coils produces an average output power of 42 mW at 1 *g* and approximately 20 Hz. Amjadian et al. (2022 [102])

use a single coil sandwiched between two $M \times M$ planar magnets arrays. The polarization shift schemes explored by Amjadian et al. are more complex than those used by Li et al., yet the best performing array uses the same polarization scheme as Li et al. 513 mW is achieved at 0.1 *g* and approximately 61 Hz. Ordoñez et al. (2022 [103]) utilizes a stack of 3 magnetic rings, with 90° polarity shifts between each. This configuration increases the gradients of magnetic flux density within the ring-stack. Power is generated from a coil on a spring within the ring-stack. Their VEH generates 3.61 mW at 0.03 *g* and 61.7 Hz. Digregorio et al. (2024 [4]) implement an axisymmetric design and utilize the motion of a stack of ring magnets attached to a pair of planar springs to induce voltage in a pair of coils. The ring magnets are stacked with equal poles facing each other in order to increase magnetic field gradients. The VEH produces approximately 1.7 mW for an excitation of 1.32 *g* at 10Hz.

Non-linear spring action is implemented in some EMEH to increase bandwidth and/or reduce the resonance frequency. A VEH using a magnetic spring system, which is inherently non-linear, is described by Nguyen et al. (2013 [55]). An oscillating magnet is “trapped”, by opposite polarities, between two stationary magnets. Two differentially coupled coils, summing the generated voltage of each, are placed around the path of the oscillating magnet. A model, verified by measurements, shows a potential power output of 170 mW at 1.25 *g* and 16 Hz. A review on this type of VEH is given by Carneiro et al. (2020 [104]). A nonlinear magnetic torque spring is used in a wrist worn VEH described by Cai et al. (2021 [105]). Power generation of 151 µW was achieved during simulations of walking with a step frequency of 1.3 Hz.

Xu et al. (2022 [106]) achieve a bi-stable EMEH by replacing the stationary cylindric magnets, typically used in a magnetic spring system, with axially polarized ring magnets. The bandwidth of this EMEH increases with decreasing distance between the ring magnets, at a cost in peak power. The EMEH generates a peak power of 6.02 mW at 9.5 Hz and 0.5 g. Another approach to bandwidth broadening is to use multiple oscillating elements, with different resonance frequencies. A double cantilever type EMEH is described by Foong et al. (2022 [107]).

Table 3 gives a sample of vibrational energy harvesters, using magnetic induction, together with some characteristic parameters. Several design configurations are included in the table. Two of these use a planar magnet array and both achieve a significantly larger power density than most of the other examples, excluding one magnetic spring system. Of the VEH reviewed by Digregorio et al. [4], the highest performing VEH make use of planar magnet arrays. This may indicate that this design approach is an efficient means to produce large power density in an EMEH. The VEH with largest power density (Nguyen et al. [56]) in table 3 has a single permanent magnet oscillating within two coils. The magnet is levitated between two stationary magnets. The VEH by Nguyen et al. uses a heavy proof mass and a relatively large excitation acceleration. Under same conditions, the VEH with planar magnet array (Amjadian et al. [102]) would likely have better performance. The VEH described by Paul et al. [41] stands out with a large bandwidth (largest of all VEH examined in this thesis), a result of the systems non-linearity at large excitation acceleration.

Compared with the VEH in table 3, the VEH described in this thesis (paper I) does not stand out in regard to power density but achieves a moderate bandwidth by augmenting a linear mechanical spring with the force from magnetic attraction. The primary distinction of the VEH of paper I is its large resonance frequency tunability. Only two other systems in table 3 mention semi-practical tuning capability, see [56] and [106]. As the tunability is less than 1 Hz/mm in these two cases it would require rather bulky mechanics to achieve a large resonance frequency shift. The maximum tunability achieved in paper I is 420 Hz/mm, in which case the use of stacked piezoelectric actuators could be feasible. As an example, the commercially available actuator P-882.31 (PICMA), with dimensions 3 mm × 2 mm × 13.5 mm, has a travel distance of 11 μm. The P-882.31 could thus be used to shift the resonance frequency by 5 Hz, for the VEH described in paper I. Larger travel distances are commercially available but require longer stacks of piezoelectric material, or an amplifying structure.

Table 3. Summary of reviewed electromagnetic energy harvesters.

Harvester design	**Output power [μW/cm³]**	**Size [cm³]**	**BW [Hz]**	**Tip mass [g]**	**Conditions acc. @ freq.**	**Ref.**
Magnetic spring	14.3	10.6	-	13	1.3 Hz[1]	[105]
Stacked magnet rings	26.18	137.9	0.7	170	0.03 g @ 61.7 Hz	[103]
Variable reluctance	56.7	19.4	14	180	0.17 g @ 47 Hz	Paper I
Stacked magnet rings	75.9	22.4		62	1.32g @ 10 Hz	[4]
Multi-beam	199.3	600	0.8	257	0.1 g @ 25 Hz	[107]
Magnetic spring	223	27	8	15	0.5 g @ 9.5 Hz	[106]
Tapered spring	254	5.11	45	2.7	1 g @ 130 Hz	[40]
Planar magnet array	900[2]	46.8	2	38	1 g @ 20 Hz	[101]
Magnetic spring	3028	56.14	3	14	1.25 g @ 16 Hz	[55]
Planar magnet array	2729[2]	188	-	42	0.1 g @ 3.5 Hz	[102]

[1]Measured using a mechanical system to emulate walking, with a step frequency of 1.3 Hz. [2]Based on average power rather than RMS.

3.3 Electromagnetic energy harvesters for safety sensor in belt buckle

Electromagnetic energy harvesting for a safety sensor was developed within the scope of this thesis. The main goal was to reduce as much as possible or even to totally remove the electrical cables used for powering a sensor in the safety belt (Figure 16) and for transmitting the sensor's data. This was to be achieved by harvesting energy from the ambient vibrations in the belt-buckle and the mechanical work required for buckling in and out.

Figure 16. Belt buckle including cable harness and connector.

The safety belt should give information regarding the 'user status' and the 'standby status'. Thus, the energy harvesting system, acting as a power supply, should fulfil its operating requirements for these test cases:

- Airport parking – 4 weeks
- Several buckling/unbuckling events with short driving distance (e.g. taxi)
- Not so many buckle/unbuckle events (e.g. highway driving / baby chair)
- How fast after buckle/unbuckle will the system work
- Frequency of measurements – buckle/unbuckle

In this thesis we develop, test and evaluate two solutions, one to address efficient harvesting of a buckle in/out sequence and one aimed towards maximizing the harvested energy during extended periods between buckling sequences while driving. Although the solutions are evaluated separately, they can be used in unison and would then likely remove the need for cables to power the belt buckle sensor system. In the following two sections, the design and results of each solution are presented.

3.3.1 Vibrational energy harvester for belt buckle

To develop a system for harvesting the energy from vibration in a belt buckle, it is useful to know the magnitude and the frequency of these vibrations. Figure 17 and Figure 18 show two examples of accelerometer measurements performed on a belt buckle. The speed and road conditions vary between the data-sets, which is clearly reflected in the corresponding frequency plots. A VEH for these conditions will need to be able to harvest vibrations well below 100 Hz and preferably have a tunable optimal frequency down to just a few hertz as well as a significant bandwidth.

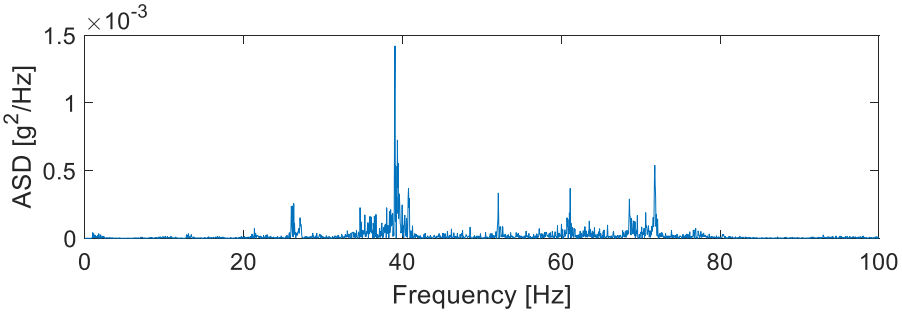

Figure 17. Acceleration spectral density of measured acceleration in a Volvo V60, driving on a highway at 70 km/h.

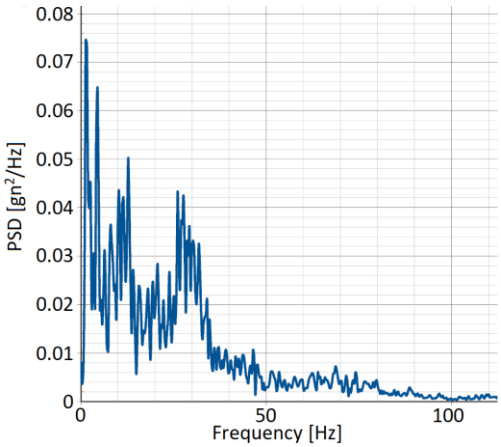

Figure 18. Power spectral density of measured acceleration in a compact Multi-Purpose Vehicle, driving on a test track at 20 km/h.

The average acceleration for the data-set corresponding to Figure 17 is only 0.38 m/s^2, which for a linear system with small mass leads to very small displacements within the VEH, unless the stiffness of the VEH is very low. One solution to this problem is to introduce a non-linearity into the system. A novel yet simple method to achieve this was to make use of the nonlinear relationship between force and magnetic flux in the air gap of a magnetic circuit. The attractive force, between the two components of the air gap, is proportional to the square of the magnetic flux in the air gap. Figure 19 shows the chosen design to implement this concept.

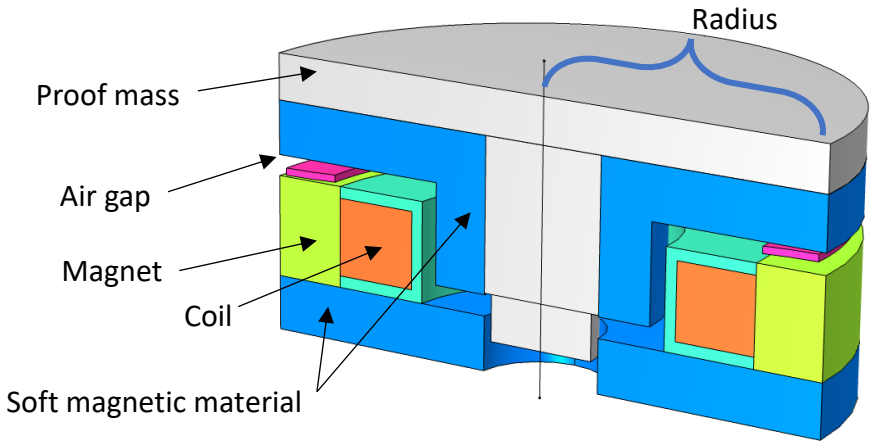

Figure 19. Electromagnetic energy harvester concept design with ideal spring placement. Schematic of geometry and constituents.

The EMEH described in paper I can be thought of as a magnetic circuit with a permanent magnet to generate magnetomotive force, a core to guide the magnetic flux and a variable air gap to control the reluctance of the magnetic circuit. The flux in the magnetic circuit is passed through a coil. Varying the reluctance of the circuit leads to a varying flux through the coil and thus an induction voltage is generated and a current if a load is connected to the coil. The variable air gap is achieved by dividing the magnetic circuit in two parts, kept apart by a mechanical spring while the magnetic flux works to close the gap. As the spring-force is linear and the attractive magnetic force is non-linear, with respect to gap length, the relationship between an externally applied force and gap length displacement becomes nonlinear.

The initial idea was based on the principles outlined in Figure 20, showing the quadratic and linear force vs distance relationship for the magnetic force and spring force respectively. At this point hysteresis effects in the magnetic core had been neglected.

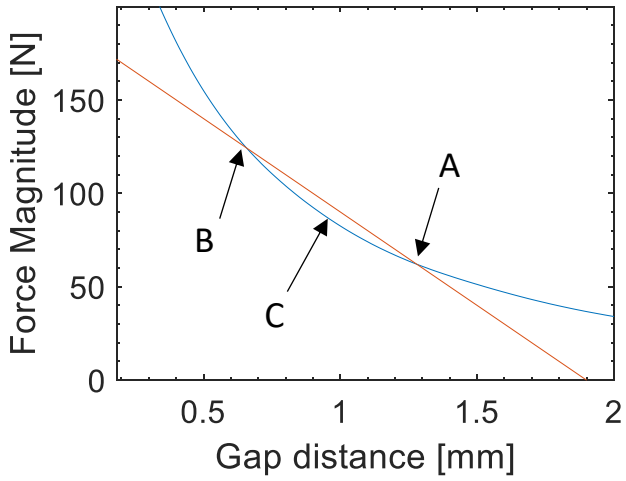

Figure 20. Magnitude of opposing forces. Blue: Magnet force. Red: Spring force. A: Stable equilibrium. B: Unstable equilibrium. C. Local maximum in restoring force.

The method to develop and validate this concept was to build both a physical prototype (see Figure 21) and an equivalent FEM model in which complex effects could be considered, such as hysteresis and eddy currents in the core. Measurement result from the prototype would confirm the validity of the FEM model, which could then be used as an optimization platform and to simulate other types of excitations. The first step in characterizing the prototype system was to measure the force at varying air gap. A custom test-rig was built to hold the relevant components (see Figure 22 right). The magnet and one core component were mounted statically. The second core component was mounted on a rod passing through the center of the magnet and resting on a vertically adjustable base. The force was measured between rod and base using a thin film sensor. The gap displacement was measured using a digital dial indicator.

The blue curve of Figure 23 shows the measured force when increasing and decreasing the gap distance. It became apparent that the magnetic hysteresis effects were not negligible when a solid iron core was used. The red curve of Figure 23 shows the corresponding simulated force curve. Although the hysteresis effect was successfully included in the FEM model, the degree of hysteresis could not be matched to reality. Hysteresis was included in

the FEM model by implementation of the 5-parameter Jiles-Atherton model [108,109]. Determining the correct parameter values is typically done by numerical methods, supported by measurements. In this thesis work the parameter space was manually explored to find suitable values to match simulations with measurements. A first guess was based on the values specified by Jiles et al. [108], valid for Fe-C 0.06 wt%. It is possible that the performed parameter search was insufficient to find suitable values. An investigation of additional or alternate sources of hysteresis was not performed and thus this possibility cannot be entirely discarded.

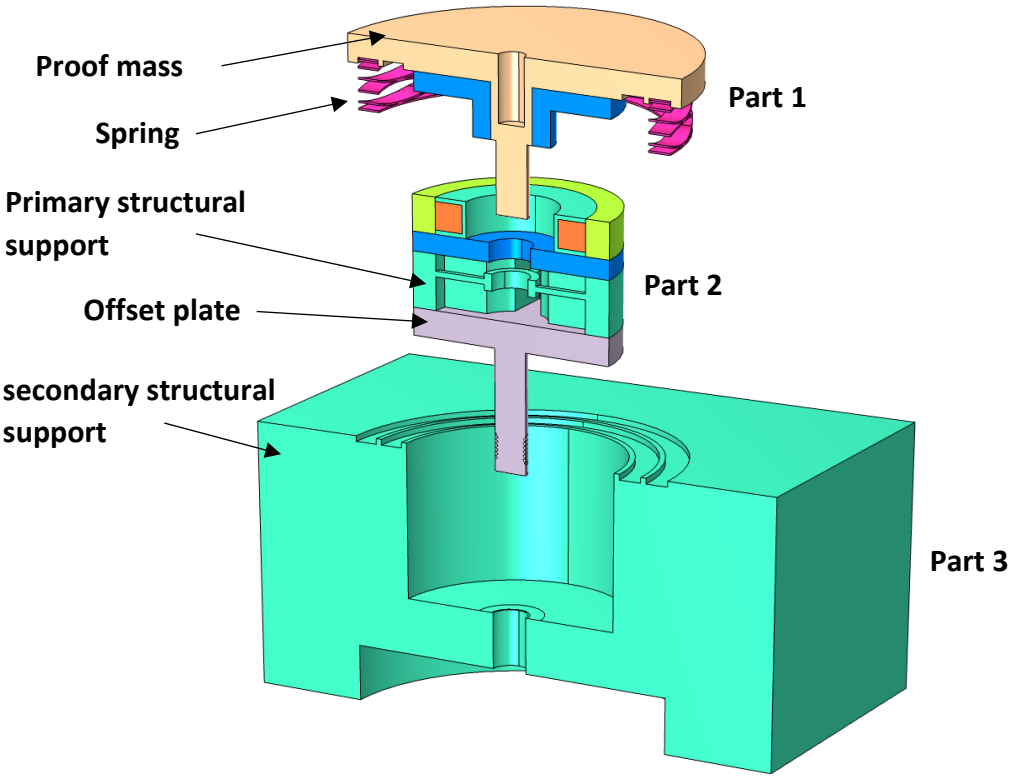

Figure 21. Exploded diagram of prototype. Top: Part 1 consisting of proof mass, spring and core component. Middle: Part 2 consisting of magnet, coil, core component, offset plate and support structure. Bottom: Part 3 is used as support structure.

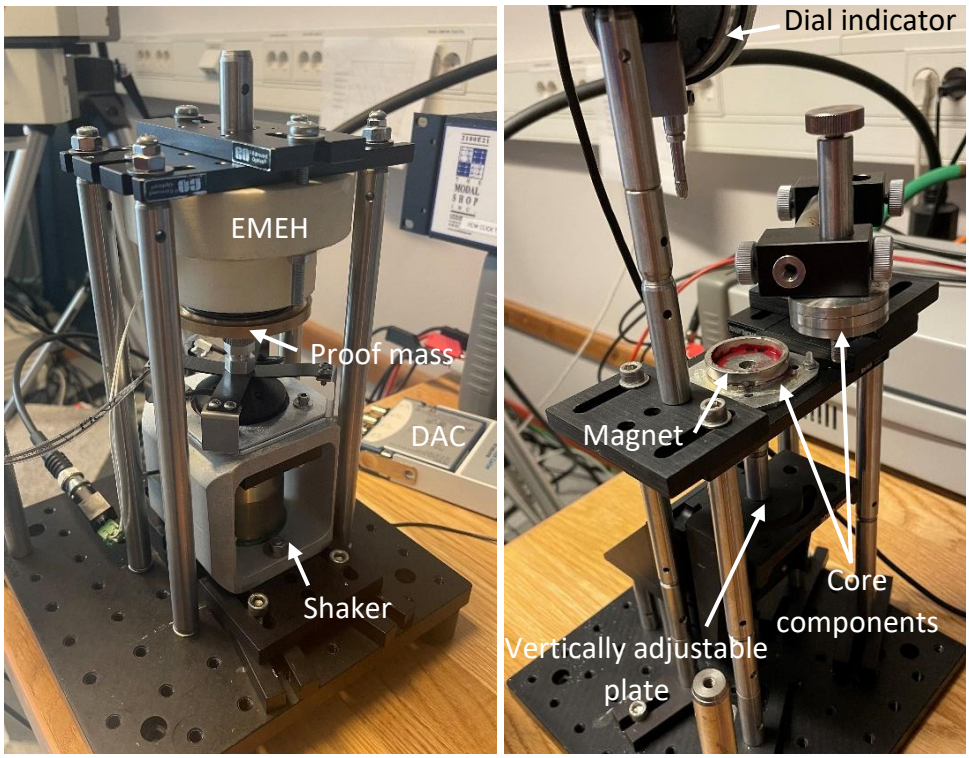

Figure 22. Left: A shaker excites the EMEH by applying a harmonically oscillating force directly on the proof mass. Right: Setup to measure force, between air gap components, at varying gap distance. Only the force due to magnetic flux in the airgap is measured, i.e. without a spring.

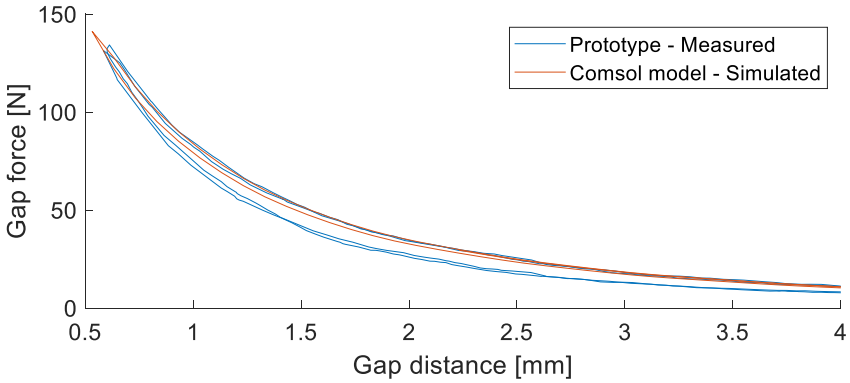

Figure 23. Force, between air gap components, resulting from magnetic flux in the air gap (i.e., spring is not included). Measured (blue) and simulated (red) force. Top part of hysteresis curve corresponds to increasing the gap distance. The air gap distance is cycled twice to confirm hysteresis effect.

Taking into account the discrepancy in hysteresis, the results of paper I were able to match the frequency dependent behavior, regarding resonance shift and peak power trend, between measurement and simulation. Material parameters described in literature, for a laminated iron core, were then applied to the FEM model, resulting in a negligible hysteresis for the system. This allowed for a tuning to significantly lower frequencies, down to 20 Hz as shown in Figure 24. Figure 25 shows the model with spring offset tuned to give a resonance at 40 Hz, using a harmonic force excitation of amplitude 70 mN (corresponding to an excitation acceleration of approximately 0.039 *g*).

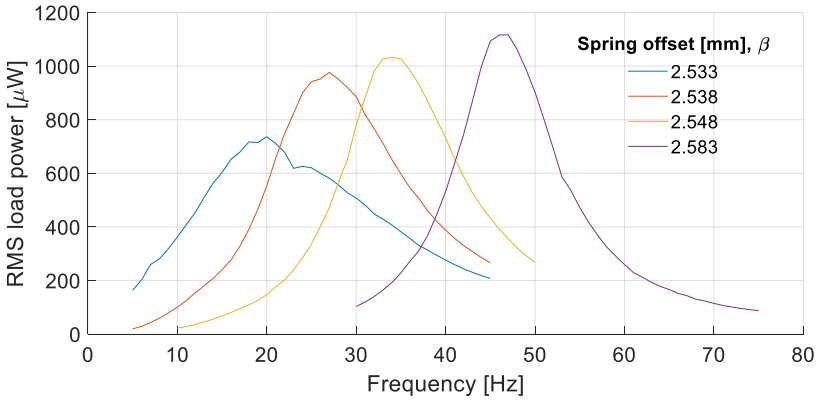

Figure 24. Simulated load power using the low hysteresis model. The excitation force is 0.3 N and load resistor of 275.1 Ω is used.

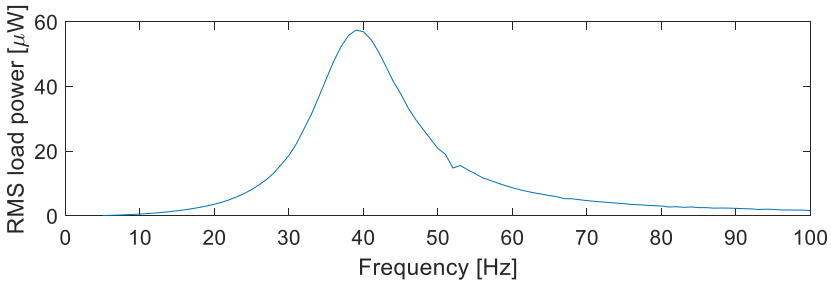

Figure 25. Frequency response using parameterization tuned to 40 Hz. The excitation force is 0.07 N (corresponding to an excitation acceleration of approx. 0.039 g) and load resistor of 275.1 Ω is used.

The final step to determine the potential performance of the VEH was then to run the FEM simulation using accelerometer data as input for excitation. The accelerometer data is shown in Figure 26 and the resulting power output from the VEH is shown in Figure 27.

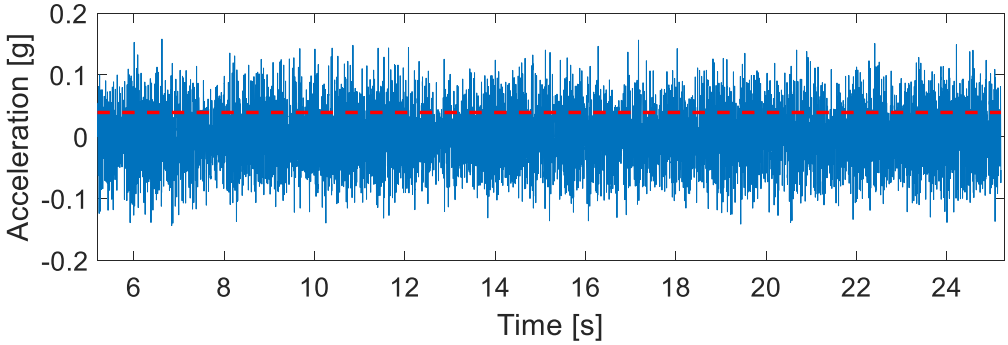

Figure 26. In situ measured vibrational acceleration data from automotive source, driving on a highway at ~70 km/h. Dotted red line shows the mean of the acceleration magnitude at 0.039 g

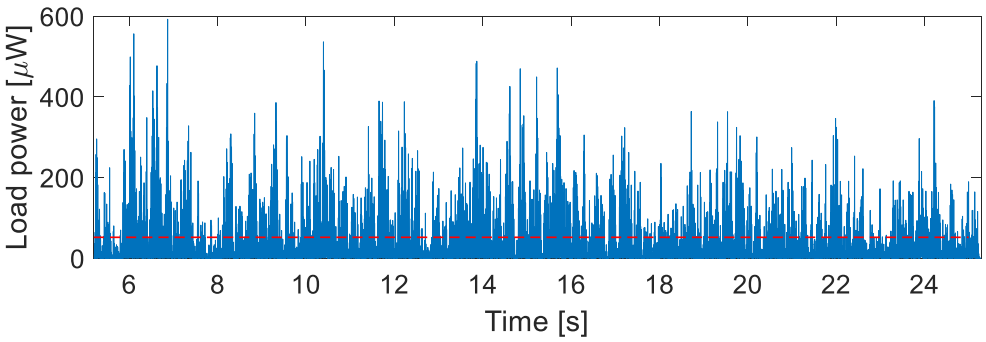

Figure 27. Simulated load power using measured vibration data as input. Dotted red line shows the mean power of 52 μW.

The EMEH concept and design for belt buckle vibration harvesting shows promising results regarding generated output power for safety sensors in modern automotive vehicles. The results show the potential to generate useful amounts of power (52 μW) when harvesting energy in-car during normal road conditions at ~70 km/h, without making use of any dynamic tuning. Although the full frequency tuning potential is not explored, it is shown that the tuning range of a single device is at least 20 Hz to 45 Hz, a useful range considering typical in-car vibrations. Considering the simplicity and robustness of the design, it could lead to a competitive alternative for use not only in an automotive application but also for other practical situations where only very small excitation signals exist such as in machinery or construction equipment.

3.3.2 Buckle in/out energy harvester for belt buckle

The belt buckle offers a second source of energy, other than the vibrations during driving. Each time a passenger, or driver, begins or ends a trip, the passenger must buckle in or buckle out. The potential bio-mechanical power available is very large compared to the vibrational energy, but only for a short time. The mechanical transient energy harvester is here mainly limited by regulations regarding the allowed maximum force required for buckle in or buckle out, which are 20 N and 18 N respectively. Measuring the force required from a standard belt buckle (see Figure 28) we can see that 11 N can be added to buckling in and 4 N to buckling out. Based on the measured distance (Figure 28), these forces represent energy sources of 165 mJ (buckle in) and 20 mJ (buckle out).

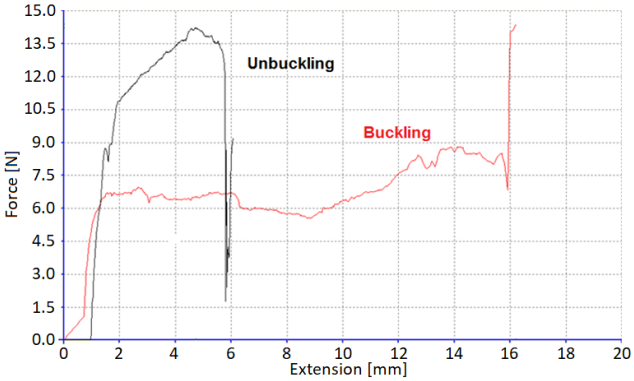

Figure 28. Measured force and displacement required to buckle and unbuckle a standard belt buckle (courtesy Autoliv AB).

To increase energy conversion efficiency and power density it is preferable to convert the above-mentioned linear movement to rotational movement. This also allows for adjusting the input force by adding a simple gear system with suitable gearing. The proposed mechanical transient energy harvester is based on a patent owned by ReVibe AB, which performs the conversion from linear to rotational movement in a simple manner (see Figure 29a). In the patented design, an external force gives angular momentum to a cylindric configuration of permanent magnets (NdFeB), which gives a rotational movement of the magnets. As the magnets rotate, their magnetic flux is diverted through an iron core to pass through a coil.

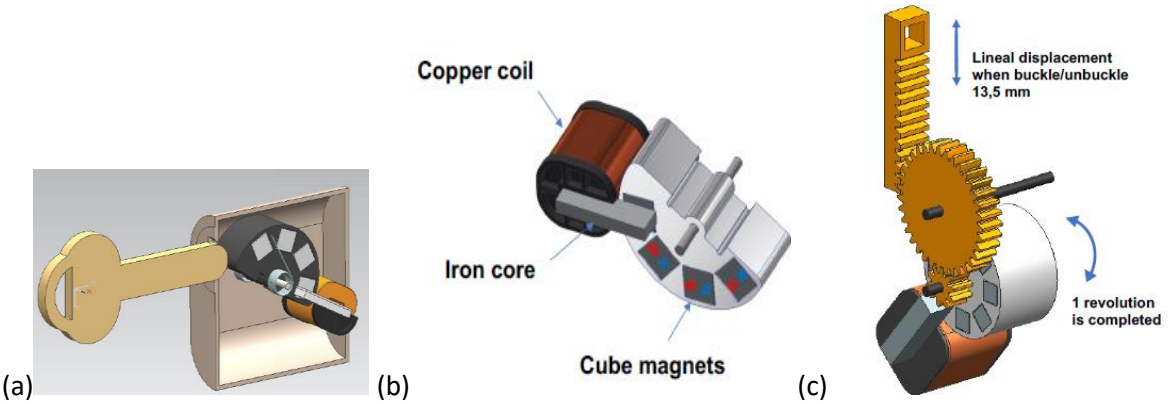

Figure 29. Schematic of energy harvester concept evaluation based on ReVibe Energy AB electromagnetic harvesting principle (a) and (b); (c) mechanical transient energy harvester based on angular movement of permanent magnets in an electric coil used inside the buckle.

Automated and manual buckle-in/-out were performed to obtain information on generated energy as a function of speed and travel distance for varying electric load. Tests were done on a similar harvester, using an equivalent mechanism as in Figure 29, but with half the rotational speed and half the number of magnets (this was intended for a different application). The generated output is 12 µJ for a constant insertion speed of 1000 mm/min (200 Ω load) and 178 µJ for manual insertion at approximately 50000 mm/min (100 Ω load), see Figure 30.

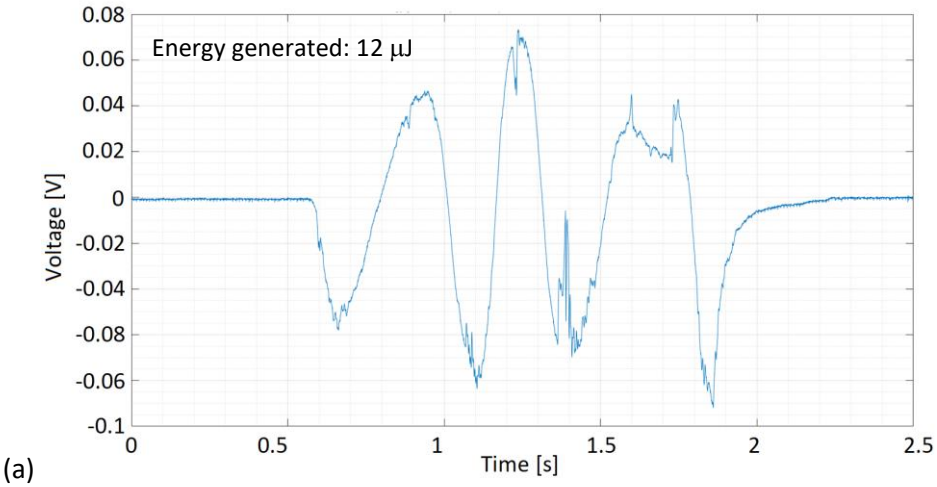

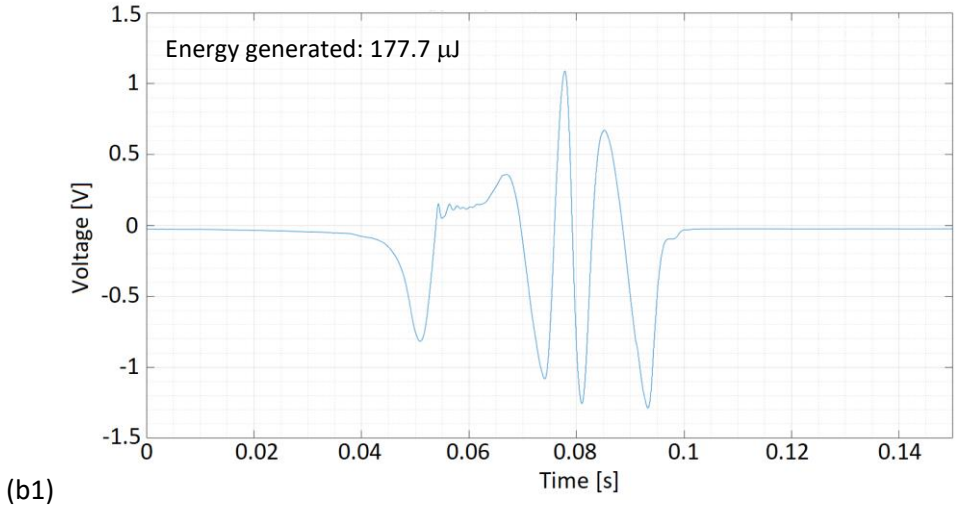

(b1)

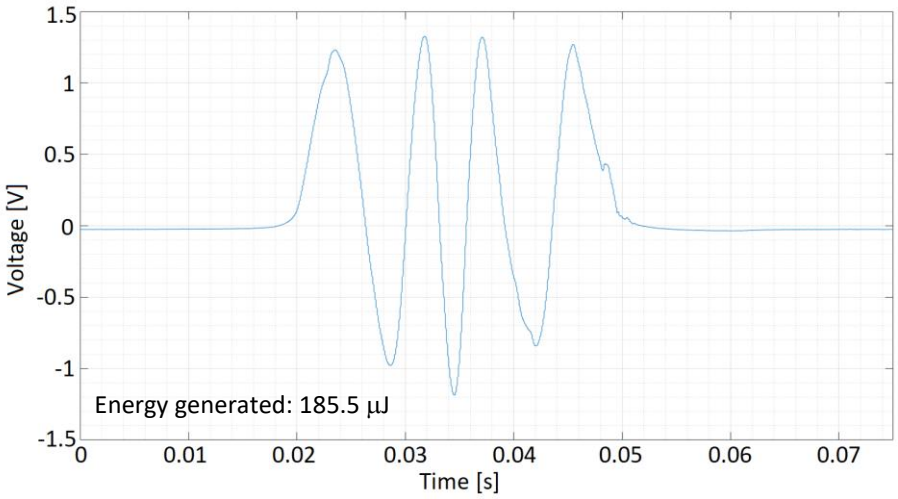

(b2)

Figure 30. Example of open-circuit voltage vs time on an equivalent mechanism (a) mechanical insertion, speed 1000 mm/min, 200 Ω load; (b) manual, load 100 Ω, (b1) insertion, (b2) extraction.

Based on these results, two buckle prototypes incorporating energy harvesting were developed:

• A standard safety buckle modified with a harvester having a 2D magnet array and using linear movement, developed by Autoliv AB (Figure 31). This design requires only minor adjustments to the original buckle housing, see Figure 32a, and has the least effect on required buckle-in/-out force.

• A 3D printed buckle incorporating multiple magnets with rotational movement (Figure 32b), developed by ReVibe Energy AB. The mechanism shown in Figure 29 is here mirrored on each side of the belt buckle. A system of two gears is used to couple linear movement to rotation. This coupling defines both rotational speed and required buckle-in/-out force.

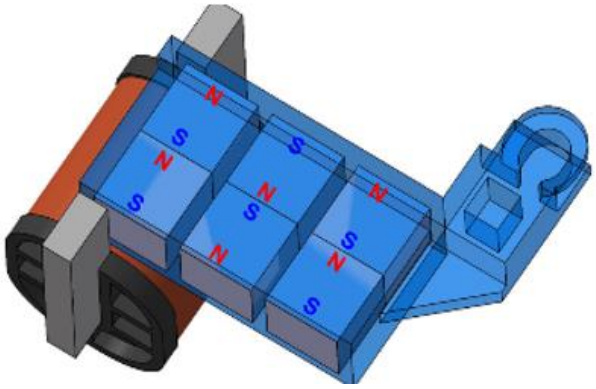

Figure 31. Schematic mechanical transient energy harvester based on linear movement of permanent magnets in an electric coil used inside the buckle.

(a)

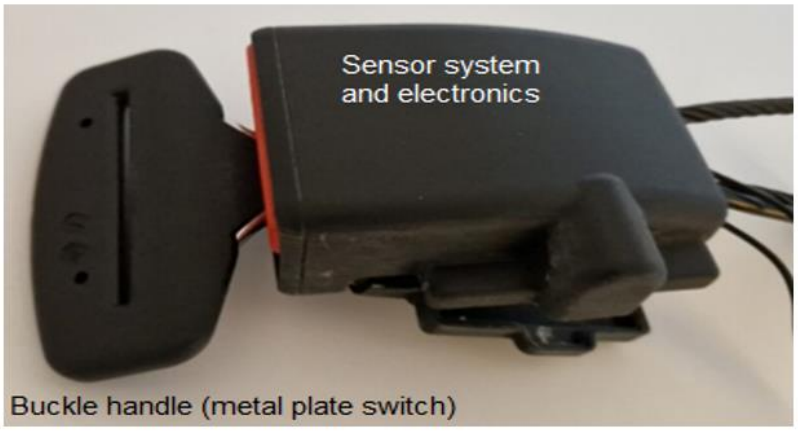

(b)

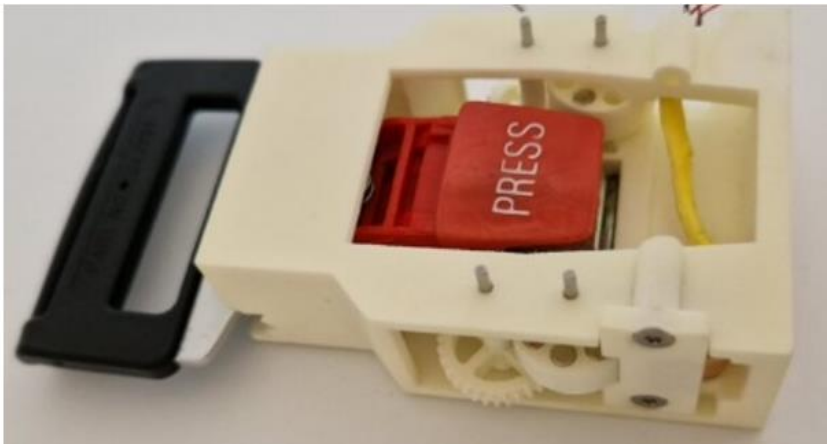

Figure 32. Image of safety buckle developed by (a) Autoliv AB and (b) ReVibe Energy AB that include energy harvester.

The Autoliv developed buckle with incorporated mechanical-electromagnetic harvester (Figure 32) was tested for various configurations and parameters for the coil and resistive load. The results from manual buckle-in/-out, based on one configuration, are shown in Figure 33. The maximum measured energy output was approximately 300 µJ for buckle-in and 400 µJ for buckle-out.

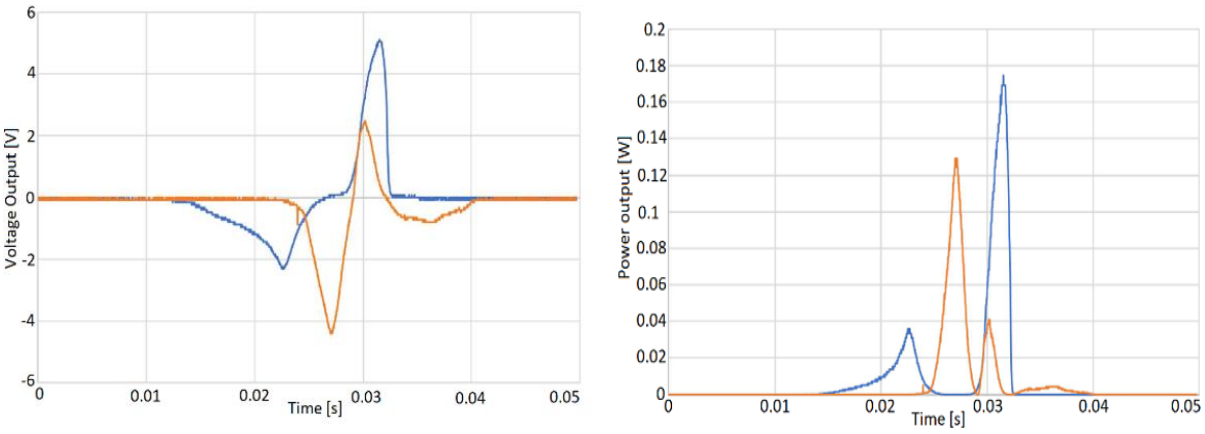

Figure 33. Example of Autoliv harvester's open-circuit voltage and power for wire diameter: 0,1 mm, 3000 turns, R = 150 Ω, load R = 350 Ω. Blue curve corresponds to buckle-out event and orange curve corresponds to buckle-in event.

Peak power as function of resistive load was also measured for impedance matching optimization and is shown in Figure 34. The blue and red data points are the power outputs averaged over 5 buckle-in/-out events. The grey data points are measured on a commercial mechanical switch energy harvester (BLE-SWITCH001-GEVB), added for comparison. The optimal loads are 100 Ω and 300 Ω for ReVibe's and Autolivs's energy harvesters respectively.

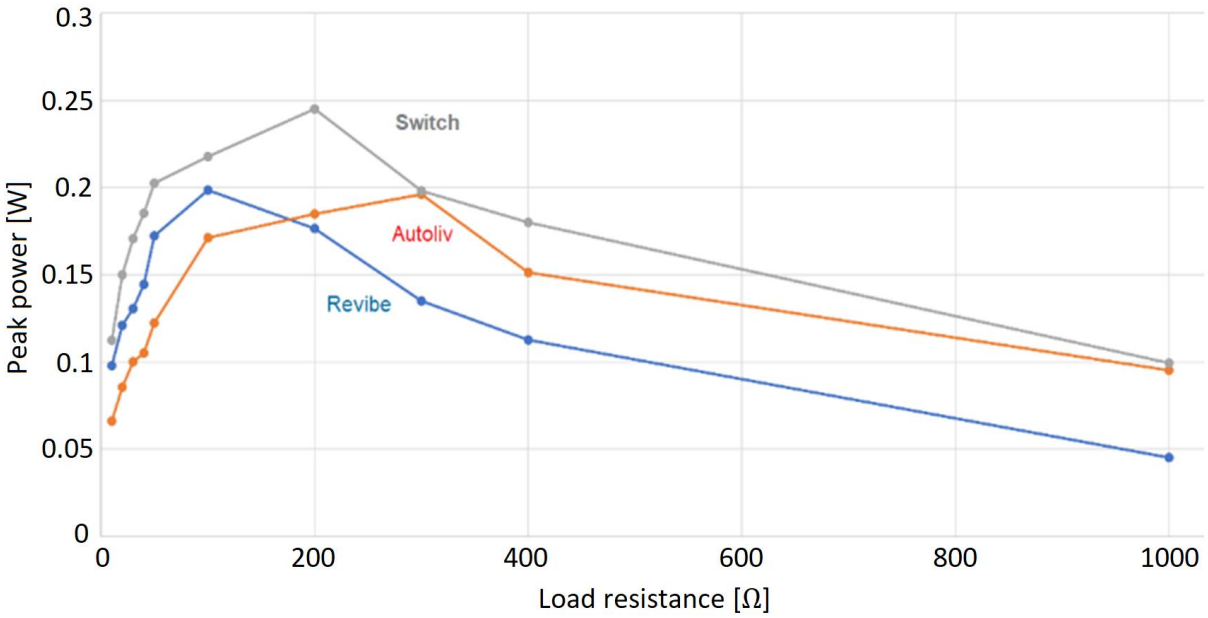

Figure 34. Peak power harvested as function of resistive load.

The time required to manually perform a buckle-in/-out event was estimated by manually performing the procedures 10 times each while measuring with a laser control system. The average time for both buckle-in and -out was about 0.1 s. The displacement history is shown in Figure 35.

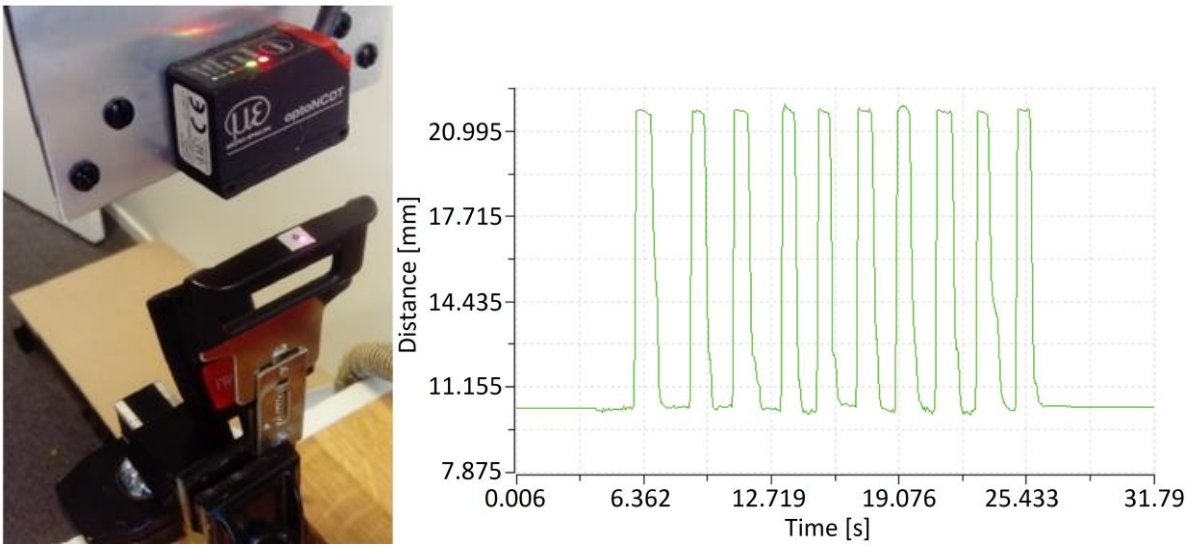

Figure 35. Image for setup to estimate the buckle-in/-out time (left) and results (right).

Application tests were also performed for both protypes, Autoliv and ReVibe (Figure 32) connected to commercial wireless communication units to check their performance. By buckle-in or -out from at least one meter, it was possible to activate a RF Receiver and Transmitter Module (Qiachip 433MHz).

The Bluetooth® low energy switch evaluation board (BLE-SWITCH001-GEVB) was used to measure the voltage transients and as comparison with a commercial mechanical switch energy harvester, also utilizing electromagnetic induction. The open-circuit voltage was measured for the commercial switch, and both buckle harvester prototypes (for which the commercial switch was removed from the BLE circuit), see Figure 36. The results for the Autoliv EH are comparable with Figure 33. Compared to Figure 30, ReVibe's EH naturally has substantially larger voltage as the design is here tailored to the application. The overall shape is still comparable.

All these graphs have the same time interval in which by one buckle-in/-out, Autoliv buckle gives only one pulse while ReVibe's buckle gives multiple pulses, due to differences in magnet arrays. Also, the open-circuit voltage shape is wider for both buckle prototypes compared to the commercial switch energy harvester, which means that more energy can be harvested. The duration of energy harvesting for both buckle designs is small (10 ms – 20 ms) compared to the measured average buckle-in/-out time. This may indicate that only a portion of the available mechanical energy is utilized for energy harvesting and that design optimization may lead to significant improvements.

During all these measurements, voltage data was sent via BLE to a PC at a few meters distance.

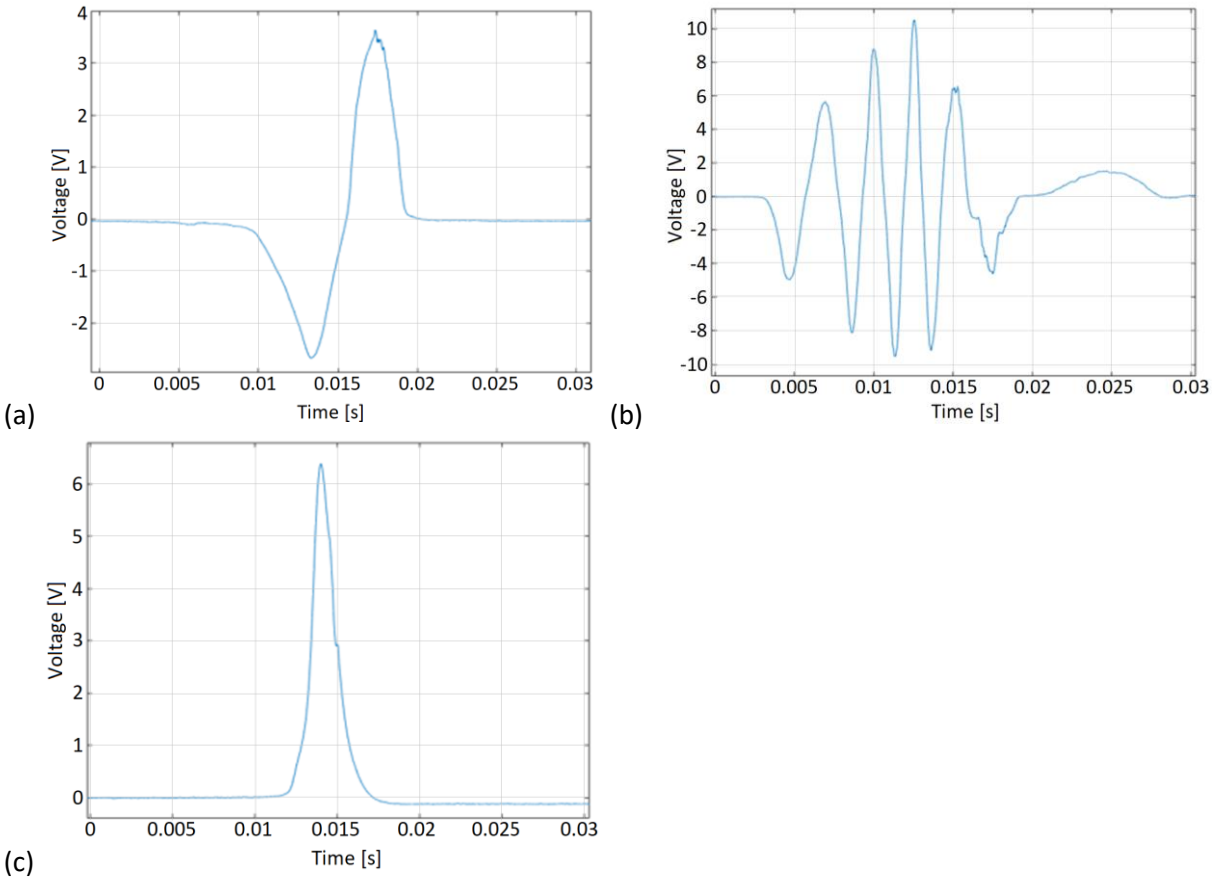

Figure 36. Typical open-circuit voltage from the (a) Autoliv harvester-buckle prototype; (b) ReVibe harvester-buckle prototype; (c) mechanical switch by using Bluetooth® low energy switch evaluation board (BLE-SWITCH001-GEVB).

In summary, this design allows for an easy, robust, and elegant solution to harvest energy for a safety belt. The linear displacement obtained from the buckle is transformed to angular displacement. One revolution is completed by the magnet holder with the insertion or extraction of the buckle. This mechanism can be implemented in a compact design, with reasonable dimensions as compared to the original belt buckle.

Simulations demonstrate that with all the space and design limitations it is still possible to generate enough energy with the presented concept. Dual energy harvester generators would potentially produce up to 8 mJ in 0.1 seconds.

Measurement results of ReVibe's linear to angular energy harvester show better performance than the compared commercial unit. The measured peak output voltage of 10 V is promising, but the relatively short signal duration indicates room for significant improvement in energy harvesting.

To give an estimate on the practical performance of this energy harvester, we assume a simple rectifier bridge is used, with low voltage drop diodes (approx. 0.25V each), and a commercial lower power harvester power management IC with high rated input voltage (>10 V) and 90% efficiency (ADP5310). Assuming an additional 10% energy is dissipated within the harvester

itself, then at least 70% of transduced power can be used to generate a stable voltage for a sensor. Considering a buckle sensor consumes in μW range, the buckle sensor could work continuously for up to 10 min, for a single buckle event.

3.4 Enhancing electromagnetic energy harvesting using magnetostriction

The energy harvester described in section 3.3.1 showed good performance regarding frequency response and power density relative the excitation amplitude. As a continuation of this work, we explored the possibility of synergistically combining the principles of the aforementioned VEH with giant magnetostriction. The reasoning behind this approach is that the concept of a variable air gap, with displacement determined by an attractive magnetic force and a restoring mechanical spring force, inherently provides the potential of pre-stress and magnetic field bias, which we will see from the next section, are key factors for optimal magnetostrictive effect.

3.4.1 Introduction to magnetostriction and magnetoelasticity

Magnetostriction is the occurrence of an additional strain in a material resulting from an applied magnetic field, also called the Joule effect. James Joule first measured this effect in 1842, who upon a request from F. D. Arstall, measured an elongation of 85 um in a 610×6×3 mm^3 iron bar when subjected to a magnetic field [110] (the field strength is not specified in the reference). Magnetoelasticity describes the change in magnetization resulting from an applied strain, also called the Villari effect after its discovery by Emilio Villari ([111] is commonly cited). In the decades following the measurements by Joules and Villari, it seems no significant research was performed specifically regarding magnetostriction or magnetoelasticity. In 1888 researched on the subject began to grow as H. Nagaoka published his first paper on magnetostriction and continued to pioneer the field, later joined by K. Honda [112]. Based on the extensive review article by Kumar et al. [113], a body of research regarding the modelling of magnetostriction began to grow from around 1930, including both anhysteretic and hysteretic models.

In the context of magnetostriction, the theory of the magnetic domains provides an important piece of the puzzle. The theory, formulated by P. Weiss in 1906 [114], describes the distribution of the orientation of atomic magnetic moment in ferromagnetic materials. According to Weiss, ferromagnetic materials can be divided into microscopic domains. Within one such domain the magnetic moments of all atoms are aligned in the same direction, producing a net magnetic moment. If an external magnetic field is applied, the magnetic moments of a domain will rotate to align with this external field. This rotation of atomic magnetic moments leads to the magnetic domain expanding in the direction of applied field [112,115]. The sum of all domain rotations produces strain in the material, which is the effect dubbed magnetostriction. All ferromagnetic materials act in this way, although most to a very small degree; the magnetostrictive strain in iron is in the order of 10^{-5} [116]. There are also materials which exhibit very large magnetostrictive strain, also known as giant magnetostriction. Examples of this are galfenol and terfenol-D, with magnetostrictive strain in the order of 10^{-4} to 10^{-3} [117]. Magnetostriction and magnetoelasticity can also be

implemented in a non-metallic material, by e.g. introducing ferromagnetic particles into a polymer [118].

The magnetostrictive and magnetoelastic effects of galfenol are quantitatively shown in Figure 37, as measured by Flatau et al. [119]. The magnetostrictive strain levels off at large applied magnetic field (see Figure 37 left). This effect corresponds to magnetic saturation, i.e. the magnetization direction in each magnetic domain cannot rotate further and the magnetization of the sample is at its saturation. The corresponding strain is called saturation magnetostriction, λ_S. Figure 37 also shows that there is a magnetic field bias and a pre-stress which maximize the magnetostrictive and magnetoelastic effects. From Figure 37 (left) this is clearly seen that there is certain magnetic field which gives the largest slope in strain. In Figure 37 (right) it is not as evident, but the stress vs magnetic induction curve also has a point of maximum slope (see stress vs magnetic induction curves in [119]).

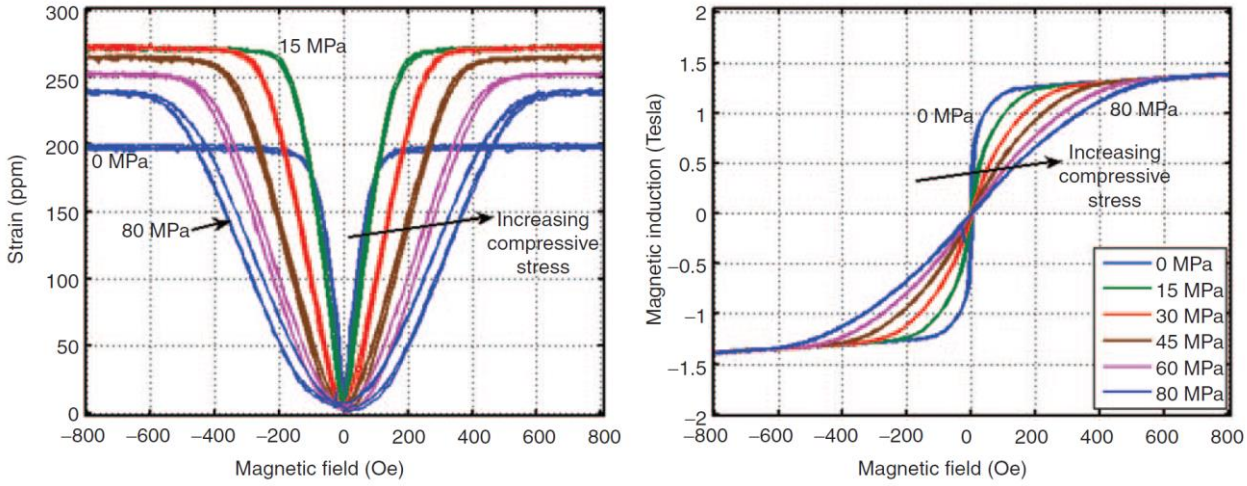

Figure 37. Measurements on single-crystal $Fe_{71}Ga_{29}$, furnace cooled, 〈100〉. (a) Magnetostrictive strain vs applied magnetic field for various pre-stress. (b) Magnetic induction vs applied magnetic field for various pre-stress. Reprinted with permission from [119]. Copyright 2008, SAGE Publications.

Assuming small variations in strain or magnetization, the magnetostrictive and magnetoelastic effects can be modelled using linear constitutive equations. The total strain, $\boldsymbol{\varepsilon}$, is given by combining Hooke's law and the magnetoelastic effect, see Equation (11). Further, the induced magnetic field density, $\boldsymbol{B}$, is given by combining the magnetic constitutive law and the magnetostrictive effect, see Equation (12). $\boldsymbol{s}$ is the compliance tensor (4th rank) [120] at constant magnetic field strength and $\boldsymbol{\mu}$ is the magnetic permeability at constant stress. Matrices $\boldsymbol{T}$ and $\boldsymbol{H}$ describe stress and magnetic field, respectively. $\boldsymbol{d}$ is a tensor (3rd rank) of piezomagnetic coefficients which, for a specific measuring orientation, corresponds to the gradient of the curve in Figure 37 (left) at a certain value of stress and magnetic field. The coupling between mechanical and magnetic domains is here assumed to be equal in both directions, else different piezomagnetic coefficients should be used in Equations (11) and (12). The magnetostrictive and magnetoelastic components of Equations (11) and (12) are defined in Equations (13) and (14). Equations (11) to (14) use Voight notations (see section 2.1).

$$\varepsilon_j = s_{jl}T_l + d_{ji}H_i \qquad (11)$$

$$B_i = d_{ij}T_j + \mu_{ik}H_k \qquad (12)$$

$$\boldsymbol{\varepsilon}_{me} = d_{ji}H_i \qquad (13)$$

$$\boldsymbol{H}_{me} = d_{ij}T_j/\chi\mu_0 \qquad (14)$$

In this work, a non-linear model is used in simulations of magnetostriction. The magnetization and magnetic induction are then expressed by the non-linear functions described by Equations (15) and (16).

$$\boldsymbol{M} = M_S L\left(\left|\boldsymbol{H}_{Eff}\right|\right)\frac{\boldsymbol{H}_{Eff}}{|\boldsymbol{H}_{Eff}|} \qquad (15)$$

$$\boldsymbol{B} = \mu_0\left(\boldsymbol{H} + \boldsymbol{M}(\boldsymbol{H}_{Eff})\right) \qquad (16)$$

Here L is a function defining the magnetization shape and $\boldsymbol{H}_{Eff}$ is the sum of the externally applied magnetic field, $\boldsymbol{H}$, and the field resulting from mechanical stress, $\boldsymbol{H}_{me}$. One possible choice of L is the Langevin function, in which case $L\left(\left|\boldsymbol{H}_{Eff}\right|\right)$ is given by Equation (17).

$$L\left(\left|\boldsymbol{H}_{Eff}\right|\right) = \coth\left(\frac{3\chi_0|\boldsymbol{H}_{Eff}|}{M_S}\right) - \frac{M_S}{3\chi_0|\boldsymbol{H}_{Eff}|} \qquad (17)$$

Here χ_0 is the initial magnetic susceptibility, i.e. the susceptibility as $\boldsymbol{H}$ approaches zero. From the theory of micro-magnetics and by using the principle of energy minimization [121], the isotropic magnetoelastic strain can be described by Equation (18) [120]. Here $\boldsymbol{m}$ is a unit vector (normalized magnetization) described by, $\boldsymbol{m} = \boldsymbol{M}/|M_S|$, $\boldsymbol{I}$ is the unity matrix and $\boldsymbol{m} \otimes \boldsymbol{m}$ is the tensor product.

$$\boldsymbol{\varepsilon}_{me} = \frac{3\lambda_S}{2}(\boldsymbol{m} \otimes \boldsymbol{m} - (1/3)\boldsymbol{I}) \qquad (18)$$

Noting that the magnetostrictive piezomagnetic coefficient is given by $\frac{\partial \boldsymbol{\varepsilon}_{me}}{\partial \boldsymbol{H}}$ [120,122,123] and that $\frac{\partial \boldsymbol{M}}{\partial \boldsymbol{H}} = \chi$, where χ is the magnetic susceptibility for arbitrary $\boldsymbol{H}$, the magnetostrictive effect is derived from Equation (14), resulting in Equation (19).

$$\boldsymbol{H}_{me} = \frac{1}{\mu_0\chi}\boldsymbol{T}\frac{\partial \boldsymbol{\varepsilon}_{me}}{\partial \boldsymbol{M}}\frac{\partial \boldsymbol{M}}{\partial \boldsymbol{H}} = \frac{3\lambda_S}{\mu_0 M_S^2}\boldsymbol{T}\boldsymbol{M} \qquad (19)$$

3.4.2 Magnetostrictive energy harvester research

In the 1960s it was discovered that certain rare earth garnets had drastically larger magnetostriction than hade be previously measured (Terbium and Dysprosium, among others, were examined [124,125]). Although these materials exhibited large magnetostriction, their practical use was limited due to low Curie temperature (218 K for Tb and 85 K for Dy [126,127]). Motivated by the potential for giant magnetostrictive materials to boost performance of underwater sonars, the U.S. Navy funded extensive research in the subject [128]. In 1972, Clark et al. published a paper describing the room temperature giant magnetostriction in $TbFe_2$ (discovered in 1971 [115]) and $DyFe_2$ [129]), the former later being dubbed terfenol-D (in which dysprosium is beneficially added). Due to the high sensitivity to

temperature, and its brittle nature, an alternative to terfenol-D was sought, which led to the discovery of galfenol ($Fe_{100-x}Ga_x$). Galfenol has the benefit of being ductile and heat resistant (also having a large Curie temperature of 943 K), among other things [117,130]. A detailed experimental characterization of galfenol was performed by Dapino et al. [131] (see also the report [132]).

Although galfenol was used in several different sensing and actuation applications (Sonar, electric motors, torque or displacement sensor, magnetometers, et c. [133,134]), since its discovery in 1999, it seems it was not until 2005 that the (possibly) first example of galfenol use in vibrational energy harvesting, by Flateu et al. [130] (although other giant magnetostrictive material have been evaluate for energy harvesting prior to this). In [130], Flateu et al. examined the possibility to use galfenol to extract energy from low frequency (below 100 Hz) vibration, having ship hull vibrations in mind. Research in the field of magnetostrictive energy harvesting has continued, with publications on both magnetostrictive cantilever beam VEH [135–137] and magnetostrictive rod type VEH [117,138]. The review by Deng et al. [139] gives an overview of VEH using different magnetostrictive materials in both rod and beam configurations. Narita et al. [45] provide a review include other transduction types, providing an interesting comparison.

Ducharne et al. have in their research [140,141] evaluated and compared energy harvesting using various magnetostrictive materials. Their conclusion is that, given sufficient magnetic biasing, terfenol-D and galfenol give the best performance.

From 2019 to 2022, Rasilo et al. published several papers dealing with the modelling of galfenol rod [142–146] and galfenol cantilever beam energy harvesting [147]. Thermodynamic constitutive laws and an equivalent stress model are implemented within the FEM simulation tool COMSOL, and a linearized small signal model is developed and evaluated. The simulation results are shown to correspond well with measurements.

Similarly, Davino et al. have published several papers describing and modelling magnetostrictive energy harvester. Davino et al. primarily take an equivalent circuit approach to developing a (non-linear) model for the VEH voltage and power output. In [148], such a model is implemented in COMSOL. Following the equivalent circuit approach, Davino et al. have explored circuit designs with active control to maximize the converted voltage and power (i.e. the rectified and voltage converted signal) [149–151]. Davino also gives an example of utilizing magnetostriction for energy harvesting in a vehicle suspension system [152].

From the sample of magnetostrictive beam energy harvesters given in table 4, most have comparable power densities (especially considering the differences in excitation acceleration amplitudes). The VEH described by T. Ueno [153] stands out with a large power density and bandwidth at moderate excitation acceleration and low tip mass. In the design by T. Ueno the galfenol beam is positioned some distance away from the neutral axis leading to an amplification of stress, as well as a more homogenous stress distribution. The downside of this being a stiffer structure. T. Ueno also uses a relatively small magnet and galfenol beam, while maintaining a seemingly good magnetostrictive effect. Similarly to paper IV, both variable reluctance and magnetoelasticity contribute to the time varying magnetic field within the coil.

Coupling between variable reluctance and magnetostriction is however not discussed in the paper by T. Ueno. An important distinction in the VEH by T. Ueno is that the magnetostrictive element is soldered rather than adhered with epoxy (as is in the other examples of table 4). Based on the data in table 4 the VEH described in paper IV has competitive power density and bandwidth in its size range (~10^1 cm^3). Of the examined literature, the system in paper IV is also the only magnetostrictive cantilever beam VEH which implements both pre-stress and magnetic field bias. A second important distinction is the potential of resonance frequency tuning. None of the examples given in table 4, other than paper IV, provide practical means of frequency tuning. The results of paper IV showed a tunability of 140 Hz/mm. As mentioned in section 3.2, at this scale of tunability, the use of piezoelectric actuators is feasible. As a reference, the commercially available amplified piezoelectric actuator APA150XXS (Cedrat Technologies), of dimensions 5 mm x 14 mm x 9 mm, has a travel distance of 130 um, which could be used to shift the resonance frequency by 18.5 Hz.

Table 4. Summary of reviewed magnetostrictive beam energy harvesters.

Harvester type	**Output power [µW/cm³]**	**Size [cm³]**	**BW [Hz]**	**Tip mass [g]**	**Conditions acc. @ freq.**	**Ref.**
Rectangular Cantilever	26.28	15.6	1.5	3.7	0.3 g @ 139.5 Hz	[154]
Rectangular Cantilever	30	4.62	10	2	0.5 g @ 45 Hz	[155]
Rectangular Cantilever	64.1	15.6	8	3.6	1 g @ 200 Hz	[135]
Rectangular Cantilever	69.7	22.9	-	-	1 g @ 222 Hz	[156]
Rectangular Cantilever	95.9	22.9	-	10	1 g @ 222 Hz	[157]
Variable reluctance	275	18.5	7	10	0.5 g @ 216 Hz	Paper IV
Variable reluctance	1186	3.12	-	4.8	2.5 g @ 166hz	[158]
Variable reluctance	3000	0.4	12[1]	1.6	1.2 g @ 212 Hz	[153]

[1]Bandwidth value is based on the relation between resonance frequency and Q-factor.

3.4.3 Magnetostrictive cantilever beam energy harvester for belt buckle

To explore the possibility of synergistically combining magnetostriction with the previously described concept using a variable airgap (see section 3.3.1), a cantilever approach was implemented. This resulted in a rectangular planar-symmetric design, with a magnetostrictive beam as elastic component, instead of a wave spring as previously used. This design simplifies the implementation of a magnetostrictive material, as a layer can be adhered to a substrate beam (green segment in Figure 38a). Two designs have been evaluated in this work, the second a necessary iteration of the first due to poor magnetic field biasing conditions (a conclusion drawn from measurements and simulations, as will be described). In both designs the magnetic circuit consists of a skewed “U” shaped core (grey). Either one or two magnets (blue/red) provide the magnetomotive force. The magnets are attached at the ends of the beam, with one also taking the role of proof mass. In the original design, a simple bilayer beam is used, with a substrate layer (green segment in Figure 38a) and a magnetostrictive layer (purple segment in Figure 38a), of equal thickness. In the iterated design the magnetostrictive layer is made significantly shorter and slightly thicker, with a layer of soft magnetic material on top (light blue segment in Figure 38b). The magnet fixing the beam to the core is also replaced by a corresponding block of iron. The changes made for the iterated design have the primary purpose of reducing magnetic field bias in the magnetostrictive layer.

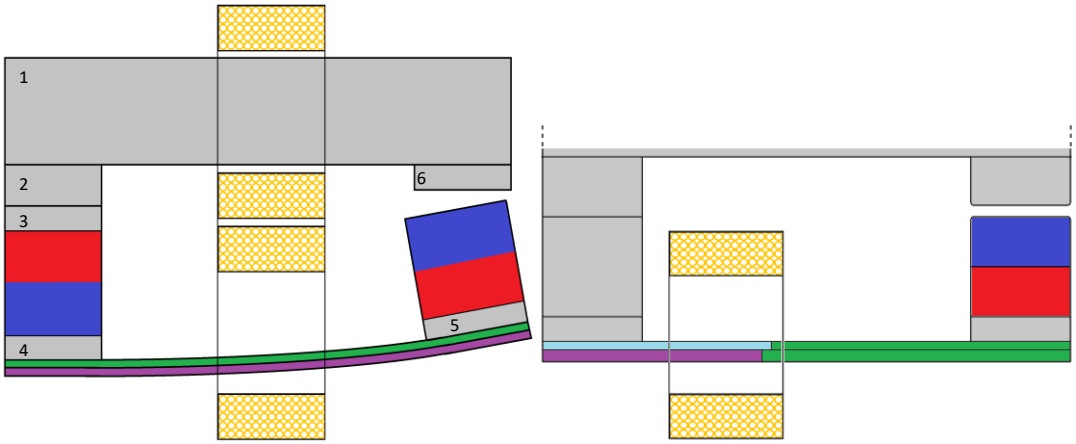

Figure 38. (a) Cross section of the original energy harvester design, with iron core (grey), neodymium magnets (blue/red), aluminum substrate (green) and galfenol magnetostrictive layer (purple). (b) Cross-section of iterated design.

In equilibrium, the beam tip is displaced due to the force resulting from the magnetic flux in the air gap. In this way the magnetostrictive layer of the beam experiences both a pre-stress and magnetic field bias. The oscillations of the systems are coupled to the distance of the air gap through the movement of the proof-mass magnet. The resulting variation in airgap reluctance (due to the change in air-gap distance) leads to magnetic flux variations in the magnetic circuit which can be used to induce current in a coil. Two coils are included in Figure 38a to note that we examine the magnetic induction in both paths.

The goal is to achieve a large coupling between the magnetic flux variations of the magnetic circuit, displacement of the proof mass and the magnetostrictive/magnetoelastic effects. By placing a material of positive λ_S on the bottom side of the beam, the magnetostriction would contribute to the displacement of the beam tip, and increasingly so as the magnetic flux increases while the airgap distance decreases. Likewise, the increase in beam stress as the airgap decreases would lead to increased magnetization of the magnetostrictive component. The potential of increased non-linear behavior and the benefits thereof are also of interest.

Following the method of the paper I, a COMSOL model and corresponding lab-prototype were built (see Figure 39). The purpose is here for the lab-prototype to verify the COMSOL model, allowing for further evaluation through simulation. Only the original design has a corresponding lab-prototype. The details regarding the material and simulation parameters are given in paper IV.

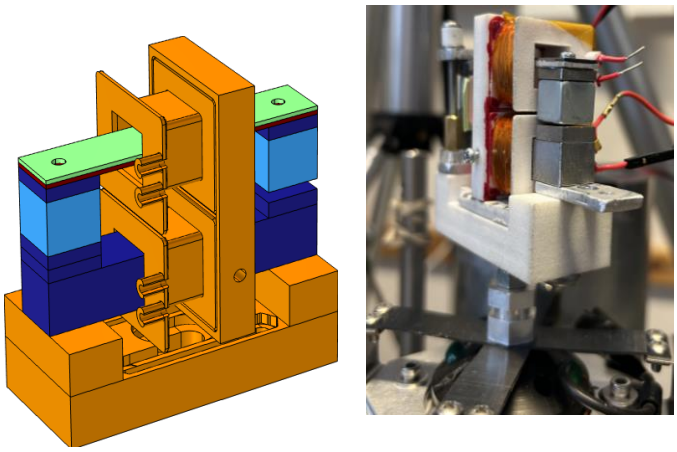

(**a**) (**b**)

Figure 39. 3D CAD of COMSOL model geometry, with iron (dark blue), neodymium (light blue), aluminum (dark red), galfenol (green) and polyamide (orange). (b) Prototype for lab measurements. The energy harvester is here mounted on top of the shaker.

For the prototype we chose to use galfenol (produced by Extrema, which uses the composition $Fe_{81.6}Ga_{18.4}$). The main reason being its large saturation magnetostriction constant (λ_S = 200 ppm) combined with its ductile nature and thus ease of machining. The delivered galfenol rod was cut in-house using wire electrical discharge machining. The core parts were manufactured using the same process. To allow for some modularity, the design of the lab-prototype includes several threaded holes for screwing parts together. Iron blocks with threaded holes were glued to the magnets. The beam layers are also glued together. The beam and core are then screwed to the magnets, completing the system.

The use of glue in this case proved challenging. Initially epoxy glue was used. Glued surfaces were left to dry overnight while firmly pressed together by a clamp. This resulted in very small glue gaps but also seemed to reduce the bond strength as the surfaces easily lost adhesion while handling. A rudimentary structure was added to support the beams mechanical attachment to the core. The in-house manufactured galfenol beam was glued to the beam substrate also using clamps. Inconsistencies in the initial measurements indicated issues with the glue layer (possibly due to partial loss of adhesion). As mentioned in paper IV, mechanical damping can vary significantly with glue layer thickness, and it is likely that the natural frequency of the beam decreases with increasing glue layer thickness. These issues were resolved by using liquid metal as glue instead of epoxy.

The hypothesis is that the magnetostrictive component will enhance power density. In order to determine if this is true, a comparison must be made with an equivalent system which does not have a magnetostrictive component. For the simulation model, a reference is generated by running the simulation with magnetostriction deactivated (by setting $\lambda_S = 0$). For the lab-prototype we used a second beam, with galfenol replaced by iron, as a reference. The two systems, using either a galfenol beam or Iron beam, are not directly comparable and thus this reference is mainly qualitative. The comparatively large relative permeability and mechanical stiffness of iron will lead to differences in behavior.

The data acquisition procedures, from simulations and lab-measurements, are described in paper IV. The primary output from each is their respective frequency response of the open circuit voltage (OCV) from a theoretical coil (the amplitude is the RMS of a time dependent data set). The measured voltage can be defined as open circuit, as the output impedance is less than 500 Ω and the input impedance (to the measuring unit) is larger than 1 MΩ. We also simulated the systems under free oscillations, from which we could determine both the natural frequency and damping. We found the simulated resonance frequencies and damping ratios to be 227 Hz and 8.1 $\times 10^{-3}$, for the original design with a galfenol beam, and 273 Hz and 8.8 $\times 10^{-3}$, for the iterated design. Figure 40 shows the measured and simulated RMS OCV of the original VEH design and the simulated RMS OCV of the iterated design, for a set of β values.

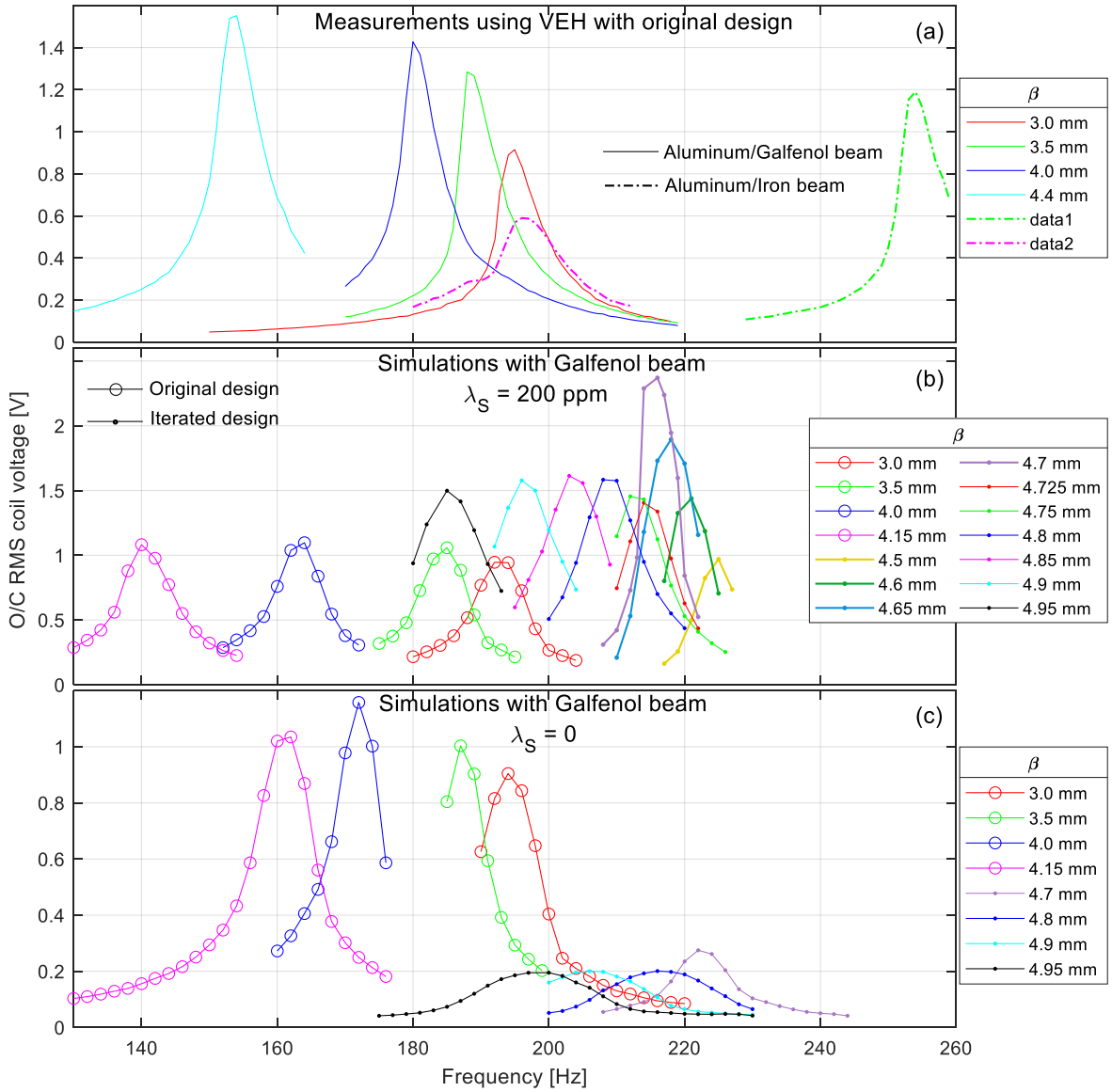

Figure 40. RMS of the open-circuit coil voltage. Curves from right to left result from using an increasingly thicker spacer, i.e. increasing β. (a) Measured values using the original design. Solid lines correspond to using an aluminum/galfenol beam and dashed lines for an aluminum/iron beam. (b) Simulated values of both original and iterated design, with λ_S = 200 ppm. (c) Simulated values of both original and iterated design, with λ_S = 0 ppm. Dots and circles are data points. Lines are for visual aid.

We note first the differences between measurements on the galfenol beam and iron beam, in Figure 40a. From this comparison, it is unclear if magnetostriction is playing a significant role. The iron beam data shows a seemingly larger resonance frequency shift, which could be due to a larger magnetic flux and thus a different relationship between magnetic force and spring force. The voltage amplitude for β = 3.5 mm is close to the values seen in the galfenol beam data, but decreases by 50% at β = 4.5 mm. The trend of increasing RMS voltage for the galfenol beam and decreasing amplitude for the iron beam (although only for two values of β) would however fit with an assumption that increasing β puts the system closer to optimal conditions for magnetostriction in both cases. The negative λ_S (approx. -10 ppm for iron [159]) for iron would then lead to an increasing amount of damping as β is increased, while the positive value of λ_S for galfenol would give the opposite effect. A similar trend can be found in the results of paper I, in which the effect was attributed to their likely being an optimal airgap for a given excitation amplitude.

Comparing the simulation data for the original design with using a galfenol beam, with λ_S = 200 ppm and λ_S = 0 (see Figure 40b and c), we see that the amplitudes are similar, but the resonance frequency tuning is less. Although these results shows that magnetostriction does have a significant effect, at least on the frequency response, it does not implicitly show a significant coupling between the oscillations of the beam and a magnetostrictive, or magnetoelastic, effect. Even a static additional strain from magnetostriction would help to reduce the resonance frequency by further reducing the initial air gap.

Suspecting that, for the original design, there is no significant coupling between the beam's transient behavior and magnetostriction, we looked closer at the magnitude and distribution of the magnetization in the galfenol layer. Figure 41a shows the von Mises stress in the beam and Figure 41b and c show the magnetization, with and without magnetostriction. Comparing these three images we can see that the coupling between stress and magnetization is small, i.e. the difference in magnetization with and without magnetostriction is small. We see also that magnetization is very close to magnetic saturation (M_S is approx. 1.5×10^6 A/m for galfenol [132,160,161]) throughout the beam. From these observations it is clear that the dynamic magnetostrictive effect is very small in the original design. The same comparison for the iterated design (Figure 41d e and f) instead shows a strong coupling between stress and magnetization. Although parts of the galfenol layer are close to M_S in magnetization (Figure 41e), a substantial part has a low to moderate magnetization. As the stress distribution changes due to inertial forces, the magnetization can thus follow, without magnetically saturating the material.

Magnetization simulations of the iterated design show that the magnetic field bias is successfully reduced to levels which may be close to optimal. As the distribution of stress and magnetization are inhomogeneous, it is likely not relevant to state a single value for optimal magnetic field bias or pre-stress. Some regions of the magnetostrictive material will evidently be in either optimal magnetic field bias or pre-stress, however not necessarily at the same time. As the states of pre-stress and magnetic field bias are coupled, only specific combinations are possible, depending on the system configuration. Some configurations may lead to a parameter space far from the global optimum while some configurations may lead

to spatially local optimum conditions (i.e. some region of the magnetostrictive segment may be in optimal magnetic field bias and pre-stress simultaneously).

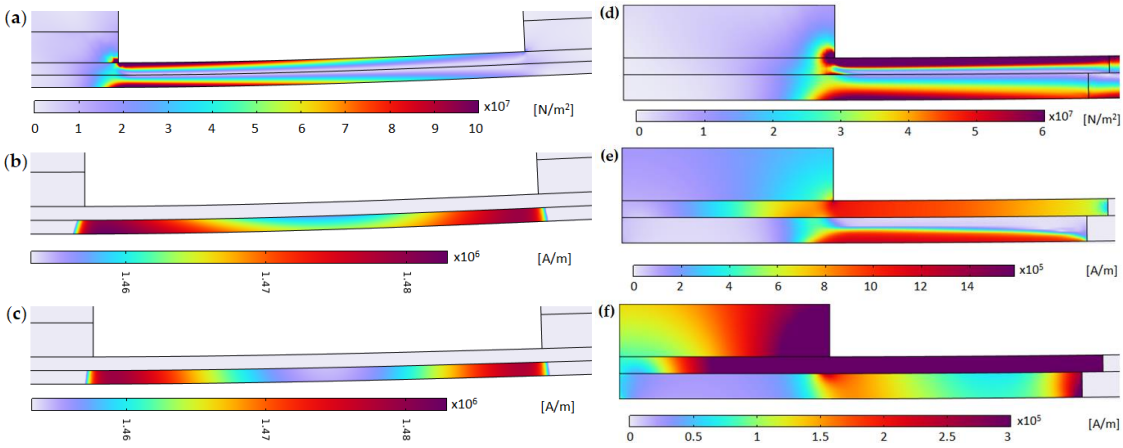

Figure 41. Simulation results in the vicinity of the magnetostrictive component. (a) von Mises stress distributions, original design. (b) Magnetization, original design, $\lambda_S = 200$. (c) Magnetization, original design, $\lambda_S = 0$. (d) von Mises stress distributions, iterated design. (e) Magnetization, iterated design, $\lambda_S = 200$. (f) Magnetization, iterated design, $\lambda_S = 0$.

An issue was noticed while measuring the frequency response of the lab-prototype, when using configurations with a small initial airgap. For a certain small initial airgap (< 1 mm), a decrease in airgap distance over time was noticed, while the shaker was inactive. Given sufficient time (in the order of seconds to tens of seconds), the two components making up the airgap would eventually end up in permanent contact (unless pried apart). The exact reason for this was not determined. One hypothesis is that it is due to the plasticity of galfenol (which is not accounted for in COMSOL). It could also be due to the characteristics of the magnetic force and mechanical spring force (as described in paper I), i.e., the state of the system has passed the unstable equilibrium, yet the net force is still small.

As described in paper I, a smaller resonance frequency tuning is expected in the measured data, as compared to simulated (see Figure 40a and b), due to the likely larger total system reluctance of the lab-prototype (as a result of glue gaps). The fact that a smaller initial airgap can be used in the lab-prototype, without the two components making up the airgap coming in contact, indicates that the magnetic flux is less and the reluctance is larger, compared to the simulation model.

Based on the above discussion, the data suggests that the model is qualitatively accurate. It can thus be used on a comparative basis, for design evaluation. Additional measurements and a second prototype for the iterated design are required to determine the model's quantitative accuracy.

Under the assumption that the COMSOL model can be used comparatively, we compare the simulated frequency response of the original design with that of the iterated design (see Figure 40b). As noted, the iterated design has a stiffer beam, thus the resonance frequencies will be larger for the iterated design. Comparing the data sets β = 3 mm to 4.15 mm for the original design and β = 4.75 mm to 4.95 mm for the iterated design, the behavior is similar. The RMS values at resonance are however roughly 50% larger for the iterated design and the

shift in resonance frequency relative β is much larger. Comparing, again, the data with and without magnetostriction, the differences between these two data sets, for each of the two designs, shows strong similarities. We therefore conclude that magnetostriction improves the "tunability" through the "static" effect of and increased strain bias, effecting the equilibrium state. The 50% increase in OCV however, is a result of utilizing the large local gradients in the magnetostrictive material, arising from a strong coupling to inertial forces. Interestingly, the iterated design seems to provide an optimal combination of magnetic field bias and pre-stress around β = 4.7 mm, as a seemingly continuous increase in OCV can be seen when increasing β from 4.5 mm.

CHAPTER 4

General modelling of vibrational energy harvesters

4.1 Introduction to modelling of vibration energy harvesters

Creating a model to predict the behavior of a VEH system is useful for both development of VEH prototypes and probing the characteristics of the system. As the purpose of any VEH is to convert mechanical energy to electrical energy, it can always be described by work done in the mechanical domain and in the electrical domain, with an electromechanical coupling factor defining the energy transfer between domains.

The modeling of a physical system, be it mechanical or electrical can be either lumped or distributed. The distributed model accounts for a parameter distribution across the geometry of the system while the lumped model assumes that each parameter can be characterized in a single point, or between two points. The cantilever beam PEH is a good example as both lumped and distributed mechanical models are used in literature. It is unlikely that a distributed model for the mechanical domain would be warranted for an EMEH, unless it uses a flexible induction coil or the field generating material is flexible.

The lumped mechanical system of a cantilever VEH can be summarized by a free-body diagram, as shown in Figure 42 right. The diagram consists of mass, spring and dampeners. The mass should be taken as an effective mass, i.e. describing the effect of the distributed mass as one acting only on the beam tip. The spring acts as a force restoring the beam tip to equilibrium and the dampeners retard the movement of the tip.

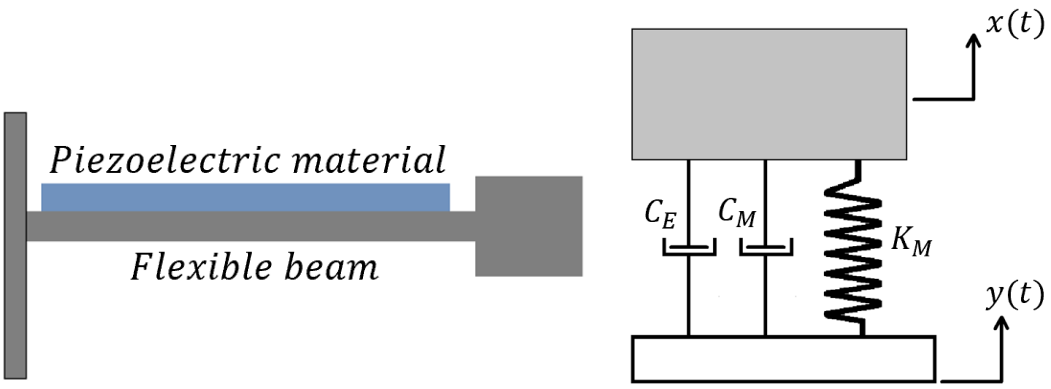

Figure 42. Representation of PEH (right) with a corresponding free body diagram (left). C_E and C_M are the electrical and mechanical damping coefficients. k_M is the mechanical spring coefficient. m is the effective mass of the system. $x(t)$ is the proof mass or tip displacement and $y(t)$ is the base displacement.

For a clamped-free beam with base excitation $y(t)$, the displacement $x(t)$ of the beam tip is given by Equation (11). Mechanical damping and stiffness are given by C_M and K_M, both assuming no effects from the electromechanical coupling, m is the effective mass and f is the electrical damping force.

$$m\ddot{x} + C_M\dot{x} + K_M x + f = m\ddot{y} \qquad (11)$$

The electrical domain is described by the lumped element model of Figure 43. The piezoelectric layer is here modeled as a current source, i, in parallel with a capacitance, C_P, and resistance, R_P. The capacitance is a result of the electrode separated by a thin dielectric. The resistance is a result of the resistivity of the system. Kirchhoff's law can then be used to derive Equation (12).

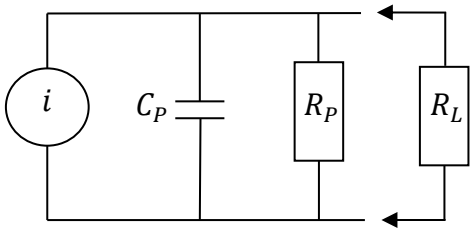

Figure 43. Lumped element model of electrical domain for a PEH. C_P, R_P, R_L are the capacitance, resistance due to PEH resistivity and load resistance. i is the generated current.

$$i = C_P\dot{v} + \frac{v}{R_L} + \frac{v}{R_P} \qquad (12)$$

The distributed bending behavior of a beam was well established at the beginning of the 1900s, resulting in e.g. the Timoshenko–Ehrenfest beam theory [162]. A simpler form, which is commonly used today and referred to as Euler-Bernoulli beam theory, was derived by Daniel Bernoulli and Leonard Euler and published in 1744 [163,164]. This theory states that the relationship governing the one-dimensional bending shape in a beam is given by Equations (13) and (14):

$$M = -EI\frac{d^2\omega}{dx^2} \qquad (13)$$

$$\frac{d^2}{dx^2}\left[EI\frac{d^2\omega}{dx^2}\right] = p \qquad (14)$$

Where ω is the beam deflection at a point x, p is the applied force per unit length, E is the elastic modulus, I is the second moment of area of the beam's cross section and M is the bending moment. Some assumptions within this theory are that the beam deflection is small, the load is only lateral and shear deformation and rotatory inertia can be ignored [162].

The equation of motion based on the distributed model has the same form as the lumped model, but uses the distributed forces as derived by Euler-Bernoulli beam theory. The sum of forces is in this case given by Equation (15), where c_s is the internal viscoelastic damping, c_a

is the air damping, m is the mass per unit length, ω_b is the base displacement and ω_{rel} is the beam displacement relative the base [165,166]. The effect of the beam's mechanical stiffness and the electrical damping is included in $M(x,t)$. Mechanical damping effects are included as a strain-rate damping, due to internal friction, and viscous air damping.

$$\frac{\partial^2 M(x,t)}{\partial x^2} + c_s I \frac{\partial^5 \omega_{rel}(x,t)}{\partial x^4 \partial t} + c_a \frac{\partial \omega_{rel}(x,t)}{\partial t} + m\frac{\partial^2 \omega_{rel}(x,t)}{\partial t^2} = m\frac{\partial^2 \omega_b(x,t)}{\partial t^2} - c_a \frac{\partial \omega_b(x,t)}{\partial t} \qquad (15)$$

The circuit equation is identical to the lumped case. The PEH current can now be derived using the piezoelectric constitutive equations together with the Euler-Bernoulli beam theory [165], resulting in Equation (16). d_{31} is the piezoelectric constant, Y_p is the young's modulus of the PZT material, h_{pc} is the thickness of the PZT layer, b is the width of the beam and L is the length of beam.

$$C_P \frac{dv(t)}{dt} + \frac{v(t)}{R_L} = -\int_{x=0}^{L} d_{31} Y_p h_{pc} b \frac{\partial^3 \omega_{rel}(x,t)}{\partial x^2 \partial t} \qquad (16)$$

There are additional methods to model a VEH, such as Finite Element modeling or with a circuit equivalent model.

A sub-field of research in VEH modeling is unified modeling of VEH's. The lumped model for the mechanical domain can be the same for different types of VEH. As an example, a magnet attached to a base by a spring, oscillating within a coil (see Figure 44) is described by the same free-body diagram as in Figure 42 left. By a suitable choice of dimensionless variables, both PEH and EMEH power performance can be expressed in the same way. Analysis of such a unified model can highlight the strengths and weaknesses of different types of VEH. It can also provide a useful tool to be used in the development of prototype VEH's.

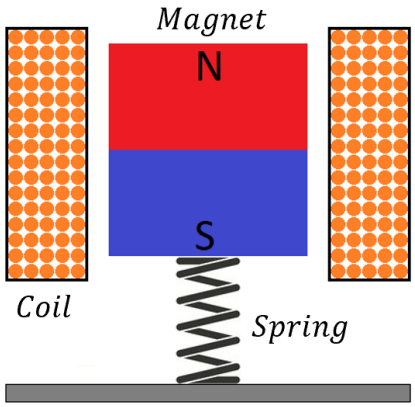

Figure 44. Representation of an EMEH.

4.2 Analysis of a unified model for vibration energy harvesters

In paper II, the derivation of such a unified model is given for the case of PEH and EMEH. To further probe the system characteristics, both harmonic base excitation and a prescribed displacement are considered. The optimal values of power, load resistance and excitation frequency, in dimensionless form, are explored in the space of normalized quality factor, k,

and normalized internal resistance, ξ_E. The internal resistance here refers either R_P as defined in Figure 43 or R_w as defined in Figure 45. The expressions for the dimensionless parameters are given in Table 5. ω_N is here the natural frequency of the VEH. R_P, R_w, R_L, C_P and L are described in Figure 43 and Figure 45. Q_{Crit} is the mechanical quality factor at which the system, under resonance and negligible internal resistance, reaches a theoretical maximum in output power [167].

Table 5. Dimensionless parameters.

Parameter	Expression	Name
k	Q/Q_{Crit}	Normalized quality factor
γ	ω/ω_N	Normalized angular excitation frequency
ξ_C	$PEH\colon 1/R_L\omega_N C_P$ $EMEH\colon R_L/\omega_N L$	Normalized load resistance
ξ_E	$PEH\colon 1/R_P\omega_N C_P$ $EMEH\colon R_W/\omega_N L$	Normalized internal resistance

The model in paper II is derived from Equation (11) and the lumped element models for a PEH and EMEH (see Figure 43 and Figure 45 and Equations (12) and (17)).

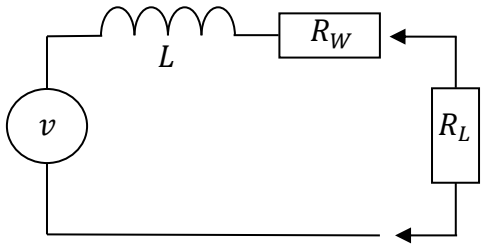

Figure 45. Lumped element model of electrical domain for an EMEH. L, R_w, R_L are the coil inductance, coil resistance and load resistance. v is the generated voltage.

$$v = L\frac{di}{dt} + (R_w + R_L)i \qquad (17)$$

Based on these sets of equations, the relationship between the mechanical and electrical parameters can theoretically be analytically solved in the frequency domain under the assumption of harmonic signals. In practice however, the complexity of the problem, taking into account all parameters, seems to prohibit a solution to be found. This is typically not an issue in most literature, where at least one parameter is deemed insignificant. As an example, the internal resistance could be assumed as much smaller or larger than the load resistance and, depending on the VEH type, could then be excluded from the model without significant effect on the model accuracy. This can be applicable for certain load cases and when dealing with a certain type of VEH, but a unified model without a defined load (other than that it is purely resistive) cannot make these assumptions. Thus, the analytical solution can only be taken so far before numerical methods need to be implemented.

The locally optimal values of the dimensionless excitation frequency, γ, and dimensionless load resistance, ξ_C, can be found by finding the intersections of solutions to $\partial\bar{P}_{IL}/\partial\xi_C = 0$ and

$\partial \bar{P}_{IL}/\partial\gamma = 0$. A numerical method for solving this problem can be derived from the following requirement:

> A value of ξ_C lies in the intersection to the solutions to $\partial \bar{P}_{IL}/\partial\xi_C = 0$ and $\partial \bar{P}_{IL}/\partial\gamma = 0$ if this value, input to solution for $\partial \bar{P}_{IL}/\partial\gamma = 0$, generates a value of γ that when input to the solution for $\partial \bar{P}_{IL}/\partial\xi_C = 0$ generates again the initial input value of ξ_C.

To numerically find all the values of ξ_C which fullfill this requirement a M×N data set is defined, corresponding to all the descrete combinations of ξ_C and ξ_E in a chosen range, where M and N are the number of discrete values for each parameter. For a set value of k, which will be incremented in small steps, the analytical solution to $\partial \bar{P}_{IL}/\partial\gamma = 0$ is used to acquire the M×N numerical values for optimal γ. The numerical output of γ_{Opt} in then used as input to the analytical solution to $\partial \bar{P}_{IL}/\partial\xi_C = 0$. The numerical computation then consists of finding the zeros of $\xi_C - \xi_{C\_Opt}$. A linear fit is used to find the near-zero crossings. The above algorithm is performed over a range of k-values, resulting in the power optimal values of γ and ξ_C in the space of k vs ξ_E.

There exists a certain relationship between ξ_E and k where, for small values of ξ_E or large values of k, there are three zeros in $\xi_C - \xi_{C\_Opt}$. Figure 45 left shows this region for the case of $k = 1.1$ and Figure 45 right shows the lack of such a region for $k = 0.9$. One of the three solutions correspond to a local minimum in power. The other two corresponds to the systems resonance and anti-resonance states (as described earlier in section 1.4.1). The numerical analysis can thus show the relationship between quality factor and intrinsic resistance at which a VEH system will exhibit anti-resonance. Figure 47 shows this boundary, dubbed k_{crit}, at various values of the effective electromechanical coupling coefficient, η, which is the electromechanical coupling normalized by mechanical stiffness and inductance or capacitance.

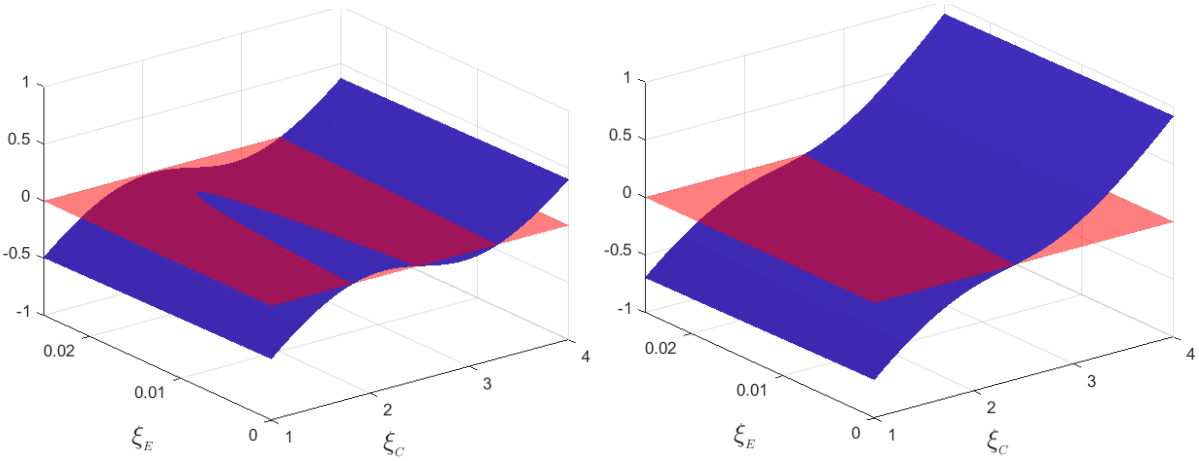

Figure 46. Surfaces of $\xi_C - \xi_{C\_Opt}$ in blue with the zero-plane in red. Left: $k = 1.1$. Right: $k = 0.9$.

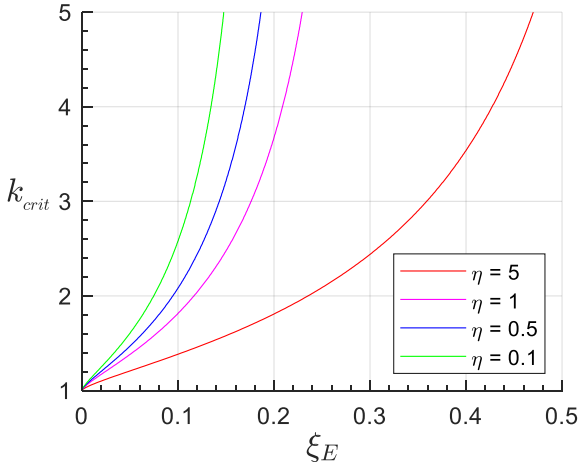

Figure 47. Minimum value of k required for the existence of an anti-resonant solution. $\eta = \{0.1, 0.5, 1, 5\}$, from left to right.

The raw output from the numerical calculations described above are the surfaces, in k-ξ_E space, for the power optimal values of γ and ξ_C as well as the values of optimal power and efficiency in the same space. Analyzing these surfaces can provide a clearer picture of the behavior of VEH systems and result in new insights. From Figure 48 we can see the region where the typical assumption, that resonance occurs at the natural frequency, is true. We can see that the resonance frequency tends towards the natural frequency at large k and the anti-resonant frequency towards $\sqrt{1+\eta}$ (if $\eta = 1$ then this value is 1.41).

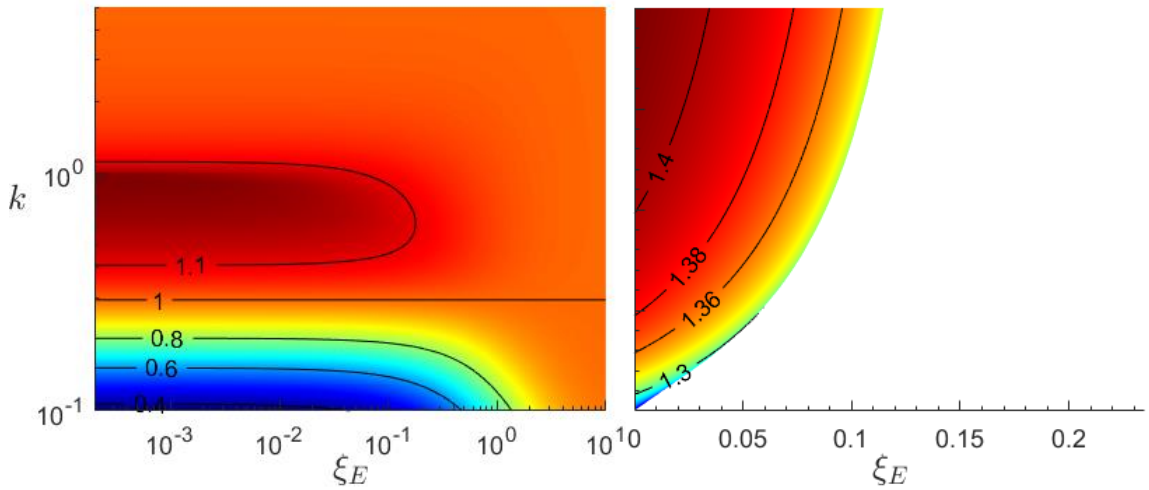

Figure 48. Normalized angular excitation frequency under the condition of power optimal load and $\eta = 1$. Left: at resonance. Right: at anti-resonance. The color scale is linear and independent for each plot

Assuming we can design an arbitrary EMEH or PEH to operate either at the resonant or the anti-resonant state, the two VEH systems will benefit differently from operating under either condition. From the numerical results we can compare these states regarding the key performance parameters: output voltage, power and efficiency

As described earlier, in section 1.2, a VEH system will in general include circuitry for rectification of the generated signal. The diodes typically used in such circuitry can have a

substantial voltage drop across them (ranging between approximately 0.2 V to 0.7 V depending on the type of diode). Luckily this voltage drop is absolute and the larger the output voltage from the VEH the smaller the proportion of power is lost in the diodes. Due to the series nature of the EMEH circuit model, a large output voltage is obtained when ξ_C is large and ξ_E is small, while for a PEH both should be small. From the results in Figure 50 left and Figure 49 we can see that a system run at resonance can in general achieve large values of optimal ξ_C at high k values. On the contrary, values of optimal $\xi_C \ll 1$ at resonance require large values of η and $k \ll 1$. Only at anti-resonance (see Figure 50 right) can we achieve an optimal $\xi_C \ll 1$ at small values of η. In both cases (PEH/EMEH) an increasingly beneficial value of optimal ξ_C, with regards to output voltage, is achieved at increasing k. In a similar sense, the power characteristics at anti-resonance (Figure 51 right) also favor the PEH over the EMEH as the power rapidly declines at increasing ξ_E and k, while it is close to its theoretical maximum for $\xi_E \ll 1$, regardless of k.

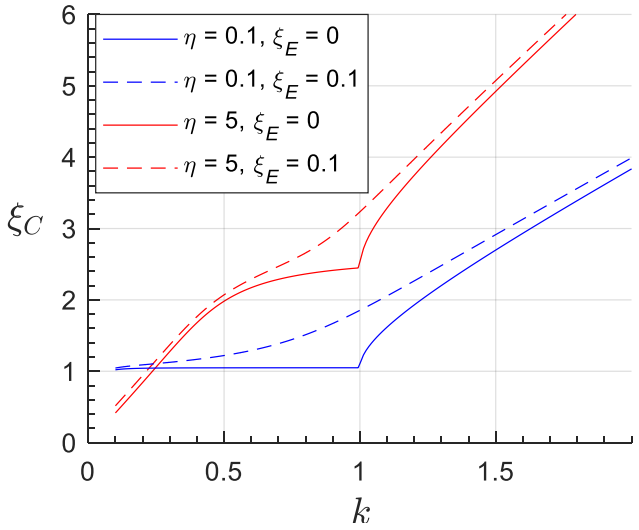

Figure 49. Optimum normalized load resistance, at resonant excitation frequency. $\eta = \{5, 1\}$ and $\xi_E = \{0, 0.1\}$

Looking to Table 5 we can see that the practical design parameters available, for manipulating ξ_C and ξ_E are ω_N, C_P, L, R_W, R_P and R_L. Spring stiffness and mass determines ω_N, which for a cantilever beam with proof mass is determined by beam width, thickness, Young's modulus and proof mass weight. Electrode area, electrode separation and dielectric material properties determine both C_p and R_P. Coil geometry (length and area) and number of windings determine L for an air wound coil. Coil wire length and conductivity determine R_W. R_L is determined by the load electronics. Based on the argument from the previous paragraph and assuming the PEH is limited to small η, the parameters ω_N, C_P, R_P and R_L should all be maximized for the PEH. For the EMEH, ω_N, L and R_W should be minimized while R_L is maximized. As mentioned in the previous paragraph, a high *k*-value is beneficial with regards to power output and voltage (at resonance and anti-resonance). The parameter *k* is a function of ω_N and η as well as mass and mechanical damping. Due to the overlap between the parameters ξ_C, ξ_E, η and k, finding the optimal geometry and material properties, while adhering to the power optimal proportionalities, is a complex task for both types of VEH.

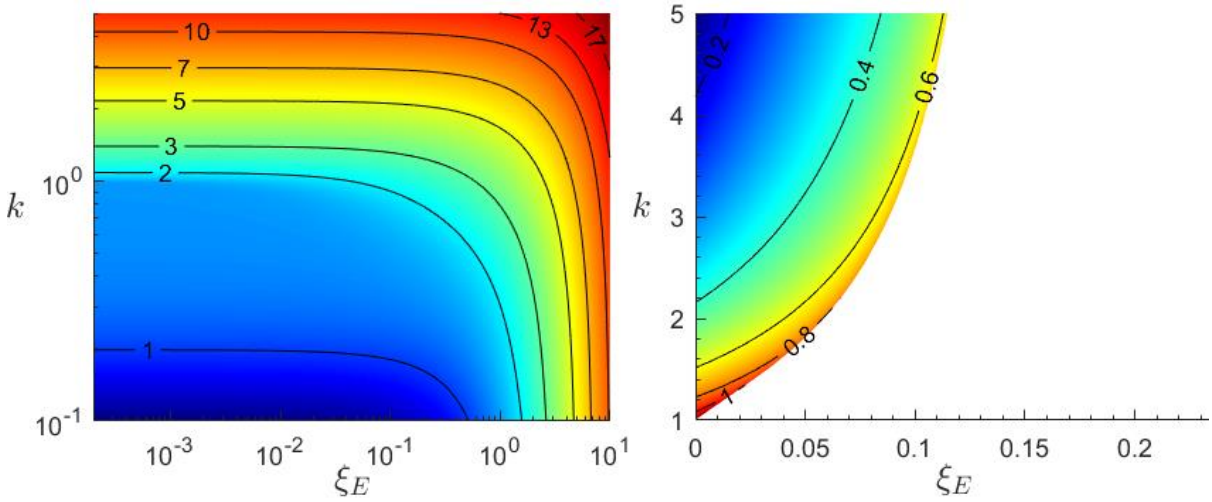

Figure 50. Power optimum normalized load resistance for $\eta = 1$. Left: at resonance. Right: at anti-resonance. The color scale is logarithmic and independent for each plot

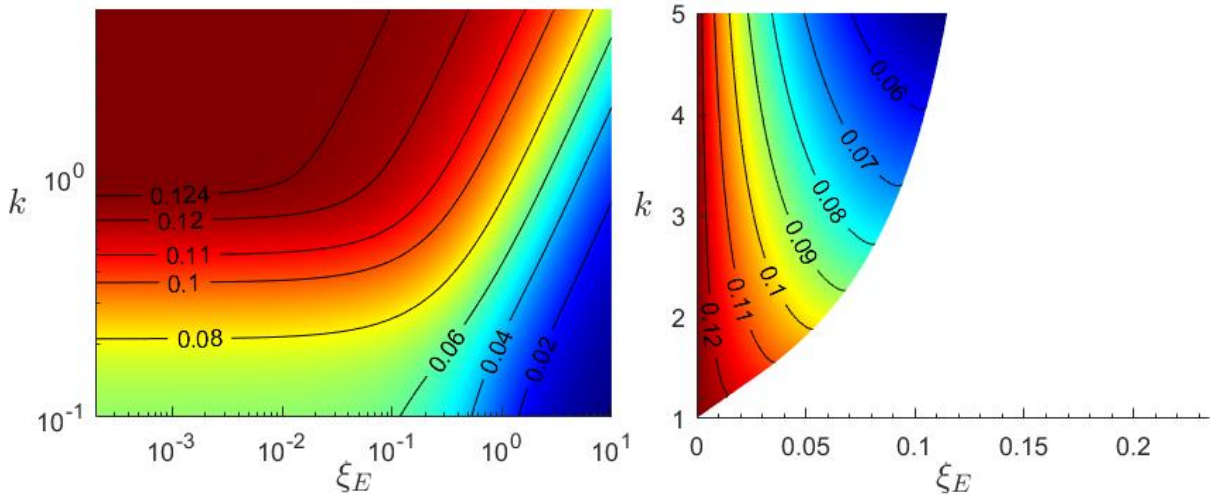

Figure 51. Dimensionless power at optimal load and $\eta = 1$. Left: at resonance. Right: at anti-resonance. The color scale is linear and independent for each plot.

In the region of $k > 1$, in Figure 51, it can be derived that the dependance between the ratio k/ξ_E and value of $\bar{P}$ to be traced follows a logarithmic slope. Figure 52 shows k/ξ_E as a function of $\bar{P}$ at $\eta = \{5,1,0.1\}$. We can see that the sensitivity of k to ξ_E increases dramatically near the theoretical power maximum. The quality factor and/or effective coupling coefficient required to achieve a power output close to the theoretical maximum can thus become large for energy harvesters with large loss coefficient, such as for a typical EMEH.

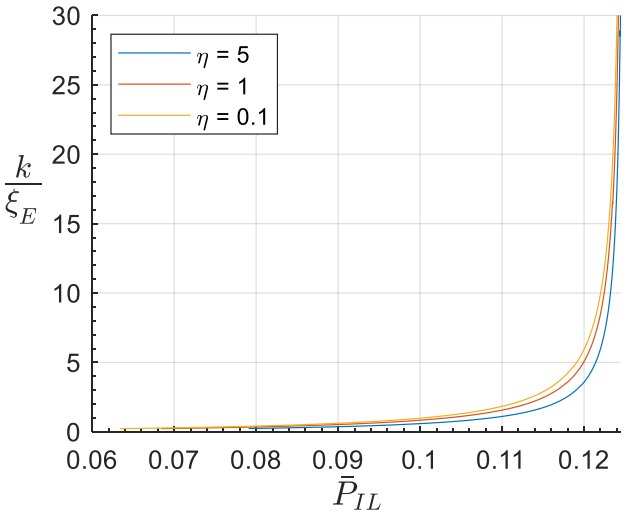

Figure 52. Sensitivity of k to ξ_E as a function of dimensionless power, i.e., the ratio of k to ξ_E when tracing a specific power value. This relationship only holds for $k>1$.

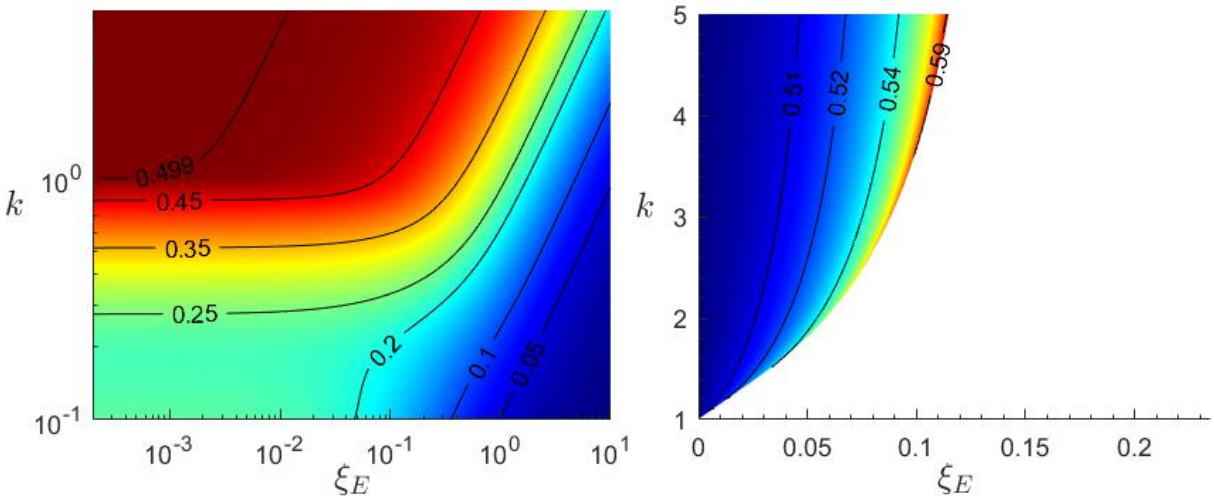

Figure 53. Power input to output efficiency under the condition of power optimal load and $\eta = 1$. Left: at resonance. Right: at anti-resonance. The color scale is linear and independent for each plot.

Assuming load resistance and excitation frequency remain optimized by load power, both VEH systems have a maximum efficiency of 50% at resonance (see Figure 53 left). At antiresonance the efficiency is above 50% (if $\xi_E > 0$) and increasingly so along the boundary of k_{crit}, in the direction of larger k and ξ_E (see Figure 53 right). It may be beneficial to operate in this region if the source power is small. If we instead assume an arbitrary γ and a load optimized by efficiency, the efficiency can approach 100%.

The primary results from modeling assuming a prescribed displacement lie in the validation of the expressions derived for the model with base excitation. The expressions for efficiency are equal in both cases, which is intuitive assuming efficiency is a purely intrinsic property. Optimal load resistance was also found to differ by only a term related to the electric damping, an effect negated by prescribed displacement.

To summarize, the results of this chapter help provide a clearer picture of VEH characteristics thanks to the detailed investigation of the effect from the resistive loss coefficient, under both

resonance and anti-resonance. The numerical results described in this chapter take into account all the parameters of the unified lumped VEH model, under the condition of power optimal proportions, and thus a more complete picture is gained compared to previous literature which exclude one or more parameters. New insights gained from the analysis can be summarized as the following:

- The critical quality factor specified in previous literature only holds for zero intrinsic resistance and increases with a cubic dependency with increasing intrinsic resistance. This effect is more notable at small values of effective electromechanical coupling coefficient.
- The relationship between optimal load and intrinsic resistance favors the PEH at anti-resonance and the EMEH at resonance.
- The efficiency, under power optimal conditions, is potentially larger at anti-resonance.
- VEH systems with large intrinsic resistance reach a practical power limit before the theoretical limit.

CHAPTER 5

Discussion, conclusion and future work

5.1 Discussion and concluding remarks

The energy required by most small-scale electronics is insignificant next to the total energy of a moving vehicle. The possibility of wirelessly extracting a very small portion of this energy to enable wireless self-sufficient systems is an attractive and today proven concept. VEH to date utilize three main areas of power extraction; tire surface buckling, suspension compression and ambient vibrations. The energy available from additional electrical damping in the suspension is by a wide margin the largest. This is due to that VEH can be strongly coupled to the total oscillating mass of the vehicle. This source of energy is naturally limited to suspension units. Energy harvesters in tires can also make some use of the vehicles mass as they can be coupled directly to the tires surface. The rotating of the wheel can also be used to augment VEH performance. Sources of ambient vibrational energy are available throughout the vehicle, the downside being most of these sources are already significantly damped (perhaps excluding those in direct connection with the engine). Areas close to the passenger seats likely have the least ambient vibrations, for greater passenger comfort. VEH utilizing ambient vibrations make use of inertial forces acting on the components of the VEH, which for small systems leads to small forces and low input energy. This area is therefore the most challenging for achieving large power output.

This thesis describes two energy harvesters for scavenging ambient vibrations within a vehicle, one utilizing piezoelectricity and the other magnet induction. The described PEH placed on the flexplate likely has a larger source of power compared to the EMEH on the belt-buckle, naturally leading to more harvested power. The described PEH is an example of a VEH utilizing the environment, centrifugal force and gravitational pull in this case, to boost the output performance and reduce required size. The EMEH on belt buckle has no such advantages and must have high performance in order to produce significant power from the small vibration environment. There is also a natural size limit. A VEH larger than the belt-buckle would likely be deemed too bulky. The described macroscale EMEH has a simple design but still manages a large power density and a usable power output if intermittent communication can be accepted. The low-level vibration capabilities make this EMEH a likely competitive VEH in many other areas of the vehicle. The work exploring the addition of magnetostriction showed promising results and indicate that the power output and power density of the belt buckle VEH can be further increased by incorporating magnetostriction. Adding to this a system for extracting energy from buckling in and out and it may be feasible to build a system which can

power a belt buckle wireless sensor node for the duration of the vehicle transit, without the need for a battery.

The market trend towards an increasing number of purely electric vehicles may put additional requirements for ambient vibration VEH in vehicles; without a combustion engine a significant source of vibration is gone. The current limitation in travel range of electrical vehicles has likely put a strict requirement on energy management and weight minimization. Thus, the additional weight and energy consumption due to a VEH needs to be well justified. Safety sensors may have additional requirements inhibiting the use of a VEH as sole power source.

Which type of transduction mechanism to choose can be a difficult choice as successful attempts to mitigate the weaknesses of each can be found in most research areas. The solutions can be more or less complex, and it can therefore still be of interest to explore the pros and cons of the basic VEH systems. Unified modeling of VEHs provides a tool for such an analysis. Although such a model can highlight useful characteristics the unified aspect creates the need for a simplified lumped model. The strain distribution in the piezoelectric layer is a key parameter which is lost in the lumped model. The unified model described in paper II requires the use of numerical methods. A complete analytical expression would be of more use.

Surveying the research field of vibrational energy harvesting in vehicles we find that there are several regions where a VEH can be of use. The stochastic resonance PEH described here shows potential for an efficient VEH in a rotational environment. The demonstrated use of VEHs for ambient vibrations in the passenger/driver area is missing in literature. The EMEH described here shows the potential implementation of such a VEH. From the sample of VEH found in tables 2 to 4, there are several which would be of interest to use in the passenger/driver area due to their small size, although they have not been evaluated in this context. The results from papers I and IV indicate that the described systems have the potential of large resonance frequency tuning (orders of magnitude larger than any other of the reviewed systems). In the context of vibrational energy harvesting in vehicles, where the excitation spectrum is affected by vehicle speed, the possibility to actively control the resonance frequency, over a significant frequency range, becomes highly beneficial.

5.2 Future work

Of the two VEHs for ambient vehicle vibrations, described in this thesis, none are rigorously optimized and thus this work needs to be performed to determine their true potential. In both cases an improved experimental test setup would be beneficial for system characterization and optimization. Further prototyping and lab measurements are required to confirm all the beneficial effects of combining magnetostriction with the concept described in paper I. As the design described in paper I showed promise, a modification of this design, incorporating magnetostriction could be derived and experimentally tested.

To rigorously prove the usefulness of the belt buckle energy harvesters described in this work, a complete system with both VEH and mechanical transient energy harvester, power management electronics and transmitter, could be constructed and validated in the field.

The analysis of the unified model could be expanded to include more transduction mechanisms, as these only differ in the electrical domain when using the lumped approach. An attempt could be made to include corrections factors considering the approximations of the lumped model. The analytical results would benefit from a rigorous validation by lab measurements or measurement data from literature (if all necessary data can be extrapolated).

References

[1] Harold I. Sharlin. From Faraday to the Dynamo. Sci Am 1961;204:107–19.

[2] Smith GS. Faraday's first dynamo: A retrospective. Am J Phys 2013;81:907–17. https://doi.org/10.1119/1.4825232.

[3] Algave É, Boulard J, Sloane TO, Lungren CM. The electric light : its history, production, and applications. New York: D. Appleton and Co.; 1884.

[4] Digregorio G, Redouté J-M. Electromagnetic Energy Harvester Targeting Wearable and Biomedical Applications. Sensors 2024;24:2311. https://doi.org/10.3390/s24072311.

[5] Sultan I, Banday MT. Ultra-Low Power Microcontroller Architectures for the Internet of Things (IoT) devices. 2023 5th International Conference on Smart Systems and Inventive Technology (ICSSIT), IEEE; 2023, p. 482–8. https://doi.org/10.1109/ICSSIT55814.2023.10060949.

[6] Kopta V, Enz C. Ultra-Low Power FM-UWB Transceivers for IoT. River Publishers; 2019.

[7] Schumacher T, Stadelmayer M, Faseth T, Pretl H. A Review of Ultra-Low-Power and Low-Cost Transceiver Design. 2017 Austrochip Workshop on Microelectronics (Austrochip), IEEE; 2017, p. 29–34. https://doi.org/10.1109/Austrochip.2017.15.

[8] Jahan MS, Langford J, Holleman J. A low-power FSK/OOK transmitter for 915 MHz ISM band. 2015 IEEE Radio Frequency Integrated Circuits Symposium (RFIC), IEEE; 2015, p. 163–6. https://doi.org/10.1109/RFIC.2015.7337730.

[9] Kopta V, Enz CC. A 4-GHz Low-Power, Multi-User Approximate Zero-IF FM-UWB Transceiver for IoT. IEEE J Solid-State Circuits 2019;54:2462–74. https://doi.org/10.1109/JSSC.2019.2917837.

[10] Sondej T, Bednarczyk M. Ultra-Low-Power Sensor Nodes for Real-Time Synchronous and High-Accuracy Timing Wireless Data Acquisition. Sensors 2024;24:4871. https://doi.org/10.3390/s24154871.

[11] Bai Y, Jantunen H, Juuti J. Energy Harvesting Research: The Road from Single Source to Multisource. Advanced Materials 2018;30:1707271. https://doi.org/10.1002/adma.201707271.

[12] Sun R, Zhou S, Cheng L. Ultra-low frequency vibration energy harvesting: Mechanisms, enhancement techniques, and scaling laws. Energy Convers Manag 2023;276:116585. https://doi.org/10.1016/j.enconman.2022.116585.

[13] Siang J, Lim MH, Salman Leong M. Review of vibration-based energy harvesting technology: Mechanism and architectural approach. Int J Energy Res 2018;42:1866–93. https://doi.org/10.1002/er.3986.

[14] Dong L, Closson AB, Jin C, Trase I, Chen Z, Zhang JXJ. Vibration-Energy-Harvesting System: Transduction Mechanisms, Frequency Tuning Techniques, and Biomechanical Applications. Adv Mater Technol 2019;4. https://doi.org/10.1002/admt.201900177.

[15] Maurya D, Kumar P, Khaleghian S, Sriramdas R, Kang MG, Kishore RA, et al. Energy harvesting and strain sensing in smart tire for next generation autonomous vehicles. Appl Energy 2018;232. https://doi.org/10.1016/j.apenergy.2018.09.183.

[16] Mondal S, Wijewardena K, Karrapuswami S, Kumar D, Chahal P, Ghannam M, et al. A Wireless Battery-less Seat Sensor for Autonomous Vehicles. 2020 IEEE 70th Electronic Components and Technology Conference (ECTC), IEEE; 2020. https://doi.org/10.1109/ECTC32862.2020.00357.

[17] Rui X, Zeng Z, Zhang Y, Li Y, Feng H, Huang X, et al. Design and Experimental Investigation of a Self-Tuning Piezoelectric Energy Harvesting System for Intelligent Vehicle Wheels. IEEE Trans Veh Technol 2020;69. https://doi.org/10.1109/TVT.2019.2959616.

[18] Huang J, Xu C, Ma N, Zhou Q, Ji Z, Jia C, et al. Intelligent Device for Harvesting the Vibration Energy of the Automobile Exhaust with a Piezoelectric Generator. Micromachines (Basel) 2023;14:491. https://doi.org/10.3390/mi14020491.

[19] Pepe G, Doria A, Roveri N, Carcaterra A. Vibration energy harvesting for cars: semi-active piezo controllers. Archive of Applied Mechanics 2022. https://doi.org/10.1007/s00419-022-02292-1.

[20] Zhu D, Wang L, Henaut J, Beeby S. Comparisons of Energy Sources for Autonomous In-car Wireless Tags for Asset Tracking and Parking Applications. Procedia Eng 2014;87:783–6. https://doi.org/10.1016/j.proeng.2014.11.680.

[21] Lee JH, Jeong K, Lee J, Yoo S, Lee B, Ha J, et al. Development of Adaptive Powertrain Control Utilizing ADAS and GPS, 2019. https://doi.org/10.4271/2019-01-0883.

[22] Sivertsson M, Sundström C, Eriksson L. Adaptive Control of a Hybrid Powertrain with Map-based ECMS. IFAC Proceedings Volumes 2011;44:2949–54. https://doi.org/10.3182/20110828-6-IT-1002.02091.

[23] Pandharipande A, Cheng C-H, Dauwels J, Gurbuz SZ, Ibanez-Guzman J, Li G, et al. Sensing and Machine Learning for Automotive Perception: A Review. IEEE Sens J 2023;23:11097–115. https://doi.org/10.1109/JSEN.2023.3262134.

[24] Sriranga AK, Lu Q, Birrell S. A Systematic Review of In-Vehicle Physiological Indices and Sensor Technology for Driver Mental Workload Monitoring. Sensors 2023;23:2214. https://doi.org/10.3390/s23042214.

[25] Guerrero-Ibáñez J, Zeadally S, Contreras-Castillo J. Sensor Technologies for Intelligent Transportation Systems. Sensors 2018;18:1212. https://doi.org/10.3390/s18041212.

[26] Abdelkareem MAA, Xu L, Ali MKA, Elagouz A, Mi J, Guo S, et al. Vibration energy harvesting in automotive suspension system: A detailed review. Appl Energy 2018;229:672–99. https://doi.org/10.1016/j.apenergy.2018.08.030.

[27] Chilabi HJ, Salleh H, Al-Ashtari W, Supeni EE, Abdullah LC, As'arry AB, et al. Rotational Piezoelectric Energy Harvesting: A Comprehensive Review on Excitation Elements, Designs, and Performances. Energies (Basel) 2021;14:3098. https://doi.org/10.3390/en14113098.

[28] Gao X, Wu J, Yu Y, Dong S. A modified barbell-shaped PNN-PZT-PIN piezoelectric ceramic energy harvester. Appl Phys Lett 2017;111:212904. https://doi.org/10.1063/1.5001803.

[29] Koo B-G, Shin D-J, Lim D-H, Kim M-S, Kim I-S, Jeong S-J. Properties of Car-Embedded Vibrating Type Piezoelectric Harvesting System. Applied Sciences 2021;11:7449. https://doi.org/10.3390/app11167449.

[30] Caban J, Vrabel J, Górnicka D, Nowak R, Jankiewicz M, Matijošius J, et al. Overview of Energy Harvesting Technologies Used in Road Vehicles. Energies (Basel) 2023;16:3787. https://doi.org/10.3390/en16093787.

[31] Kaushik Reddy P, Thakan A. A Comprehensive Analysis of the Design and Functionality of Regenerative Shock Absorbers: A Review, 2024, p. 285–310. https://doi.org/10.1007/978-981-97-3173-2_20.

[32] Ali A, Ahmed A, Ali M, Azam A, Wu X, Zhang Z, et al. A review of energy harvesting from regenerative shock absorber from 2000 to 2021: advancements, emerging applications, and technical challenges. Environmental Science and Pollution Research 2023;30:5371–406. https://doi.org/10.1007/s11356-022-24170-7.

[33] Zhao Z, Wang T, Shi J, Zhang B, Zhang R, Li M, et al. Analysis and application of the piezoelectric energy harvester on light electric logistics vehicle suspension systems. Energy Sci Eng 2019;7:2741–55. https://doi.org/10.1002/ese3.456.

[34] Zhao Z, Wang T, Zhang B, Shi J. Energy Harvesting from Vehicle Suspension System by Piezoelectric Harvester. Math Probl Eng 2019;2019:1–10. https://doi.org/10.1155/2019/1086983.

[35] Alhumaid S, Hess D, Guldiken R. A Noncontact Magneto–Piezo Harvester-Based Vehicle Regenerative Suspension System: An Experimental Study. Energies (Basel) 2022;15:4476. https://doi.org/10.3390/en15124476.

[36] Zhou R, Yan M, Sun F, Jin J, Li Q, Xu F, et al. Experimental validations of a magnetic energy-harvesting suspension and its potential application for self-powered sensing. Energy 2022;239:122205. https://doi.org/10.1016/j.energy.2021.122205.

[37] Esmaeeli R, Aliniagerdroudbari H, Hashemi SR, Alhadri M, Zakri W, Batur C, et al. Design, modeling, and analysis of a high performance piezoelectric energy harvester for intelligent tires. Int J Energy Res 2019;43:5199–212. https://doi.org/10.1002/er.4441.

[38] Seo J, Jhang K-Y, Lee H, Kim Y-C. Vibration energy harvesting technology for smart tire monitoring. Journal of Mechanical Science and Technology 2019;33:3725–32. https://doi.org/10.1007/s12206-019-0714-2.

[39] Miao G, Fang S, Wang S, Zhou S. A low-frequency rotational electromagnetic energy harvester using a magnetic plucking mechanism. Appl Energy 2022;305:117838. https://doi.org/10.1016/j.apenergy.2021.117838.

[40] Paul K, Amann A, Roy S. Tapered nonlinear vibration energy harvester for powering Internet of Things. Appl Energy 2021;283:116267. https://doi.org/10.1016/j.apenergy.2020.116267.

[41] Aktakka EE, Najafi K. A Micro Inertial Energy Harvesting Platform With Self-Supplied Power Management Circuit for Autonomous Wireless Sensor Nodes. IEEE J Solid-State Circuits 2014;49:2017–29. https://doi.org/10.1109/JSSC.2014.2331953.

[42] Kasargod PS, Rashidzadeh R, Ahmadi M. A MEMS based rectifier for energy harvesting. 2017 European Conference on Circuit Theory and Design (ECCTD), IEEE; 2017, p. 1–4. https://doi.org/10.1109/ECCTD.2017.8093296.

[43] Staaf LGH, Lundgren P, Enoksson P. Present and future supercapacitor carbon electrode materials for improved energy storage used in intelligent wireless sensor systems. Nano Energy 2014;9:128–41. https://doi.org/10.1016/j.nanoen.2014.06.028.

[44] Pender JP, Jha G, Youn DH, Ziegler JM, Andoni I, Choi EJ, et al. Electrode Degradation in Lithium-Ion Batteries. ACS Nano 2020;14:1243–95. https://doi.org/10.1021/acsnano.9b04365.

[45] Narita F, Fox M. A Review on Piezoelectric, Magnetostrictive, and Magnetoelectric Materials and Device Technologies for Energy Harvesting Applications. Adv Eng Mater 2018;20. https://doi.org/10.1002/adem.201700743.

[46] Apicella V, Clemente CS, Davino D, Leone D, Visone C. Review of Modeling and Control of Magnetostrictive Actuators. Actuators 2019;8. https://doi.org/10.3390/act8020045.

[47] Bjurström J, Ohlsson F, Rusu C, Johansson C. Unified Modeling and Analysis of Vibration Energy Harvesters under Inertial Loads and Prescribed Displacements. Applied Sciences 2022;12:9815. https://doi.org/10.3390/app12199815.

[48] Wang ZL. Triboelectric Nanogenerators as New Energy Technology for Self-Powered Systems and as Active Mechanical and Chemical Sensors. ACS Nano 2013;7:9533–57. https://doi.org/10.1021/nn404614z.

[49] Munirathinam P, Anna Mathew A, Shanmugasundaram V, Vivekananthan V, Purusothaman Y, Kim S-J, et al. A comprehensive review on triboelectric nanogenerators based on Real-Time applications in energy harvesting and Self-Powered sensing. Materials Science and Engineering: B 2023;297:116762. https://doi.org/10.1016/j.mseb.2023.116762.

[50] Boisseau S, Despesse G, Ahmed B. Electrostatic Conversion for Vibration Energy Harvesting. Small-Scale Energy Harvesting, InTech; 2012. https://doi.org/10.5772/51360.

[51] Tang G, Cheng F, Hu X, Huang B, Xu B, Li Z, et al. A Two-Degree-of-Freedom Cantilever-Based Vibration Triboelectric Nanogenerator for Low-Frequency and Broadband Operation. Electronics (Basel) 2019;8:1526. https://doi.org/10.3390/electronics8121526.

[52] Halvorsen E, Nguyen SD. MEMS Electrostatic Energy Harvesters with Nonlinear Springs. Advances in Energy Harvesting Methods, New York, NY: Springer New York; 2013, p. 63–90. https://doi.org/10.1007/978-1-4614-5705-3_3.

[53] Harne RL, Wang KW. A review of the recent research on vibration energy harvesting via bistable systems. Smart Mater Struct 2013;22:023001. https://doi.org/10.1088/0964-1726/22/2/023001.

[54] Halim MA, Kim DH, Park JY. Low Frequency Vibration Energy Harvester Using Stopper-Engaged Dynamic Magnifier for Increased Power and Wide Bandwidth. Journal of Electrical Engineering and Technology 2016;11. https://doi.org/10.5370/JEET.2016.11.3.707.

[55] Tri Nguyen H, Genov DA, Bardaweel H. Vibration energy harvesting using magnetic spring based nonlinear oscillators: Design strategies and insights. Appl Energy 2020;269. https://doi.org/10.1016/j.apenergy.2020.115102.

[56] Pertin O, Guha K, Jakšić O, Jakšić Z, Iannacci J. Investigation of Nonlinear Piezoelectric Energy Harvester for Low-Frequency and Wideband Applications. Micromachines (Basel) 2022;13:1399. https://doi.org/10.3390/mi13091399.

[57] Ghandchi Tehrani M, Elliott SJ. Extending the dynamic range of an energy harvester using nonlinear damping. J Sound Vib 2014;333. https://doi.org/10.1016/j.jsv.2013.09.035.

[58] Colin M, Basrour S, Rufer L, Bantignies C, Nguyen-Dinh A. Highly Efficient Low-frequency Energy Harvester Using Bulk Piezoelectric Ceramics. J Phys Conf Ser 2013;476:012133. https://doi.org/10.1088/1742-6596/476/1/012133.

[59] IEEE Standard on Piezoelectricity. ANSI/IEEE Std 176-1987 1988:0_1.

[60] Priya S, Inman DJ, editors. Energy Harvesting Technologies. Boston, MA: Springer US; 2009. https://doi.org/10.1007/978-0-387-76464-1.

[61] Rajasekar S, Sanjuan MAF. Nonlinear Resonances. Cham: Springer International Publishing; 2016. https://doi.org/10.1007/978-3-319-24886-8.

[62] Ando B, Baglio S, Bulsara AR, Marletta V. A Nonlinear Energy Harvester Operated in the Stochastic Resonance Regime for Signal Detection/Measurement Applications. IEEE Trans Instrum Meas 2020;69:5930–40. https://doi.org/10.1109/TIM.2019.2957913.

[63] Cammarano A, Burrow SG, Barton DAW, Carrella A, Clare LR. Tuning a resonant energy harvester using a generalized electrical load. Smart Mater Struct 2010;19:055003. https://doi.org/10.1088/0964-1726/19/5/055003.

[64] Brenes A, Morel A, Juillard J, Lefeuvre E, Badel A. Maximum power point of piezoelectric energy harvesters: a review of optimality condition for electrical tuning. Smart Mater Struct 2020;29:033001. https://doi.org/10.1088/1361-665X/ab6484.

[65] KATZIR S. The Discovery of the Piezoelectric Effect. Arch Hist Exact Sci 2003;57:61–91. https://doi.org/10.1007/s00407-002-0059-5.

[66] Fundamentals of Piezoelectricity. Piezoelectric Transducers for Vibration Control and Damping, London: Springer-Verlag; n.d., p. 9–35. https://doi.org/10.1007/1-84628-332-9_2.

[67] Smith M, Kar-Narayan S. Piezoelectric polymers: theory, challenges and opportunities. International Materials Reviews 2022;67:65–88. https://doi.org/10.1080/09506608.2021.1915935.

[68] Fraden J. Handbook of Modern Sensors. Cham: Springer International Publishing; 2016. https://doi.org/10.1007/978-3-319-19303-8.

[69] Ballas RG. The Piezoelectric Effect – an Indispensable Solid State Effect for Contemporary Actuator and Sensor Technologies. J Phys Conf Ser 2021;1775:012012. https://doi.org/10.1088/1742-6596/1775/1/012012.

[70] Safari A, Akdoğan EK, editors. Piezoelectric and Acoustic Materials for Transducer Applications. Boston, MA: Springer US; 2008. https://doi.org/10.1007/978-0-387-76540-2.

[71] JAFFE H. Piezoelectric Ceramics. Journal of the American Ceramic Society 1958;41:494–8. https://doi.org/10.1111/j.1151-2916.1958.tb12903.x.

[72] Pinin. Perovskite structure of PZT. Wikimedia Commons 2010.

[73] Carpi F, editor. Electromechanically Active Polymers. Cham: Springer International Publishing; 2016. https://doi.org/10.1007/978-3-319-31530-0.

[74] Jones G, Assink R, Dargaville T, Chaplya P, Clough R, Elliott J, et al. Characterization, performance and optimization of PVDF as a piezoelectric film for advanced space mirror concepts. Albuquerque, NM, and Livermore, CA (United States): 2005. https://doi.org/10.2172/876343.

[75] Park S, Kim Y, Jung H, Park J-Y, Lee N, Seo Y. Energy harvesting efficiency of piezoelectric polymer film with graphene and metal electrodes. Sci Rep 2017;7:17290. https://doi.org/10.1038/s41598-017-17791-3.

[76] Rivas M, Rudy RQ, Sanchez B, Graziano MB, Fox GR, Sunal P, et al. Iridium oxide top electrodes for piezo- and pyroelectric performance enhancements in lead zirconate titanate thin-film devices. J Mater Sci 2020;55:10351–63. https://doi.org/10.1007/s10853-020-04766-5.

[77] Fu H, Chen G, Bai N. Electrode Coverage Optimization for Piezoelectric Energy Harvesting from Tip Excitation. Sensors 2018;18:804. https://doi.org/10.3390/s18030804.

[78] Jing-Feng Li. Fundamentals of Piezoelectricity. Lead-Free Piezoelectric Materials. first, WILEY; 2021.

[79] Kim T, Ko Y, Yoo C, Choi B, Han S, Kim N. Design optimisation of wide-band piezoelectric energy harvesters for self-powered devices. Energy Convers Manag 2020;225:113443. https://doi.org/10.1016/j.enconman.2020.113443.

[80] Bouhedma S, Rao Y, Schütz A, Yuan C, Hu S, Lange F, et al. System-Level Model and Simulation of a Frequency-Tunable Vibration Energy Harvester. Micromachines (Basel) 2020;11:91. https://doi.org/10.3390/mi11010091.

[81] Jiang J, Liu S, Feng L, Zhao D. A Review of Piezoelectric Vibration Energy Harvesting with Magnetic Coupling Based on Different Structural Characteristics. Micromachines (Basel) 2021;12:436. https://doi.org/10.3390/mi12040436.

[82] Sun S, Leng Y, Hur S, Sun F, Su X, Song H-C, et al. Energy Harvesting Performance of a Novel Nonlinear Quad-Stable Piezoelectric Energy Harvester with Only One External Magnet. Machines 2022;10:803. https://doi.org/10.3390/machines10090803.

[83] Dhote S, Li H, Yang Z. Multi-frequency responses of compliant orthoplanar spring designs for widening the bandwidth of piezoelectric energy harvesters. Int J Mech Sci 2019;157–158:684–91. https://doi.org/10.1016/j.ijmecsci.2019.04.029.

[84] Chen K, Fang S, Gao Q, Zou D, Cao J, Liao W-H. An enhanced nonlinear piezoelectric energy harvester with multiple rotating square unit cells. Mech Syst Signal Process 2022;173:109065. https://doi.org/10.1016/j.ymssp.2022.109065.

[85] Wakshume DG, Płaczek MŁ. Optimizing Piezoelectric Energy Harvesting from Mechanical Vibration for Electrical Efficiency: A Comprehensive Review. Electronics (Basel) 2024;13:987. https://doi.org/10.3390/electronics13050987.

[86] Tabak A, Safaei B, Memarzadeh A, Arman S, Kizilors C. An Extensive Review of Piezoelectric Energy-Harvesting Structures Utilizing Auxetic Materials. Journal of Vibration Engineering & Technologies 2024;12:3155–92. https://doi.org/10.1007/s42417-023-01038-9.

[87] Wang T, Zhang Q, Han J, Tian R, Yan Y, Cao X, et al. Low-frequency energy scavenging by a stacked tri-stable piezoelectric energy harvester. Int J Mech Sci 2024;280:109546. https://doi.org/10.1016/j.ijmecsci.2024.109546.

[88] Forsberg G, Geréb G, Bjurström J, Rusu C, Lundgren P, Tiedke S. Piezoelectric Energy Harvesting For Rotating System. 19th International Conference on Micro and Nanotechnology for Power Generation and Energy Conversion Applications, PowerMEMS, Kraków: 2019.

[89] Wang Q, Zhang Y, Sun NX, McDaniel JG, Wang ML. High power density energy harvester with high permeability magnetic material embedded in a rotating wheel. In: Gyekenyesi AL, editor., 2012, p. 83470V. https://doi.org/10.1117/12.916980.

[90] Li M, Wen Y, Li P, Yang J, Dai X. A rotation energy harvester employing cantilever beam and magnetostrictive/piezoelectric laminate transducer. Sens Actuators A Phys 2011;166:102–10. https://doi.org/10.1016/j.sna.2010.12.026.

[91] Gu L, Livermore C. Passive self-tuning energy harvester for extracting energy from rotational motion. Appl Phys Lett 2010;97:081904. https://doi.org/10.1063/1.3481689.

[92] Zhang Y, Zheng R, Kaizuka T, Su D, Nakano K, Cartmell MP. Broadband vibration energy harvesting by application of stochastic resonance from rotational environments. Eur Phys J Spec Top 2015;224:2687–701. https://doi.org/10.1140/epjst/e2015-02583-7.

[93] Kim H, Zuo L, Tai W che. Self-tuning stochastic resonance energy harvester for smart tires. In: Erturk A, editor. Active and Passive Smart Structures and Integrated Systems XII, SPIE; 2018, p. 29. https://doi.org/10.1117/12.2296689.

[94] Kim H, Tai WC, Parker J, Zuo L. Self-tuning stochastic resonance energy harvesting for rotating systems under modulated noise and its application to smart tires. Mech Syst Signal Process 2019;122:769–85. https://doi.org/10.1016/j.ymssp.2018.12.040.

[95] V. Experimental researches in electricity. Philos Trans R Soc Lond 1832;122:125–62. https://doi.org/10.1098/rstl.1832.0006.

[96] Hampshire DP. A derivation of Maxwell's equations using the Heaviside notation. Philosophical Transactions of the Royal Society A: Mathematical, Physical and Engineering Sciences 2018;376:20170447. https://doi.org/10.1098/rsta.2017.0447.

[97] Derby N, Olbert S. Cylindrical magnets and ideal solenoids. Am J Phys 2010;78:229–35. https://doi.org/10.1119/1.3256157.

[98] Camacho JM, Sosa V. Alternative method to calculate the magnetic field of permanent magnets with azimuthal symmetry. Revista Mexicana de Física E 2013;59:8–17.

[99] Bird JO, Chivers PJ. Electromagnetism and magnetic circuits. Newnes Engineering and Physical Science Pocket Book, Elsevier; 1993, p. 77–87. https://doi.org/10.1016/B978-0-7506-1683-6.50013-8.

[100] Say M, Eastham J. Motors and Actuators. Electrical Engineer's Reference Book, Elsevier; 2003, p. 20-1-20–44. https://doi.org/10.1016/B978-075064637-6/50020-4.

[101] Li Z, Liu Y, Yin P, Peng Y, Luo J, Xie S, et al. Constituting abrupt magnetic flux density change for power density improvement in electromagnetic energy harvesting. Int J Mech Sci 2021;198:106363. https://doi.org/10.1016/j.ijmecsci.2021.106363.

[102] Amjadian M, Agrawal AnilK, Nassif HH. Development of An Analytical Method for Design of Electromagnetic Energy Harvesters with Planar Magnetic Arrays. Energies (Basel) 2022;15:3540. https://doi.org/10.3390/en15103540.

[103] Ordoñez V, Arcos R, Romeu J. A high-performance electromagnetic vibration energy harvester based on ring magnets with Halbach configuration. Energy Conversion and Management: X 2022;16:100280. https://doi.org/10.1016/j.ecmx.2022.100280.

[104] Carneiro P, Soares dos Santos MP, Rodrigues A, Ferreira JAF, Simões JAO, Marques AT, et al. Electromagnetic energy harvesting using magnetic levitation architectures: A review. Appl Energy 2020;260:114191. https://doi.org/10.1016/j.apenergy.2019.114191.

[105] Cai M, Liao W-H. Enhanced electromagnetic wrist-worn energy harvester using repulsive magnetic spring. Mech Syst Signal Process 2021;150:107251. https://doi.org/10.1016/j.ymssp.2020.107251.

[106] Xu J, Leng Y, Sun F, Su X, Chen X. Modeling and performance evaluation of a bi-stable electromagnetic energy harvester with tri-magnet levitation structure. Sens Actuators A Phys 2022;346:113828. https://doi.org/10.1016/j.sna.2022.113828.

[107] Foong FM, Thein CK, Yurchenko D. Structural optimisation through material selections for multi-cantilevered vibration electromagnetic energy harvesters. Mech Syst Signal Process 2022;162:108044. https://doi.org/10.1016/j.ymssp.2021.108044.

[108] Jiles DC, Atherton DL. Theory of ferromagnetic hysteresis. J Magn Magn Mater 1986;61:48–60. https://doi.org/10.1016/0304-8853(86)90066-1.

[109] Jiles DC, Atherton DL. Theory of ferromagnetic hysteresis (invited). J Appl Phys 1984;55. https://doi.org/10.1063/1.333582.

[110] Joule JP. XVII. *On the effects of magnetism upon the dimensions of iron and steel bars*. The London, Edinburgh, and Dublin Philosophical Magazine and Journal of Science 1847;30:76–87. https://doi.org/10.1080/14786444708645656.

[111] E. Villari. Change of magnetization by tension and by electric current. Annu Rev Phys Chem 1865;126:87–122.

[112] Ishikawa Y, Miura N, editors. Physics and Engineering Applications of Magnetism. vol. 92. Berlin, Heidelberg: Springer Berlin Heidelberg; 1991. https://doi.org/10.1007/978-3-642-84158-3.

[113] Kumar A, Arockiarajan A. Evolution of nonlinear magneto-elastic constitutive laws in ferromagnetic materials: A comprehensive review. J Magn Magn Mater 2022;546:168821. https://doi.org/10.1016/j.jmmm.2021.168821.

[114] V.A. Y. Magnetic Detection of Microstructural Change in Power Plant Steels. University of Cambridge, 2003.

[115] Hathaway KB, Clark AE. Magnetostrictive Materials. MRS Bull 1993;18:34–41. https://doi.org/10.1557/S0883769400037337.

[116] Coey JMD, Parkin SSP, editors. Handbook of Magnetism and Magnetic Materials. Cham: Springer International Publishing; 2021. https://doi.org/10.1007/978-3-030-63210-6.

[117] Berbyuk V. Vibration energy harvesting using Galfenol-based transducer. In: Sodano H, editor., 2013, p. 86881F. https://doi.org/10.1117/12.2009812.

[118] Dorfmann L, Ogden RW. The nonlinear theory of magnetoelasticity and the role of the Maxwell stress: a review. Proceedings of the Royal Society A: Mathematical, Physical and Engineering Sciences 2023;479. https://doi.org/10.1098/rspa.2023.0592.

[119] Atulasimha J, Flatau AB. Experimental Actuation and Sensing Behavior of Single-crystal Iron-Gallium Alloys. J Intell Mater Syst Struct 2008;19:1371–81. https://doi.org/10.1177/1045389X07086538.

[120] Shu YC, Lin MP, Wu KC. Micromagnetic modeling of magnetostrictive materials under intrinsic stress. Mechanics of Materials 2004;36:975–97. https://doi.org/10.1016/j.mechmat.2003.04.004.

[121] Fidler J, Chantrell RW, Schrefl T, Wongsam MA. Micromagnetics: Basic Principles. Encyclopedia of Materials: Science and Technology, Elsevier; 2001, p. 5642–50. https://doi.org/10.1016/B0-08-043152-6/00984-0.

[122] Dapino MJ, Smith RC, Flatau AB. Structural magnetic strain model for magnetostrictive transducers. IEEE Trans Magn 2000;36:545–56. https://doi.org/10.1109/20.846217.

[123] Berbyuk V, Sodhani J. Towards modelling and design of magnetostrictive electric generators. Comput Struct 2008;86:307–13. https://doi.org/10.1016/j.compstruc.2007.01.030.

[124] Callen E. Magnetostriction. J Appl Phys 1968;39:519–27. https://doi.org/10.1063/1.2163507.

[125] Scanlon WW. Solid state research of the Applied Physics Department for the year 1965. 1966.

[126] Liu SH, Behrendt DR, Legvold S, Good RH. Interpretation of Magnetic Properties of Dysprosium. Physical Review 1959;116:1464–8. https://doi.org/10.1103/PhysRev.116.1464.

[127] Thoburn WC, Legvold S, Spedding FH. Magnetic Properties of Terbium Metal. Physical Review 1958;112:56–8. https://doi.org/10.1103/PhysRev.112.56.

[128] Engdahl G, Bright CB. Device Application Examples. Handbook of Giant Magnetostrictive Materials, Elsevier; 2000, p. 287–322. https://doi.org/10.1016/B978-012238640-4/50021-8.

[129] Clark AE, Belson HS. Giant Room-Temperature Magnetostrictions in TbFe2 and DyFe2. Phys Rev B 1972;5:3642–4. https://doi.org/10.1103/PhysRevB.5.3642.

[130] Staley ME, Flatau AB. Characterization of energy harvesting potential of Terfenol-D and Galfenol. In: Flatau AB, editor., 2005, p. 630. https://doi.org/10.1117/12.604871.

[131] Scheidler JJ, Asnani VM, Deng Z, Dapino MJ. Dynamic characterization of Galfenol. In: Goulbourne NC, editor., 2015, p. 94320J. https://doi.org/10.1117/12.2085573.

[132] J. Scheidler J, Vivake M. Asnani, Marcelo J. Dapino. Dynamic Characterization of Galfenol (Fe81.6Ga18.4). Ohio: 2016.

[133] Dapino MJ, Deng Z, Calkins FT, Flatau AB. Magnetostrictive Devices. Wiley Encyclopedia of Electrical and Electronics Engineering, Wiley; 2016, p. 1–35. https://doi.org/10.1002/047134608X.W4549.pub2.

[134] Dapino MJ. Magnetostrictive Materials. Encyclopedia of Smart Materials, Wiley; 2002. https://doi.org/10.1002/0471216275.esm051.

[135] Deng Z, Dapino MJ. Modeling and design of Galfenol unimorph energy harvesters. Smart Mater Struct 2015;24:125019. https://doi.org/10.1088/0964-1726/24/12/125019.

[136] Clemente CS, Davino D, Loschiavo VP, Visone C. Non-linear modeling of a bi-layer magnetostrictive cantilever considering <math altimg="si2.svg" display="inline" id="d1e1203"> <mi mathvariant="normal">Δ</mi> </math> E effect. J Magn Magn Mater 2024;592:171755. https://doi.org/10.1016/j.jmmm.2024.171755.

[137] Meng A, Yan C, Li M, Pan W, Yang J, Wu S. Modeling and experiments on Galfenol energy harvester. Acta Mechanica Sinica 2020;36:635–43. https://doi.org/10.1007/s10409-020-00943-6.

[138] Clemente CS, Mahgoub A, Davino D, Visone C. Multiphysics circuit of a magnetostrictive energy harvesting device. J Intell Mater Syst Struct 2017;28:2317–30. https://doi.org/10.1177/1045389X16685444.

[139] Deng Z, Dapino MJ. Review of magnetostrictive vibration energy harvesters. Smart Mater Struct 2017;26:103001. https://doi.org/10.1088/1361-665X/aa8347.

[140] Daniel L, Ducharne B, Liu Y, Sebald G. Choosing the best magnetostrictive material for energy harvesting applications: A simple criterion based on Ericsson cycles. J Magn Magn Mater 2023;587:171281. https://doi.org/10.1016/j.jmmm.2023.171281.

[141] Liu Y, Lallart M, Ducharne B, Makihara K, Sebald G. Analysis of energy conversion capability among various magnetostrictive materials for energy harvesting. Smart Mater Struct 2023;32:125004. https://doi.org/10.1088/1361-665X/ad0392.

[142] Mizukawa Y, Ahmed U, Zucca M, Blažević D, Rasilo P. Small-signal modeling and optimal operating condition of magnetostrictive energy harvester. J Magn Magn Mater 2022;547:168819. https://doi.org/10.1016/j.jmmm.2021.168819.

[143] Ahmed U, Jeronen J, Zucca M, Palumbo S, Rasilo P. Finite element analysis of magnetostrictive energy harvesting concept device utilizing thermodynamic magneto-mechanical model. J Magn Magn Mater 2019;486:165275. https://doi.org/10.1016/j.jmmm.2019.165275.

[144] Ahmed U, Aydin U, Zucca M, Palumbo S, Kouhia R, Rasilo P. Modeling a Fe-Ga energy harvester fitted with magnetic closure using 3D magneto-mechanical finite element model. J Magn Magn Mater 2020;500:166390. https://doi.org/10.1016/j.jmmm.2020.166390.

[145] Ahmed U, Aydin U, Daniel L, Rasilo P. 3-D Magneto-Mechanical Finite Element Analysis of Galfenol-Based Energy Harvester Using an Equivalent Stress Model. IEEE Trans Magn 2021;57:1–5. https://doi.org/10.1109/TMAG.2020.3011875.

[146] Palumbo S, Rasilo P, Zucca M. Experimental investigation on a Fe-Ga close yoke vibrational harvester by matching magnetic and mechanical biases. J Magn Magn Mater 2019;469:354–63. https://doi.org/10.1016/j.jmmm.2018.08.085.

[147] Ahmed U, Blažević D, Mizukawa Y, Aydin U, Rasilo P. Validation of thermodynamic magneto-mechanical finite-element model on cantilever-beam type magnetostrictive energy harvester. J Magn Magn Mater 2022;564:170098. https://doi.org/10.1016/j.jmmm.2022.170098.

[148] Clemente CS, Davino D, Loschiavo VP. Analysis of a Magnetostrictive Harvester With a Fully Coupled Nonlinear FEM Modeling. IEEE Trans Magn 2021;57:1–4. https://doi.org/10.1109/TMAG.2021.3059927.

[149] Clemente CS, Davino D, Iannone I, Loschiavo VP. Experimental Characterization of an AC–DC Boost for Energy Harvesting Device Based on Magnetostrictive Materials. Electricity 2024;5:24–35. https://doi.org/10.3390/electricity5010002.

[150] Clemente CS, Iannone I, Loschiavo VP, Davino D. Design and Optimization of a Boost Interface for Magnetostrictive Energy Harvesting. Applied Sciences 2023;13:1606. https://doi.org/10.3390/app13031606.

[151] Iannone I, Clemente CS, Davino D, Loschiavo VP. AC-DC Boost Modelling for Magnetostrictive Energy Harvesting. 2021 IEEE International Conference on Environment and Electrical Engineering and 2021 IEEE Industrial and Commercial Power Systems Europe (EEEIC / I&CPS Europe), IEEE; 2021, p. 1–6. https://doi.org/10.1109/EEEIC/ICPSEurope51590.2021.9584550.

[152] Clemente CS, Loschiavo VP, Davino D. Enhancing Electric Vehicle Comfort with Magnetostrictive Energy Harvesting. 2023 IEEE Vehicle Power and Propulsion Conference (VPPC), IEEE; 2023, p. 1–6. https://doi.org/10.1109/VPPC60535.2023.10403255.

[153] Ueno T. Performance of improved magnetostrictive vibrational power generator, simple and high power output for practical applications. J Appl Phys 2015;117. https://doi.org/10.1063/1.4917464.

[154] Deng Z, Dapino MJ. Influence of electrical impedance and mechanical bistability on Galfenol-based unimorph harvesters. J Intell Mater Syst Struct 2017;28:421–31. https://doi.org/10.1177/1045389X16666176.

[155] Wei L, Liu H, Shu L, Zhao L, Liu Z, Chang Y. Study of a magnetostrictive energy harvester for harvesting transient shock vibration. Sens Actuators A Phys 2023;361:114577. https://doi.org/10.1016/j.sna.2023.114577.

[156] Cao S, Yang S, Zheng J, Zhang L, Wang B. An Equivalent Circuit Model and Energy Extraction Technique of a Magnetostrictive Energy Harvester. IEEE Transactions on Applied Superconductivity 2016;26:1–6. https://doi.org/10.1109/TASC.2016.2529295.

[157] Yoo J-H, Flatau AB. A bending-mode galfenol electric power harvester. J Intell Mater Syst Struct 2012;23:647–54. https://doi.org/10.1177/1045389X12436729.

[158] Ueno T. U-shape magnetostrictive vibration based power generator for universal use. In: Meyendorf NG, Matikas TE, Peters KJ, editors., 2016, p. 98060E. https://doi.org/10.1117/12.2218759.

[159] Bras Y Le, Greneche J-M. Magneto-Elastic Resonance: Principles, Modeling and Applications. Resonance, InTech; 2017. https://doi.org/10.5772/intechopen.70523.

[160] Clark AE, Restorff JB, Wun-Fogle M, Lograsso TA, Schlagel DL. Magnetostrictive properties of body-centered cubic Fe-Ga and Fe-Ga-Al alloys. IEEE Trans Magn 2000;36:3238–40. https://doi.org/10.1109/20.908752.

[161] Mahadevan A, Evans PG, Dapino MJ. Dependence of magnetic susceptibility on stress in textured polycrystalline Fe81.6Ga18.4 and Fe79.1Ga20.9 Galfenol alloys. Appl Phys Lett 2010;96. https://doi.org/10.1063/1.3280374.

[162] Elishakoff I. Who developed the so-called Timoshenko beam theory? Mathematics and Mechanics of Solids 2020;25:97–116. https://doi.org/10.1177/1081286519856931.

[163] Timoshenko S. History of Strength of Materials: With a Brief Account of the History of Theory of Elasticity and Theory of Structures. Dover Publications; 1983.

[164] Euler L, Daudet R, Delamonce FPJI, Dibner B. Methodus inveniendi lineas curvas maximi minimive proprietate gaudentes, sive, Solutio problematis isoperimetrici latissimo sensu accepti. Genevæ: Apud Marcum-Michaelem Bousquet & Socios; 1744. https://doi.org/10.5479/sil.318525.39088000877480.

[165] Erturk A, Inman DJ. A Distributed Parameter Electromechanical Model for Cantilevered Piezoelectric Energy Harvesters. J Vib Acoust 2008;130. https://doi.org/10.1115/1.2890402.

[166] Erturk A, Inman DJ. On Mechanical Modeling of Cantilevered Piezoelectric Vibration Energy Harvesters. J Intell Mater Syst Struct 2008;19:1311–25. https://doi.org/10.1177/1045389X07085639.

[167] Liao Y, Sodano H. Optimal power, power limit and damping of vibration based piezoelectric power harvesters. Smart Mater Struct 2018;27:075057. https://doi.org/10.1088/1361-665X/aabf4a.